Photodetectors based on graphene pn-junctions for mid-infrared to terahertz range

by

Sebastián Castilla

Thesis Advisor:
Prof. Dr. Frank H.L. Koppens

ICFO – Institut de Ciències Fotòniques
UPC – Universitat Politècnica de Catalunya

December 2021

Thesis committee:

Prof. Dr. Alessandro Tredicucci (University of Pisa, Italy)
Prof. Dr. Giacomo Scalari (ETH Zurich, Switzerland)
Prof. Dr. Valerio Pruneri (ICFO – Institut de Ciències Fotòniques, Spain)

To my family and Núria

Abstract

Long wavelength light contains the infrared and terahertz (THz) spectral range of the spectrum. This wavelength range spans approximately from 1 μm to 1 mm. Several applications can be explored in this spectral range such as thermal imaging, temperature monitoring, night vision, etc. Moreover, molecular vibrations resonate at these energies that are the fingerprints for compounds identification via molecular spectroscopy. Also, THz light has an important role in security since at these frequencies is possible to achieve a higher resolution for imaging compared to millimeter waves that are typically used in airports. Despite all these potential applications, long wavelength light technology still remains non-fully exploited. One of the reasons is due to the lack of competing instrumentation such as sources, modulators, detectors, sensors, etc. In particular, regarding the detectors, the commercially available technology present some issues such as the temperature of operation, speed, sensitivity, dynamic range, broadband frequency operation, CMOS compatibility, size and compactness, etc. The extensive research during the last years on graphene and other two-dimensional (2D) materials has opened new possibilities of novel light matter interactions that can unveil the next generation photodectectors and sensors, ascribed to the advantages respect to conventional semiconductors.

In this thesis, we focus on developing novel photodetection platforms in the mid, long-wave infrared and THz range based on graphene pn-junctions with integrated metallic nanostructures and hyperbolic 2D material. We have successfully integrated an antenna with a graphene pn-junction for highly sensitive and fast THz detection in this regime. This novel terahertz detector exploits efficiently the photothermoelectric (PTE) effect, based on a design that employs a dual-gated, dipolar antenna with a nanogap. We have demonstrated that this novel detector leads to an excellent performance, which fulfills a combination of figure-of-merits that is currently missing in the state-of-the-art detectors. We also overcame the main challenge of infrared photodetectors, which is to funnel the light into a small nanoscale active area and efficiently convert it into an electrical signal. We achieve this by efficient coupling of a plasmonic antenna to hyperbolic phonon-polaritons in hBN to highly concentrate mid-infrared light into a graphene pn-junction. We use a metallic bowtie antenna and H-shape resonant gates that besides concentrating the light into its nanogap, their plasmonic resonances spectrally overlap within the upper reststrahlen band (RB) of hBN (6-7 μm), thus launching efficiently these HPPs and guiding them with constructive interferences towards the photodetector active area. Additionally, by having two different antennas orientation, it allows us to have sensitive detection in two incident polarizations. Furthermore, we have shown mid and long-wave infrared photocurrent spectroscopy via electrical detection of graphene plasmons, hyperbolic phonon-polaritons and their hybridized modes. We combined in one single platform the efficiently excited polaritonic material that also acts as a detector itself. We identified peaks in the photocurrent spectra that evolves and blue shift by increasing the gate voltage, which are related to the polaritonic resonances. Finally, we investigated the electrical detection of molecular vibrations coupled to hyperbolic phonon polaritons in hBN. We detected this strong light-matter interaction via a graphene pn-junction placed at the vicinity of the molecules-hBN stack. The edges of the gap of the local gates launch efficiently the hBN HPPs that interact with the CBP molecular resonances that are spectrally located at the upper RB. We explored this interaction as a function of the thickness of the molecular

layers, near and far field contribution, etc.

Resumen

La luz de longitudes de onda largas consiste en el rango de infrarojo y terahercio (THz) del espectro. Este rango de longitud de ondas oscila entre los valores de 1 µm a 1 mm. En esta frecuencias, muchas aplicaciones pueden ser exploradas como por ejemplo las cámaras térmicas, monitorización de temperatura, visión nocturna, etc. Además, las vibraciones moleculares de muchos materiales oscilan en este rango de energías. Estas resonancias son utilizadas como huellas dactilares para la identificación de compuestos utilizando la espectroscopía molecular. También, la luz de terahercio juega un papel importante en el sector de seguridad. Esto se debe a que en estas frecuencias se puede conseguir una mayor resolución de imagen en comparación a las ondas milimétricas que son utilizadas mayoritariamente en los aeropuertos. A pesar de todo este potencial para diferentes sectores, la tecnología basada en luz de longitudes de onda largas sigue sin ser explotada del todo. Una de las razones es por la falta de equipos eficaces como por ejemplo las fuentes de luz, moduladores, detectores, sensores, etc. En particular, los detectores que se comercializan actualmente presentan limitaciones significativas como la temperatura de operación,velocidad, sensitividad, rango dinámico, ancho de banda de frecuencias, compatibilidad con CMOS, tamaño, etc. La investigación exhaustiva durante los últimos años en grafeno y otro materiales bidimensionales (2D) ha abierto nuevas posibilidades de nuevas interacciones entre materia y luz que podría contribuir para la nueva generación de fotodetectores y sensores debido a las ventajas de estos materiales respecto a los semiconductores convencionales.

En esta tesis nos enfocaremos en el desarrollo de plataformas novedosos en fotodección en el infrarrojo medio, largo y en el rango de terahercio. Estas plataformas están basadas en junciones pn de grafeno integradas con nanoestructuras metálicas y materiales 2D hiperbólicos. Hemos integrado satisfactoriamente una antena con una junción pn de grafeno para una detección sensitividad alta y rápida de terahercio. Este fotodetector novedoso de terahercio utiliza eficientemente el efecto fototermoeléctrico, el cual esta basado en un diseño que emplea una antena con un nanogap que a su vez actúa como doble puerta. También hemos demostrado que este novedoso detector realiza un gran desempeño, consiguiendo una combinación de aspectos a destacar que actualmente no se encuentran en los detectores en literatura. Además. superamos el mayor desafío de los detectores de infrarrojo, el cual consiste en dirigir este tipo de luz en la nanoescala hacia el área activa del detector y convertirla en una señal eléctrica. Conseguimos esto mediante una acoplación eficiente de una antena plasmónica con los fonones polaritones hiperbólicos (HPPs) para concentrar altamente la luz infrarroja media a una junción pn de grafeno. Utilizamos una antenna "bowtie" metálica y unas puertas resonantes con forma de H que además de concentrar la luz en su nanogap, sus resonancias plasmónicas solapan espectralmente con la banda reststrahlen (RB) superior del hBN (6-7 µm). Esto induce a que se puedan excitar eficientemente los HPPs y se guian hacia la área activa del fotodetector mediante intereferencias constructivas. Más aún, hemos demostrado en la espectroscopía de fotocorriente en el infrarrojo medio y largo mediante la deteción eléctrica de polaritones 2D. Hemos combinado en una sola plataforma el material plasmónico que a su vez actúa como el fotodetector. Hemos identificado picos en el espectro de fotocorriente que evoluciona a medida que aumentamos el potencial de puerta, lo cual es una insignia de una resonancia polaritónica. Finalmente, investigamos la deteción eléctrica de vibraciones

moleculares acopladas a HPPs en hBN. Hemos detectado esta fuerte interacción de luz y materia mediante una junción pn de grafeno que esta próxima a este pila de capas moleculares-hBN.

Contents

1 Introduction

1.1 Preface

Infrared light is typically divided in several spectral regions such as near infrared (∼0.75 to 3 µm), mid-infrared (∼3-8 µm), long-wave infrared (∼8-15 µm) and far infrared (∼15-30 µm). This separation of the range is loosely defined and depends mostly on the context or application.[1,2] The photodetectors at this wavelength range, specifically the mid and long-wave infrared, are widely used in several fields such as thermal imaging[1], temperature monitoring[2], night vision[3], motion detection,[1] surveillance,[1,2] etc. Moreover, molecular vibrations resonate at these energies that are the fingerprints for compounds identification via molecular spectroscopy.[4–6]

The terahertz (THz) range is spectrally located between 30 µm to 3 mm (∼0.1-10 THz). This particular region of the light spectrum is of great interest in many applications such as biomedical sensing and imaging,[7,8] wireless communication,[9] etc. In particular, THz light is important in security since it is capable of a higher resolution for imaging compared to millimeter waves that are typically used in airports.[10] In addition to this, THz light can penetrate dielectric materials that allow to detect explosives, drugs, etc.[11]

Despite all these potential applications, long wavelength light technology still remains non-fully exploited.[7] One of the reasons is due to the lack of competing instrumentation such as sources, modulators, detectors, sensors, etc. Particularly regarding the detectors, the commercially available technology present some issues such as working at room temperature,[10] speed,[12] sensitivity,[1] dynamic range,[10] broadband frequency operation,[2,10] compatibility with the complementary metal oxide semiconductor (CMOS) technology,[3] size and compactness,[1,13] etc.

The extensive research during the last years on graphene and other two-dimensional (2D) materials has opened new possibilities of novel light matter interactions that can lead to the next generation photodetectors and sensors.[2,14–16] These low dimensional materials present a clear advantage respect to conventional semiconductors since they are easier to integrate with silicon CMOS technology.[2,3]

In this thesis, we develop novel photodetection platforms in the mid, long-wave infrared and THz frequency range based on graphene pn-junctions with integrated metallic nanostructures and hyperbolic phonon polaritons in hBN. We demonstrate photodetection competing performances that overcome the figure of merits of the state-of-the-art graphene photodetectors and commercially available detectors. We also show electrical detection of 2D polaritonic nanoresonators that can be use for enhanced and spectrally selective photodetection, sensing, as a spectrometer, etc. Last but not least, we also electrically detect molecular vibrations coupled to hyperbolic phonon polaritons that paves the way for a highly sensitive compact sensor for molecular spectroscopy.

1.2 Thesis outline

The thesis is organized as follows:

- In Chapter 1, we give an overview of the capabilities and limitations of the detectors in the infrared and terahertz regime, the main optoelectronic properties of the 2D materials (graphene and hexagonal boron nitride) used as building blocks in the photodetectors. Also, we describe a brief summary of the main photodetection mechanisms in graphene detectors.

- We describe the state-of-the-art 2D heterostructures assembly in Chapter 2. We illustrate the fabrication techniques used to produce our devices and the main techniques we employed to measure the optoelectronic properties of the photodetectors, including the main figure of merits.

- In Chapter 3, we describe a highly sensitive and fast photodetector in THz based on an antenna-integrated graphene pn-junction. We illustrate that the photocurrent mechanism is driven by the photothermoelectric (PTE) effect in this regime, study the speed of these detectors and support the results by numerical simulations.

- In Chapter 4, we explore in depth the coupling between a plasmonic antenna with hyperbolic phonon polaritons in hBN. This strong light-matter interaction is investigated for mid-infrared photodetection using graphene.

- In Chapter 5, we demonstrate a suitable platform for long wavelengths photocurrent spectroscopy. This is achieved via electrical detection of 2D polaritonic nanoresonators.

- We investigate the electrical detection of molecular vibrations coupled to hyperbolic phonon polaritons via a graphene pn-junction photodetector in Chapter 6.

The Conclusion section includes a summary of the major accomplishments in this work together with an outlook of the future directions of each chapter and potential applications in the infrared regime.

1.3 Long wavelength detectors

Silicon (Si) photodiodes are widely used as detectors for visible light.[1,3] These detectors are able to measure incident light with an energy larger than the Si bandgap of 1.1 eV ($\lambda = 1.1$ µm) mediated by interband transitions. Thus, these detectors covers the visible and even a fraction of the near infrared range ($\lambda = 0.4$ - 1.1 µm). Nevertheless, beyond this small fraction of the light spectrum towards long wavelengths such as the mid-infrared or terahertz range other type of detectors are required to measure this light. These detectors are often classified depending on their mechanism of detection in the following two categories[2,10,12]}: thermal and photon detectors. The main figure of merits (FOM) that we compare between these detectors are the following: operation temperature, response

time (speed), dynamic range, which is the power range that the detector shows linear photoresponse. Regarding the sensitivity, several figure of merits are evaluated such as responsivity, noise-equivalent-power (NEP) which is the minimum detectable power that gives a signal-to-noise-ratio (SNR) of 1, detectivity that is inversionally proportional to NEP but considering the photoactive area. Moreover, the integration of these detectors to the CMOS (complementary metal oxide semiconductor) technology is also analyzed, as well as the detector compactness, size, weight and power consumption.

For the case of thermal detectors, the most frequently used are bolometers and pyroelectric detectors. The former ones are made of resistors with a small heat capacity and high temperature coefficient of resistance.[2,10] The mechanism is based on the change of its resistance owing to the heat produced by absorption of incident light. In the mid-IR the typical bolometric detectors are based on vanadium oxide.[1,2] On the other hand, the pyroelectric detectors are based on the spontaneous electrical polarization ascribed to the temperature change induced by the absorption of IR/THz light.[12,109] This effect produces a voltage across the top and bottom electrodes. Usually, commercially available pyroelectric detectors show good NEP of 0.2 nW/$\sqrt{\mathbf{Hz}}$ and detectivity of 9×10^8 Jones, but a slow response time in the order of seconds.[12] One general advantage of this type of room temperature detectors is the broadband frequency operation that ranges between 0.1-30 THz or from UV range to LWIR depending on the model.[12] In the case of the commercial bolometers we highlight the superconducting bolometer case that show a NEP sub-pW/$\sqrt{\mathbf{Hz}}$ with a rise of 50 ps.[10] The operation range is between 0.1-6 THz, however it has a low dynamic range (maximum detectable power of μW) and operates at cryogenic temperatures (4 K).[10]

Regarding the photon detectors, they are based on the interaction between electrons bound to lattice atoms/impurities or free electrons with light absorbed in a material. As a result, a change in the electronic energy distribution will cause an output electrical signal. The photon detectors also can be divided in two types depending on the charge carriers that carry the signal[2]: 1) minority and 2) majority charge carriers. The former type, usually consist on the direct band gap semiconductors such as HgCdTe (MCT, mercurium cadmium telluride). In the mid-infrared range, typically InGaAs and MCT are frequently used.[1,2] The former one covers the range up to 2.6 μm and the latter one up to 10.6 μm (13 μm at low temperature). These detectors can reach a fast rise time of few nanoseconds and also high sensitivity with detectivities in the range of 10^8 Jones.[2] Frequently, these photodetectors require an input bias and/or low temperature operation to reduce dark current. Furthermore, MCT and InGaAs require a complex growth process and also are challenging to integrate with CMOS technology due to the lattice mismatch with silicon substrate.[2,3] Additionally, the fabrication of these materials involve toxic elements such as mercury, cadmium, arsenic, etc.[1,2] On the other hand, the majority charge carriers photodetectors consist on Schottky barrier detectors or quantum wells with mediated intersubband transitions. In particular, Schottky diodes in the THz regime[17] are frequently used due to its room temperature operation that also combines the high speed (response time in the picoseconds range) and high sensitivity (NEP of 10-100 pW/$\sqrt{\mathbf{Hz}}$).[17] However, they have a low frequency cutoff (operation only below ∼1 THz) and a small dynamic range.[17] As it will be presented in this thesis, these major challenges mentioned above can be overcome by using graphene and other 2D materials.

1.4 Graphene overview

Since the first experiment back in 2004 performed by the Nobel Prize laureates Andre Geim and Konstantin Novoselov, graphene and low dimensional materials have raised the interest of a big part of the scientific community.[18] These materials opened new perspectives in many research fields that ranges from optoelectronic to biomedical devices.[2,14,15,19] Among these low dimensional materials, graphene is the one that has been more widely investigated.[18] This two-dimensional (2D) material is based on carbon atoms arranged into a hexagonal honeycomb lattice as shown in Fig. 1.1a. Graphene shows intriguing properties such as broadband absorption spectrum,[20,21] high carrier mobility ($>$ 10,000 cm^2/Vs)[18,22] at room temperature, small heat capacity,[23] etc.

These outstanding optoelectronic properties are given by its band structure, which has zero band gap meaning that its valence and conduction band touch at the so-called Dirac point or charge neutrality point (CNP).[18,20,21] Due to this, graphene is classified as a zero band-gap semiconductor or semimetal. This can be explained owing to the fact that the energy dispersion as a function of momentum is linear, which is accomplished for low energy values ($\sim$ 1 eV).[18,24,25] This linearity considers the charge carriers as massless particles, hence assuming they have zero effective mass and are described by the Dirac equation.[18,24,25] In addition, the Fermi energy in graphene is determined by equation 1.1 and can be tuned respect to the CNP by changing the charge carrier density (n_s):

$$E_F = \hbar v_F k_F = \hbar v_F \sqrt{\pi n_s} \tag{1.1}$$

where E_F is the Fermi energy, $\hbar$ is the reduced Planck's constant, v_F is the Fermi velocity of the charge carriers given by $v_F \approx c/300$ m/s and k_F is the Fermi wave vector.

1.5 Electronic properties of graphene

The graphene charge carrier density can be tuned electrostatically by applying a gate voltage[18]:

$$n_s = \sqrt{((V_G - V_{\mathbf{CNP}})C_{ox}/e)^2 + n_0^2} \tag{1.2}$$

where V_G stands for the applied gate voltage, $V_{\mathbf{CNP}}$ as the voltage at which the CNP is located due to intrinsic doping of graphene, $C_{ox} = \varepsilon_0 \varepsilon_{sub}/t_{sub}$ is the capacitance per unit area of the substrate with ε_{sub} and ε_0 as the DC dielectric permittivity of the substrate and free space respectively. The thickness of the substrate is given by t_{sub} and n_0 is the residual carrier density at CNP. The gate voltage typically is applied via a silicon backgate (or a metallic local gate) separated by a thin silicon dioxide layer (SiO_2) of $\sim$300 nm (or a thin layer of hBN). Thus forming a parallel plate capacitor between the Si backgate and graphene, where the charges accumulate on the gaphene as a function of the applied voltage (V_G).

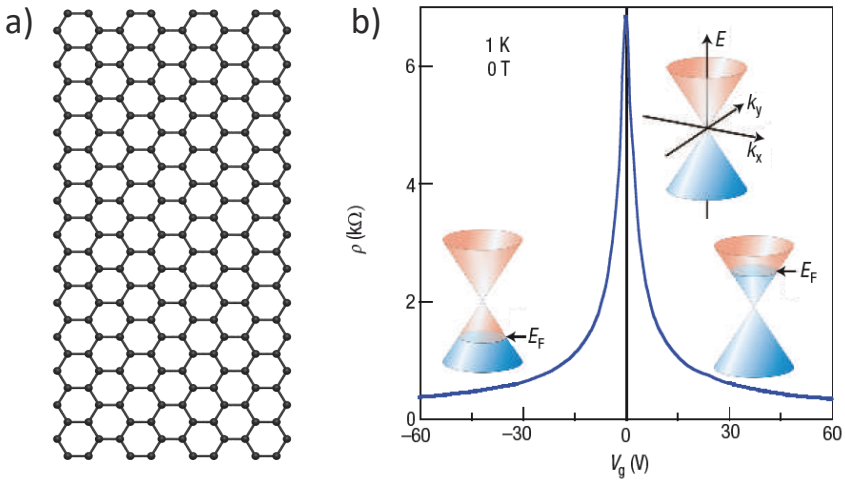

Fig. 1.1: a) Graphene, constituted by carbon atoms represented in black dots, forms a hexagonal honeycomb lattice. **b)** Graphene resistivity as a function of the gate voltage at 1 K. The inset shows the Fermi level as a function of the different gate voltages. By applying positive (negative) voltages, it induces electron (hole) doping. Figure adapted from ref. 18.

The charge carrier density is related to the electrical conductivity (σ) by the following equation:

$$\sigma = n_s e \mu \tag{1.3}$$

where μ is the charge carrier mobility of graphene and e the elementary charge. The conductivity of graphene is the inverse of the resistivity ($\sigma = 1/\rho$) that together with a geometrical factor dictate the channel resistance using the following equation[18]:

$$R = \frac{\rho L}{W} \tag{1.4}$$

where L and W correspond to the length and width of the graphene channel. Hence, the electrical properties of graphene can be tuned by changing the carrier density.[18,25] We observe in Fig. 1.1b the resistivity changes the majority charge carriers with the applied gate (V_G) from holes at negative voltages to electrons towards positive voltages. When n_s approaches to zero, the graphene shows maximum resistivity at the CNP. It is worth to mention that even thought n_s decreases significantly, the conductivity does not reach zero ascribed to n_0, which includes the charge impurities, dopants, etc. Moreover, although graphene charge carrier mobility achieves values in order of $\sim$ 10,000-100,000 cm^2/Vs at room temperature, it's limited by Coulomb scattering, acoustic phonons, etc.[18,26]

1.6 Optical properties of graphene

Owing to graphene's linear band structure and the fact that doesn't have a band gap, it provides a broad band optical absorption as shown in Fig. 1.2a.[20,24,25] We identify in

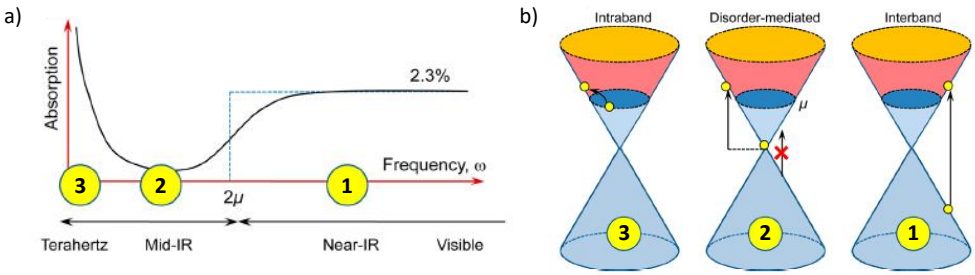

Fig. 1.2: a) Absorption spectrum of graphene from visible towards terahertz range. **b)** Optical transitions in graphene corresponding to the different ranges labelled in **a**. Figure adapted from 24.

Fig. 1.2a a frequency dependent optical spectrum spanning from visible towards terahertz (THz) light, which exploits different optical transitions in graphene (see Fig. 1.2b).[20,24] First, at the ultraviolet, visible and near-infrared (NIR) range (region labeled as 1 in Fig. 1.2a-b) we observe a flat absorption of 2.3%, known as the universal optical absorption constant of graphene ($\alpha = e^2/\hbar c = 1/137$) as this value is independent of the material parameters.[18,20,24] This absorption mechanism occurs due to interband transitions as shown in the band structure schematic in Fig. 1.2a-b, which takes place when the incident frequency is two times higher than the Fermi energy ($E_{\text{light}} > 2E_F$).[24] We point out that this absorption value is accomplished for suspended graphene, thus it might change considerably when graphene is placed on a substrate.[25]

Regarding the mid-infrared range (region 2 in Fig. 1.2), we notice a significant decrease in the absorption that corresponds to the so called Pauli blocking regime,[24,25] forbidding interband transitions of an electron from the valence to the conduction band. This occurs when $E_{\text{light}} < 2E_F$. Nevertheless, mid-IR light can be absorbed via disorder in graphene that provides the momentum required.[25] It is worth to mention that these disorder mediated transitions mainly occur in low mobility samples.[25] Finally, at THz frequencies (region 3), we observe that the absorption increases compared to the one at mid-IR range ascribed to intraband transitions.[20,24,25] In this regime when the photon energy is much lower compared to the Fermi energy ($E_{\text{light}} << E_F$), the absorption is mediated by free carriers and is described by the Drude response of graphene.[20,24,25,27] Analogous to the electronic properties of graphene, its optical response is also highly gate tunable, thus allowing different absorption regimes even at a fixed light frequency.[25]

1.6.1 Optical conductivity

The optical transitions discussed above are contained in the optical conductivity of graphene. Different models are used to describe this function, however in this thesis we mainly focus on the Drude response and local random phase approximation (RPA).[25]

Drude model

The Drude response for metallic materials is represented by free electrons. In the case of graphene, this model describes well its conductivity in particular for the intraband transitions. In this regime $E_{\text{light}} << E_F$ and $\omega\tau << 1$ and the conductivity is described as following:

$$\sigma(\omega, \tau, n_s) = \frac{2e^2 v_F \sqrt{\pi n_s}}{h} \frac{i}{\omega + i/\tau} = \frac{e^2 E_F}{\pi\hbar^2} \frac{i}{\omega + i/\tau} \tag{1.5}$$

where ω is the angular frequency of the incident light, τ the scattering time of the charge carriers and h ($\hbar$) is the (reduced) Planck constant. The permittivity and optical conductivity of graphene are related by the following equation[25]:

$$\varepsilon(\omega) = 1 + \frac{i\sigma(\omega)}{\varepsilon_0 \omega} \tag{1.6}$$

Local random phase approximation

In order to contain the whole graphene absorption spectrum in the optical conductivity, the interband and intraband contribution should be considered, as well as its dependence with doping level, carrier mobility and temperature. In the regime of local RPA for small momenta ($q \to 0$) and finite temperature (T),[25,28] the optical conductivity is described as following:

$$\sigma(\omega) = \sigma_{\text{intra}}(\omega) + \sigma_{\text{inter}}(\omega), \tag{1.7}$$

$$\sigma(\omega, T) = \frac{2e^2 T}{\pi\hbar} \frac{i}{\omega + i/\tau} \log[2\cosh(E_F/2k_B T)] + \frac{e^2}{4\hbar}\left[H(\omega/2) + \frac{4i\omega}{\pi}\int_0^\infty d\epsilon \frac{H(\epsilon) - H(\omega/2)}{\omega^2 - 4\epsilon^2}\right], \tag{1.8}$$

$$H(\epsilon) = \frac{\sinh(\hbar\epsilon/k_B T)}{\cosh(E_F/k_B T) + \cosh(\hbar\epsilon/k_B T)} \tag{1.9}$$

where k_B is the Boltzmann constant. The terms on equation 1.8 correspond to the intraband and interband absorption contributions respectively, with the intraband term described similarly with the Drude response as shown in equation 1.5. In Fig. 1.3 we observe the real and imaginary part of the local RPA optical conductivity.[25] We point out that we observe the 3 regimes explained for Fig. 1.2. The tunability of the optical conductivity is also observed in Fig. 1.3 by varying the Fermi level.

1.6.2 Plasmons

Surface plasmon polaritons (SPP) are collective excitation of free electrons coupled with incident light at the interface of a metal surrounded by dielectric media as shown in Fig. 1.4a.[25] They are characterized a significantly reduced wavelength and extreme volume confinement.[25,30] The dispersion relation of these SPP is described by:

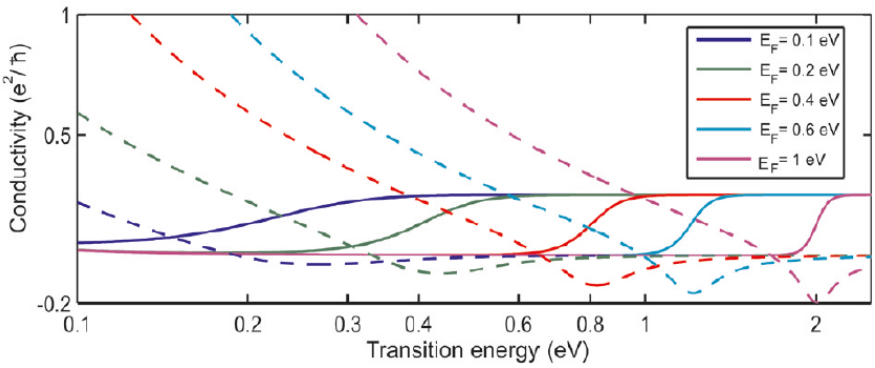

Fig. 1.3: Real (solid lines) and imaginary parts (dashed lines) of the optical conductivity at different Fermi energies. Figure taken from reference 29.

$$k_{sp} = \frac{\omega}{c}\sqrt{\frac{\varepsilon_d \varepsilon_m(\omega)}{\varepsilon_d + \varepsilon_m(\omega)}} \tag{1.10}$$

where ω stands for the free space angular frequency of the incident light, c for the speed of light in vacuum, ε_d and ε_m are the permittivity of the dielectric and metal respectively. The permittivities need to accomplish the condition $\varepsilon_d > 0$ and $\mathrm{Re}\,\varepsilon_m < 0$ in order to sustain the transverse magnetic (TM) SPP modes.[25]

The SPP wavelength is given by $\lambda_{sp} = 2\pi/\,\mathrm{Re}\,k_{sp}$, which is significantly lower than the incident wavelength.[25,30] In order to excite these plasmons, it's necessary to compensate the wave vector mismatch between the incident light and polaritonic wave vector via metallic grating structures, prism coupling, etc.[30] Additionally, at the mentioned interface, the penetration depth of the plasmon field (non-radiative) has a mode confinement in the axial direction of few nm at the mid-IR range, which is much lower than the diffraction limit.[30] Due to this, the electric field enhancement produced is several orders of magnitude higher compared to the incident light, thus increasing light-matter interactions.[30]

1.6.3 Graphene Plasmons

Graphene is able to carry plasmonic resonances driven by collective excitations of holes or electrons at sufficiently high Fermi energy. In comparison with its metallic counterpart, graphene presents lower loss plasmons owing to the considerably lower imaginary part of its optical conductivity. Moreover, it shows some other advantages such as higher confinement mode volume[31,32] and *in-situ* tunability of the plasmonic resonance via electrostatic doping. For all mentioned above, graphene plasmons are appealing for several applications in the field of sensing, photodetection[13], data communications, etc.[21,25]

The graphene plasmons properties can be described by considering its surface optical conductivity and following the boundary conditions at the interface[25]:

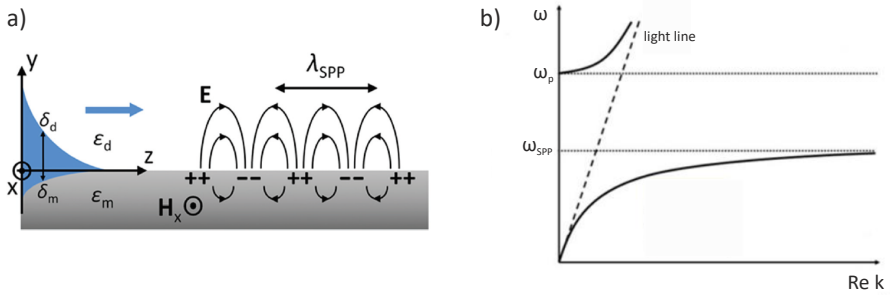

Fig. 1.4: a) Schematic of a surface plasmon polariton propagating at the interface between a metal (gray rectangle) and dielectric medium. The evanescent field of this polariton is represented at the left side of the panel. **b)** Dispersion relation of the SPP. The dispersion curves depict the lower and upper SPP modes. The upper curve (at $\omega > \omega_P$) corresponds to the radiation modes of unbounded SPPs. The lower curve depicts the bound SPPs. The dashed line is the linear dispersion of incident light. Figure adapted from reference 30.

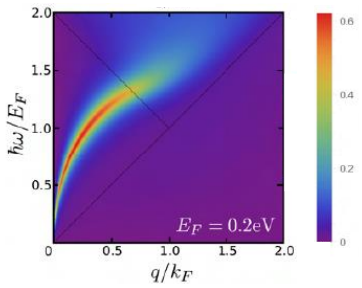

Fig. 1.5: Plasmons dispersion in graphene. The loss function is plotted in the color scale, which is the imaginary part of the reflection coefficient $\mathrm{Im}(r_p)$ calculated using RPA optical conductivity, as a function of the normalized energy and normalized momentum with Fermi energy of 0.2 eV. We see the loss function loses its intensity at high energy-mometum as it reaches the Landau damping regime (electron-hole continuum). Figure adapted from reference 25.

$$\frac{\varepsilon_1}{k_1(q,\omega)} + \frac{\varepsilon_2}{k_2(q,\omega)} + \frac{i\sigma(\omega)}{\varepsilon_0\omega} = 0 \tag{1.11}$$

where ε_1 and ε_2 are the permittivities of the substrate (labeled as region 1) and superstrate (labeled as region 2) respect to graphene and ε_0 as the vacuum permittivity. The out-of-plane wave vectors are represented by k_1 and k_2, $\sigma(\omega)$ as the optical conductivity of graphene and q as the in-plane wave vector.

By considering the dispersion relation for SPP in metal described in Eq. 1.10 and including the optical conductivity of graphene, which at long wavelengths (i.e. mid-IR or THz) is dominated by Drude response as described in Eq. 1.5 in the non-retarded regime ($q > \sqrt{\varepsilon_r}\omega/c$),[25] thus obtaining:

$$q \approx \frac{i2\omega\varepsilon_0\varepsilon_r}{\sigma(\omega)} \tag{1.12}$$

where ε_r is the average permittivity of the surrounding media (substrate and superstrate). By neglecting τ^{-1} in Eq. 1.5 and merging with Eq. 1.12,[25] we obtain:

$$\hbar\omega_{\mathbf{GSP}} \approx \sqrt{\frac{2\alpha}{\varepsilon_r} E_F \hbar c q} \tag{1.13}$$

The Eq. 1.13 shows the plasmon dispersion dependence $\omega_{\mathbf{GSP}} \propto \sqrt{q}$ and also the charge carrier density dependence $\omega_{\mathbf{GSP}} \propto n_s^{1/4}$, which exhibit its resonance tunability.

The graphene plasmon wavelength ($\lambda_{\mathbf{GSP}}$) in the electrostatic limit,[25] valid due to $\lambda_{\mathbf{GSP}}$ is considered much smaller than the radiation wavelength, is described by $\lambda_{\mathbf{GSP}} = 2\pi/\operatorname{Re}(q)$ and is related with the incident light wavelength (λ_0) by:

$$\frac{\lambda_{\mathbf{GSP}}}{\lambda_0} = \frac{2\alpha}{\varepsilon_r}\frac{E_F}{\hbar\omega} \tag{1.14}$$

1.7 Hexagonal boron nitride: electronic properties

Hexagonal boron nitride (hBN) is a layered material based on two-atom unit cell (B and N), which presents strong covalent bonds between these atoms and weak Van der Waals (VdW) forces between adjacent layers.[16,33] hBN has similarities in the crystallographic arrangement compared to graphene. Due to this fact, the lattice constant of hBN is just $\sim$ 1.7% larger than the graphene one.[16,33] Moreover, it presents an atomically flat surface that makes hBN a suitable candidate for using it as a substrate for graphene devices. One advantage besides other atomically flat materials is that it's an insulating material due to its large bandgap of $\sim$ 6 eV.[16,33] In addition to be an ideal material for encapsulation of graphene or other 2D materials, it also serves as a gate dielectric with a dielectric constant of $\varepsilon_r \sim$ 3-4 and a breakdown voltage of $\sim$ 0.7 V/nm.[34]

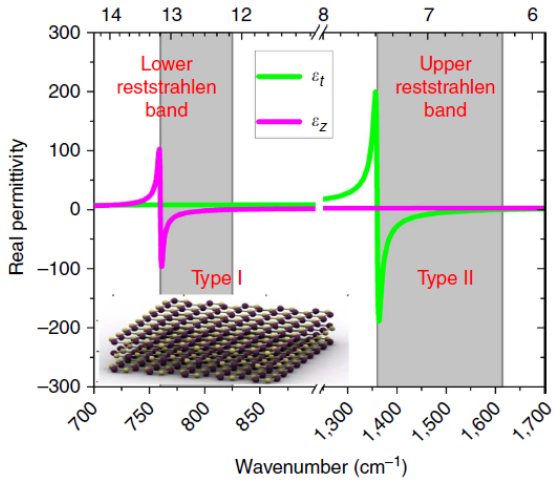

Fig. 1.6: Real part of the hBN permittivity components, where ε_t represents the in-plane component (defined previously as $\varepsilon_{x,y}$) and the out-of-plane component (ε_z). The upper and lower restrahlen bands are highlighted in gray. Figure adapted from reference 35.

1.8 Hexagonal boron nitride: optical properties

hBN presents interesting optical properties, in particular this low dimensional material is a natural hyperbolic material at mid-IR frequencies since it shows hyperbolic phonon polaritons (HPPs)[14–16,35,36]. This fact is due to its anisotropic permittivity (ε), where the in-plane ($\varepsilon_x = \varepsilon_y$) and out-of-plane ($\varepsilon_z$) permittivity present opposite sign at the restrahlen bands (RBs) as shown in Fig. 1.6. These bands are spectrally located between the transversal (TO) and longitudinal (LO) optical phonons.[16,33] These RBs are present at mid ($\sim$ 6.2-7.3 µm) and long-wave infrared ($\sim$ 12.1-13.2 µm) range, where the real part of the permittivity has a negative sign (either $\varepsilon_x = \varepsilon_y > 0$ and $\varepsilon_z < 0$ or vice versa).[16,33] Hence, the dispersion of the modes in k-space results in a hyperboloidal constant frequency surface instead of the typical spherical one for isotropic permittivity materials. This allows HPPs with a extremely small wavelength, thus with high momentum (k). Moreover, these polaritons propagate as a ray-like waves with a frequency dependent angle[33,35,37]:

$$\theta(\omega) = \arctan(i\sqrt{\varepsilon_{x,y}(\omega)}/\sqrt{\varepsilon_z(\omega)}) \tag{1.15}$$

1.9 Photodetection mechanisms

In this section we discuss the main mechanisms of photocurrent generation driven in graphene, which are represented in Fig. 1.7.[19]

1.9.1 Bolometric effect

This mechanism relies on the change in electrical conductance ($\Delta\sigma$) or in resistance (ΔR) ascribed to the change in temperature (ΔT) due to the absorption induced by the incident light (see Fig. 1.7a).[19,38–40] In particular, the modification of $\Delta\sigma$ is produced by the

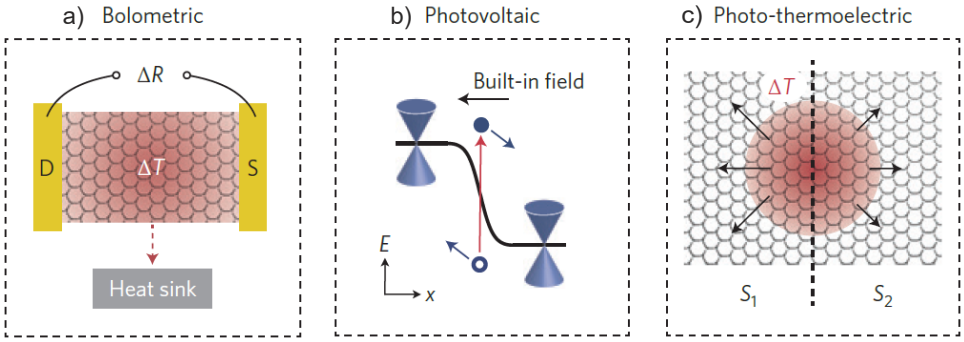

Fig. 1.7: Photocurrent mechanisms in graphene a) Bolometric effect representation in a graphene device. The red color represents high electronic temperature of the charge carriers and ΔR the measured differential resistance when exposing to illumination. **b)** Photovoltaic effect schematic that shows the separation of electron-hole pair via the built-in electric field. **c)** Photothermoelectric effect representation showing the temperature gradient (ΔT) across the channel and asymmetry in the Seebeck coefficient at the two regions (S_1 and S_2) due to the pn-junction configuration. Figure adapted from reference 19.

changes in carrier mobility ($\Delta\mu$). Hence this effect is based on the modifications of the transport properties of graphene rather than the transport of charge carriers. For operation under this mechanism is necessary a bias input in the channel as the change in $\Delta\sigma$ is measured. In contrast with other photodetection mechanisms it doesn't require a junction geometry, thus a uniform graphene channel is sufficient for light detection. The response time based on this mechanism can be very fast ($\sim$ ps timescale[38]) since it depends mainly on the cooling time of photoexcited carriers.[19]

1.9.2 Photovoltaic effect

The photovoltaic effect (PV) relies on a built-in electric field at a pn-junction in graphene for instance, where the electron-hole pairs are separated as shown in Fig. 1.7b.[19] Several methods can be employed for introducing this built-in field via electrostatic doping with local gates,[41] metal contact asymmetry with different work functions[42] or by chemical doping. In this mechanism there's no bias input required for operation. The PV effect can be measured in different configurations such as short-circuit mode, where the device is under illumination and the photocurrent collected is the short-circuit current (I_{sc}). Another configuration is the open-circuit, where a photovoltage is produced to counteract the internal (built-in) electric field, by accumulating photoexcited carriers with different polarities. The open-circuit voltage (V_{oc}) is the bias voltage needed to compensate the mentioned photovoltage.

1.9.3 Photothermoelectric effect

The photothermoelectric (PTE) effect occurs at graphene pn-junctions, where this doping asymmetry combined with a temperature gradient across the graphene channel drive a photovoltage.[42–44] The light absorbed by graphene causes an ultrafast heating of photoexcited carriers (so called hot carriers) and therefore a rise in electronic temperature (T_e). The photoexcited carriers quickly relax (< 100 fs)[23] into a local hot equilibrium Fermi-Dirac distribution by electron-electron scattering. Subsequent cooling mechanisms include electron-phonon scattering ($\sim$1 ps)[23,43–45] and heat diffusion away from the junction area (see Fig. 1.7c). As a result, a symmetric electronic temperature profile (T_e) is produced in the graphene junction giving rise to a thermoelectric photovoltage $V_{\mathbf{PTE}} \propto \nabla T_e(S_1 - S_2)$, where S represents the Seebeck coefficient of each region (1 and 2 corresponding to p and n-type doping) that is tunable by the graphene carrier density following the Mott equation:[46]

$$S = -\frac{\pi^2 k_B^2 T_e}{3e} \frac{1}{\sigma(E_F)} \frac{\partial \sigma(E)}{\partial E}\bigg|_{E=E_F} \tag{1.16}$$

where $\sigma(E)$ is the energy-dependent electrical conductivity. Additionally, due to the low electronic heat capacity, weak electron-phonon interaction and strong electron-electron interactions, the PTE effect is strong in graphene.[43,44] This photodetection mechanism will be covered in more details in Chapter 3.

2 Fabrication and measurement techniques

2.1 Fabrication of 2D heterostructures

In the last years, significant efforts for growing two-dimensional materials at large scale have been investigated. Several techniques have been employed for this task, such as chemical vapor deposition (CVD) and epitaxial growth of graphene.[47–49] Despite remarkable progress has been done, the carrier mobility achieved using these techniques remains considerably lower compared to the exfoliated graphene. As an alternative procedure for CVD growth, Banszerus et al.[22] has shown large scale single crystals of CVD graphene with high mobility such as ∼50,000 cm^2/Vs at room temperature. However, the device size is limited by the hBN flakes used for transferring the CVD graphene. By following this methodology, they avoid chemical etching of the copper substrate, which degrades considerably the quality of graphene.[22] In addition to this, growing CVD hBN is also a quite challenging task when several layers or thickness control are required.[50]

Despite of all the mentioned efforts, using natural van der Waals crystals still provide significantly higher quality of the materials' properties. These two dimensional crystals can be obtained by mechanical exfoliation onto a clean substrate. Generally, the standard substrate for graphene or other layered materials is silicon oxide (usually ∼300 nm thick) since it provides a pronounced optical contrast to these materials, which facilitates its identification.[51] However, several drawbacks occur by placing graphene or related materials on top of SiO_2. Mainly, the quality of graphene (intrinsically related to its carrier scattering time) is significantly harmed by charged impurities and surface roughness in silicon oxide.[52–54]

Therefore, to overcome this issue, a well established approach is to encapsulate graphene by a top and bottom slabs of hexagonal boron nitride[16,35,37,55]. This 2D dielectric material has a similar lattice constant compared to graphene, which makes it an ideal substrate since also provides an atomically flat surface without charged impurities.[34,54] This encapsulation method shows excellent results of graphene carrier mobility, reaching values of 100,000 cm^2/Vs.[56,57]

Hence, in this thesis we use mainly the exfoliated and encapsulated 2D layers in order to demonstrate the maximum performance achievable with high quality devices. We describe the state-of-the-art fabrication procedure of 2D heterostructures in the following sections.

2.1.1 Mechanical exfoliation and characterization

Graphene is obtained from highly ordered pyrolytic graphite (Graphenium flakes) and hBN crystals are provided by the collaboration with Prof. Kenji Watanabe and Prof. Takashi Taniguchi from the National Institute for Materials Science (Tsukuba, Japan). Initially, graphene and hBN flakes are mechanically cleaved by placing high-purity crystals of graphite or hBN between scotch tape, and exfoliating them into thinner layers. Afterwards, we press the tape containing these layered materials onto a freshly cleaned highly doped Si wafer with a thermally grown oxide layer of 285 nm. The thin graphite or hBN flakes are released onto the silica surface (Fig. 2.1a). Only a small fraction of them correspond to monolayer graphene or thin hBN (5-10 nm thick). At this thickness, interference effects with the substrate increase the optical contrast[51] of the flakes such

that even monolayers of graphene and other 2D crystals can be identified with an optical microscope as shown in Fig. 2.1b-d.

For further characterization, we use Raman spectroscopy that allows us to identify the 2D peak characteristic of monolayer graphene flakes as observed in the Raman spectrum shown in Figure 3.1 (e).

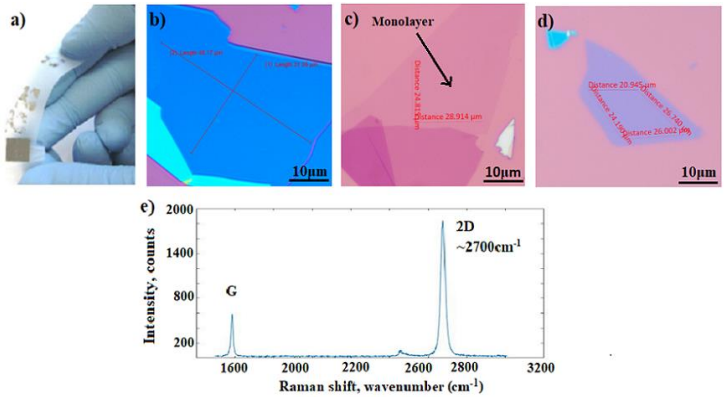

Fig. 2.1: Exfoliation procedure of graphene and hBN flakes. a) Illustration of the mechanical exfoliation of graphene or hBN using scotch tape onto a SiO2/Si wafer. Figure retrieved from 58. **b-d)** Optical images taken at 50x magnification of the exfoliated thick top-hBN **b**, monolayer graphene **c** and thin bottom-hBN **d**. All the figures have a 10 μm scale bar. **e)** Raman spectrum of the monolayer graphene flake from **c** showing its 2D peak characteristic at ≈2700 cm^{-1} and the G peak around 1500-1600 cm^{-1} from the sp^2 hybridization of graphene.

2.1.2 Characterization techniques

Raman spectroscopy is a particularly useful tool to probe the characteristics of graphene, such as its number of layers, defects and intrinsic doping[59]. This non-invasive technique relies on the inelastic (Raman) scattering of light, which is associated to the optical phonons of the investigated material. The Raman spectrum of graphene typically has three main peaks[59] located at 2700 cm^{-1} (2D peak), 1580 cm^{-1} (G peak) and 1350 cm^{-1} (D peak) as shown in Fig. 2.1e. The G peak corresponds to the optical phonon at the point ($q = 0$). Information about the doping of graphene can be obtained from the spectral position and width of the G peak. The D peak is activated by the presence of defects in the graphene lattice. Hence, a large ratio between the D and G peak implies a large defect density. The absence of D peak in the Raman spectrum indicates that the graphene flakes contains very few defects. Finally, the 2D peak, which involves double phonon scattering, is particularly useful for determining the number of layer because its shape and intensity varies as a function of the number of layers.

We use Atomic Force Microscopy (AFM) for characterizing the topography with nanometer resolution of the exfoliated flakes, substrates and metallic nanostructures. The AFM measures the height profiles from the changes of the resonance frequency of a tip due to

the interaction between the tip and the analyzed surface. By using this technique, we are able to detect the presence of residues associated to polymers during the exfoliation step, bubbles produced during the heterostructure stacking process, surface roughness of metallic gratings, etc. Moreover,we also measure the thickness of the 2D flakes as shown in Fig. 2.2.

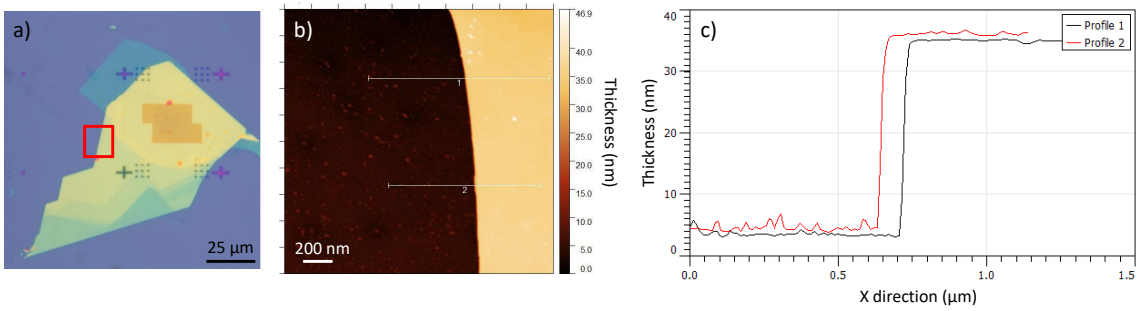

Fig. 2.2: AFM surface characterization of a hBN flake. a) Optical picture of a 2D heterostructure on top of metallic gratings. The red square region highlight the top hBN area that we scan using AFM. **b)** AFM scan across the top hBN flake area highlighted in **a**. **c)** Linecuts across the top hBN as indicated in white lines in **b**. We determine a flake thickness of 32 nm.

2.1.3 2D heterostructures assembly

After exfoliating and selecting the 2D flakes, the following fabrication step consists on assembling them. For this purpose, this technique relies on the strong van der Waals interaction between layered materials, which overcome the interactions between the flakes and the substrate. As a result, these flakes can be lifted up by others and form a so called 2D stack (top hBN/graphene/bottom hBN) as introduced by Wang et al.[34]

This precise method, also known as the "hot pick-up technique"[56,57], starts by making a transparent polymer stamp that serves as a substrate for the picked up flakes during the assembly process. The stamp consists of a thin (1 µm) layer of polycarbonate (PC) placed onto a transparent elastomer, polydimethylsiloxane (PDMS), which this latter one is placed onto a microscope slide (see 2.3). This stamp is mounted on a xyz micro-manipulator for proper alignment.

Initially, the selected top hBN flake exfoliated onto a SiO_2/Si substrate, is picked up by getting in contact with the PC stamp. This target Si wafer is placed on top of a rotational stage with xy adjustment. In addition, this stage can vary its temperature by a controlled heater. An overview of this transfer stage setup can be found in a similar setup described in ref. 60.

The flake and polymer stamp are aligned on top of each other with the help of a camera. The sample stage is then heated up to about 65-80 °C, a temperature close to the

melting point of PC. As a result, we can avoid that dirt or air get trapped forming blisters between the hBN-graphene interfaces. These blisters have a negative effect on the transport properties such as the device mobility.[57] The stage is then cooled back to room temperature and the polymer stamp is slowly lifted from the substrate. In most cases, the flake preferentially adheres to the stamp and results in a successful picked-up. If the process fails, it is repeated until it succeeds.

Once the first flake is on the polymer stamp, the following flakes can be picked up by following the same procedure. When the 2D heterostructure is completely assembled, one can release it onto a target substrate by depositing the stamp on it and heating the stage to 180 °C. At this temperature, the PC softens and adheres to the substrate, which allows the PC to be de-attached from the PDMS and microscope slide. The PC is finally dissolved in chloroform and isopropanol, thus allowing the heterostructure to remain on the substrate as shown in Fig. 2.3.

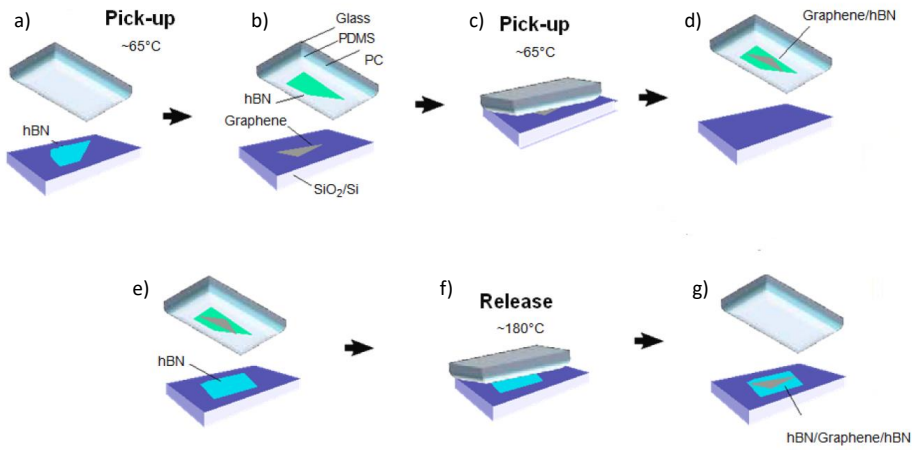

Fig. 2.3: Assembly procedure of a 2D (hBN/graphene/hBN) heterostructure. a) The top hBN on silicon wafer is picked up by the PC/PDMS stamp. **b)** The picked up top hBN is then aligned with a graphene flake on a SiO_2/Si substrate. The alignment is performed using a 20-50x microscope objective with an incorporated camera. **c)** These two flakes are brought into contact. During this process the stage is heated up to 65-80 ºC and cooled back to room temperature. The stamp is then slowly lifted in order to pick up the graphene flake from the substrate. **d)** The graphene flake is now picked up and located below the top hBN flake. **e)** Then, the graphene/hBN stack on the stamp is aligned with the bottomn hBN flake. **f)** The graphene/hBN stack is released on the bottom hBN flake by pressing the stamp and heating the polymer to 180 ºC. **g)** At this high temperature, the PC is de-attached from the PDMS/glass slide stamp and remains on top of the 2D stack.

2.2 Fabrication of electrical contacts and metallic nanostructures

The encapsulation of graphene using dielectric hBN slabs provide significant advantages as explained above. However, it prevents direct access to graphene be electrically contacted. In 2013 Wang et al.[34] showed that in this configuration, graphene can be electrically connected via one-dimensional contact between a metal-graphene interface. This approach consists in the following: an electron beam lithography (EBL) pattern containing the eletrical contacts overlapping the graphene flake (see Fig. 2.4a). In particular, we use a 30 keV beam voltage from Raith system that can reach very small features in the order of tens of nanometers. After the photoresist development, the edge of the encapsulated graphene is exposed by etching the resist-free area of the heterostructure. This process is performed by using Reactive Ion Etching (RIE) system from Oxford Instruments (Plasmalab System 100). We use SF_6 gas to etch the top hBN since the etching process stops at graphene surface[61]. Then, for etching graphene we use O_2 gas. In this way, we perform a selective etching and protect the bottom hBN that typically serves as the dielectric between the metal gate and graphene.

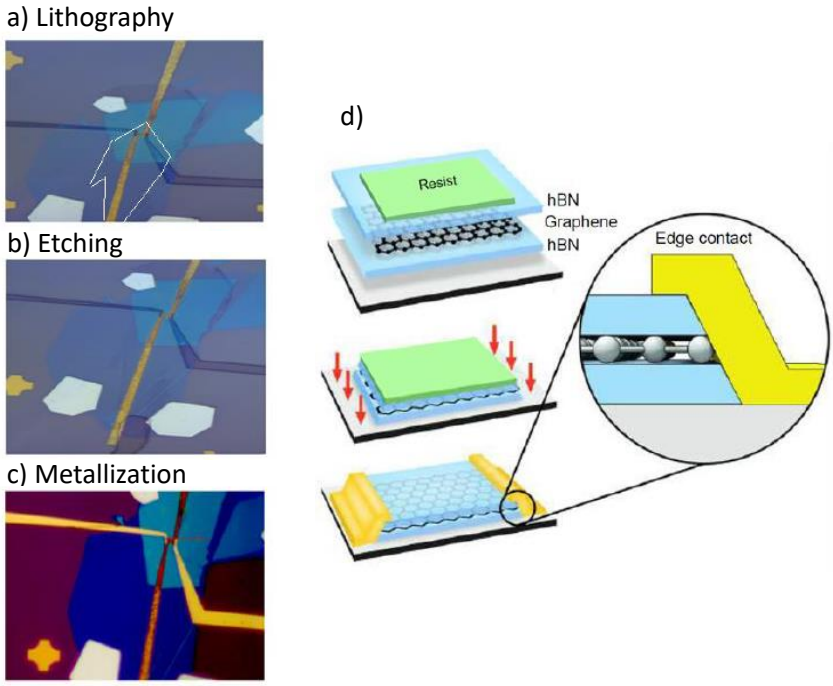

Fig. 2.4: One-dimensional edge contact. **a)** The electrical contacts are defined by EBL patterning and subsequent development of the exposed resist. The graphene flake is highlighted in white contour line. **b)** Etching step of the exposed resist-free area of the heterostructure. **c)** Metallic deposition of electrodes by evaporating a thin gold film on the sample. **d)** Illustration of the process described in **a-c** as shown in ref. 34.

After the top hBN layer is fully etched, a thin metal layer is deposited over the en-

tire substrate with an evaporator (Leybold Univex 350) operating at low pressure (∼1e-7 mbar). Later, we place the substrate in an acetone solution in order to dissolve the unpatterned resist and thus the metal on top is lifted-off. Thereby, the only metal remaining in the substrate is located at the lithography patterned regions as shown in Fig. 2.4c. We typically evaporate a metal combination of 5 nm of chromium and 50 nm of gold, which are deposited using electron beam evaporation and thermal evaporation respectively. Additionally, by following this same procedure but without the etching step, we pattern and evaporate also metallic nanostructures such as split gates, antennas or gratings as shown in Fig. 2.5. In some cases we vary the thickness of the metallic layer down to 10 nm.

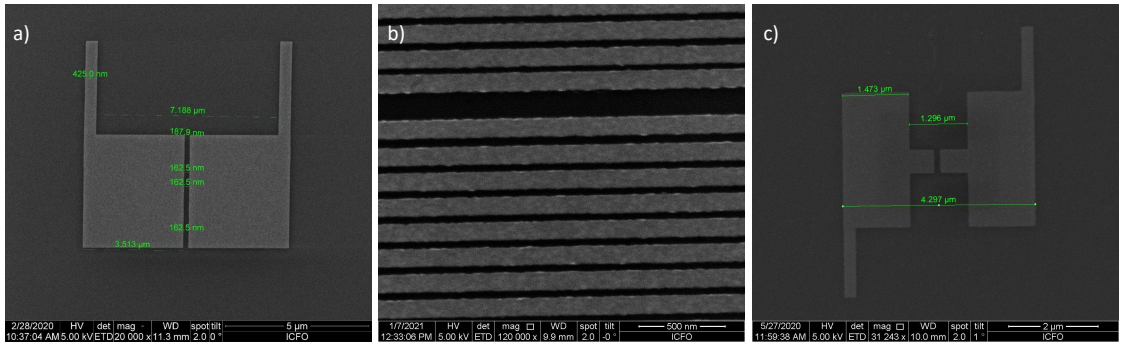

Fig. 2.5: Scanning electron microscopy (SEM) pictures of metallic nanostructures. **a)** Rectangular split gate. Length scale lines are indicated in green. **b)** Grating gates with nanometer scale period. **c)** Local gates that serves also as a mid-infrared antenna. Length scale lines are indicated in green.

2.3 Measurements techniques

2.3.1 Electrical measurements

To characterize the electrical properties of the fabricated graphene transistors, we mount them on a chip carrier (from Chelsea Technology) that contains 28 pins. This chip carrier containing the sample is mounted into a chip holder connected to a break-out box, which has all the connections to a common ground and serves also as a switch for voltage input via BNC cables. We use QTLab software for data acquisition of the measured devices and also for controlling the different equipments. Mainly, we control the voltages applied to the device gates and contacts with a digital-to-analogue converter (DAC, National Instrument) and/or Keithley sourcemeter (2450 model). To measure the voltage or current from the device output, we also use the DAC or a lock-in amplifier (Standford Research SR830). These transport measurements can be typically measured with two or four terminal configuration. The electrical characterization results provide the sample resistance as a function of gate voltages (see Fig. 2.6), which is intrinsically related to the charge carrier density as described in chapter 1. By acquiring the device resistance, we can estimate several relevant physical parameters of graphene, such as its carrier mobility, residual doping and contact resistance as we show in the following sections.

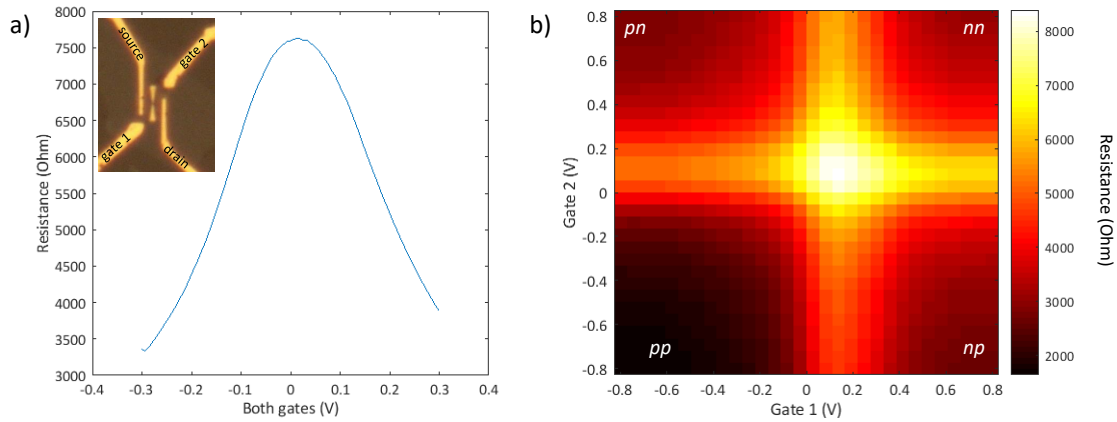

Fig. 2.6: Electrical characterization of graphene split gated device. **a)** Two-terminal resistance of the investigated graphene device with both gates at the same potential. The inset displays the photodetector outlook with the respective electrodes and gates. **b)** Resistance map as a function of the two gates. They are controlled independently and several junction configurations are formed as indicated in the figure.

2.3.2 Scanning photocurrent microscopy

The technique scanning photocurrent microscopy (SPM) consists on scanning a sample mounted on a xyz-motorized stages while keeping fixed the laser position and acquiring its photoresponse (see Fig. 2.7a). Also one can explore the approach of maintaining the sample at a fixed position and scanning the laser position, however in this thesis we work with the former described configuration. The obtained spatial photocurrent maps provide information on the optoelectronic properties of the analyzed material. For instance, by determining the maximum photoresponse position, one can distinguish the dominant photocurrent mechanism of the investigated photodetector. SPM also provides information to identify the photoresponse acquired from different contributions such as the graphene p-n junction and graphene-metal junction in PTE based photodetectors. [62]

The measurement setup consists in the following: typically we use a quantum cascade laser (QCL) as a source, which is wavelength tunable and has broadband operation in mid-IR, LWIR or THz range. In the the following chapters, we will indicate the exact light source employed and its characteristics for each project. The laser is also modulated by a mechanical chopper at a frequency of $\sim$ 300 Hz. The light is focused onto the photodetector by a reflective objective with a numerical aperture (NA) of 0.5 (LMM-40X-UVV from Thorlabs), thus achieving a laser spot size (full width at half maximum, fwhm) close to the incident wavelength (λ). The photodetector sample is mounted on a motorized stage (Newport SMC100 controller with motors TRA12PPD (X,Y) and TRA25PPD (Z)) that allows us to control the xyz-position of the device with an accuracy at the nanometer scale in the three directions. The photocurrent generated by the modulated laser beam is measured with a lock-in amplifier (Standford Research SR830) synchronized with the

mechanical chopper frequency, this allows to isolate the generated signal from the noise induced by ambient light or other sources such as dark current. We point out that all the measurements shown in this thesis were performed at room temperature and at ambient conditions. We use QTLab software for data acquisition of the measured photodetectors and also for controlling the different equipments as explained above. Moreover, via this software we tune the QCL wavelength, the polarizers position, lock-in characteristics, motorized stage positions, powermeter acquisition, etc.

2.3.3 Photocurrent spectroscopy at mid-IR, LWIR and THz range

Photocurrent spectroscopy is a useful technique to study the photoresponse as a function of incident photons' energy (wavelength). This can provide information of the energetic transitions that play a role in photocurrent generation in the photoactive material. Thus, by measuring its photocurrent spectrum we can obtain information about its absorption spectrum that are intrinsically related. We can also probe interactions between the active material with polar substrate phonons[63], polaritonic enhancement[64], etc. We point out that in some cases the photocurrent spectroscopy is more sensitive compared to the absorption spectroscopy[65] since the former one consists in probing a spatially localized region and hence can measured small samples, which is a limitation for techniques such as FTIR.

To carry out these measurements, we use a wavelength tunable QCL that ranges from 6.6 to 13.6 µm or 1515-735 cm^{-1} (in this case we use MIRcat from Daylight Solutions) with a spectral resolution of 0.1 cm^{-1}. We set the position of the motorized stages to the ones showing the maximum photoresponse (see Fig. 2.7a). At this position we collect the photocurrent as explained for the SPM technique. We then sweep the laser wavelength and construct the photocurrent spectrum (see Fig. 2.7b). We also consider any shift of the beam position across the whole wavelength range and relocate at that position, which shows the maximum photocurrent value.

2.3.4 Responsivity and NEP calculation

For determining the responsivity $\mathbb{R} = I_{\mathbf{PTE}}/P_{\mathbf{diff}}$, we extract the measured PTE photocurrent $I_{\mathbf{PTE}}$ from the output signal of the lock-in amplifier $V_{\mathbf{LIA}}$ using $I_{\mathbf{PTE}} = \frac{2\pi\sqrt{2}}{4G} V_{\mathbf{LIA}}$ [66–68], where G is the gain factor in V/A (given by the lock-in amplifier). The power in a diffraction-limited beam is given by $P_{\mathbf{diff}} = P_{\mathbf{in}} \cdot A_{\mathbf{diff}}/A_{\mathbf{focus}}$, where the ratio $A_{\mathbf{diff}}/A_{\mathbf{focus}} = \frac{w_{0,\mathbf{diff}}^2}{w_{0,\mathbf{x}} w_{0,\mathbf{y}}}$. In order to obtain $w_{0,\mathbf{x}}$ and $w_{0,\mathbf{y}}$ we use our observation that the photoresponse is linear in laser power and measured the photocurrent while scanning the device in the $x-$ and $y-$direction. The photocurrent is then described by Gaussian distributions $\propto e^{-2x^2/w_{0,\mathbf{x}}^2}$ and $\propto e^{-2y^2/w_{0,\mathbf{y}}^2}$, where $w_{0,\mathbf{x}}$ and $w_{0,\mathbf{y}}$ are the respectively obtained spot sizes (related to the standard deviation via $\sigma = w_0/2$ and to the FWHM via FWHM $= \sqrt{2\ln(2)} w_0$), see Fig. 2.8. For instance while performing THz measurements, we obtained $w_{0,\mathbf{x}} = 263.3\ \mu$m and $w_{0,\mathbf{y}} = 331.2\ \mu$m. For the diffraction-limited spot, we took $w_{0,\mathbf{diff}} = \frac{\lambda}{\pi}$, with λ the THz laser wavelength. The diffraction-limited area is thus taken as $A_{\mathbf{diff}} = \pi w_{0,\mathbf{diff}}^2 = \lambda^2/\pi$.

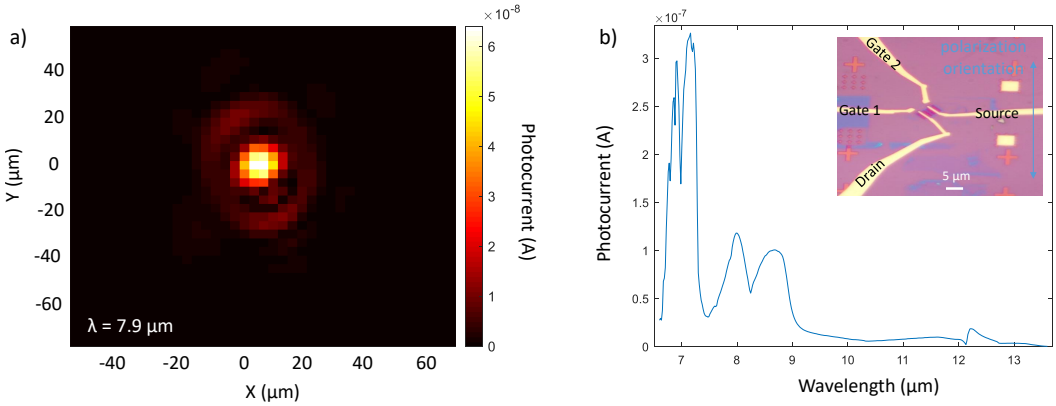

Fig. 2.7: Photocurrent measurements. **a)** Photocurrent map as a function of the scan position in x and y-directions of the motorized stage. The laser incident wavelength is 7.9 μm. **b)** Photocurrent as a function of the incident wavelength. In the inset shows the split gated hBN encapsulated graphene device outlook with the respective electrodes and the incident light polarization.

Additionally, the noise-equivalent power (NEP) that characterizes the sensitivity of the photodetector is defined as NEP $= I_{\mathbf{noise}}/$Responsivity and considering that our unbiased photodetector has a very low noise current that is limited by Johnson noise, we use a noise spectral density $I_{\mathbf{noise}} = \sqrt{\frac{4k_{\mathbf{B}}T}{R_{\mathbf{D}}}}$, where $k_{\mathbf{B}}$ corresponds to the Boltzmann constant, T is the operation temperature (300 K) and $R_{\mathbf{D}}$ the device resistance.

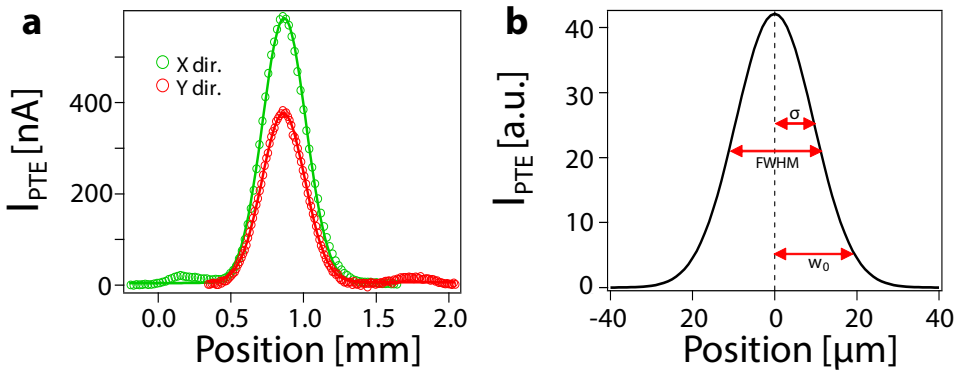

Fig. 2.8: Characterization of spot size for THz measurements on Device A described in Chapter 3. a) Photocurrent as a function of the scan position in x-direction (green) and y-direction (red) of the motorized stage onto which the device is mounted. The laser was tuned to 2.52 THz. The open dots represent the experimental data and the lines the fits according to Gaussian distributions. We obtain a FWHM of 351 (348) μm for x- ($y-$) scan direction. **b)** Calculated Gaussian distribution representing a diffraction-limit focus at 2.52 THz. The arrows indicate the standard deviation σ, FWHM and spot size w_0, corresponding to 60, 50 and 13.5% of the maximum, respectively.

3 Antenna-integrated graphene pn-junction for fast and sensitive terahertz detection

3.1 Introduction

Photodetectors operating at THz frequencies play an important role in many applications in the fields of medicine, security, quality testing, chemical spectroscopy and more[7,8,11,69–72]. One of the main benefits of THz radiation is its non-invasive nature and its capability to penetrate most dielectric materials, which are typically opaque at non-THz frequencies. For example, in the case of medical imaging and security applications, THz radiation offers clear advantages since it is non-ionizing due to its low photon energy (in the meV range) in contrast with conventional X-ray radiation with much higher photon energy (in the keV range), leading to strongly reduced health risks. Furthermore, THz detectors are expected to play an enabling role for data communication at THz bit rates[9,73,74]. For many of these applications, the ideal THz detector would meet the following five requirements: it should be highly sensitive (*i.e.* have a low noise-equivalent power, NEP), operate at room temperature, give a fast photoresponse, have a high dynamic range (the range between the lowest and highest measurable incident light power), and work over a broad range of THz frequencies, in particular above 1 THz.

Commercially available room-temperature THz detectors, for example pyroelectric detectors and Golay cells, are reasonably sensitive with an NEP on the order of $\sim$1 nW/$\sqrt{\textbf{Hz}}$. However, their response time is very long: 100 and 30 ms, respectively[12,75]. Superconducting bolometric THz detectors, on the other hand, can be highly sensitive with an NEP of $\sim$0.5 pW/$\sqrt{\textbf{Hz}}$, while simultaneously showing fast operation with a response time of $\sim$50 ps. However, these detectors require cryogenic temperatures ($\sim$4 K) and suffer from a narrow dynamic range (linear response up to a power value of $\sim$0.1 μW)[10]. Schottky diodes, although combining high speed (response time in the picoseconds regime) and high sensitivity (NEP of 10 - 100 pW/$\sqrt{\textbf{Hz}}$), have a low frequency cut-off (operation only below $\sim$1 THz) and a small dynamic range[17,76]. Thus, currently there are no commercially available THz detectors that simultaneously meet all five requirements.

Owing to its exceptional optoelectronic properties and broadband absorption spectrum (from the visible down to the GHz-THz range) graphene is a highly interesting photoactive material for detecting light[19,20,24,66,77,78]. During the past couple of years, there were several experimental demonstrations of graphene-based photodetection in the GHz-THz range. These detectors were based on various operating mechanisms. First of all, there were reports describing plasma wave-assisted THz detection, typically in the overdamped regime[66,67,79–81]. However, this scheme has resulted in high sensitivities with an NEP below nW/$\sqrt{\textbf{Hz}}$. Secondly, ballistic graphene rectifiers were demonstrated with excellent sensitivity, but only operating below 1 THz[82]. Moreover, a graphene-antenna coupled bolometer for detecting GHz radiation was shown with promising values of sensitivity at low temperatures[39].

Alternatively, one can exploit the photo-thermoelectric (PTE) effect, where absorbed THz light heats up the graphene electrons[27], subsequently creating an electron-heat driven photoresponse if an asymmetry is present in the device[43]. Such an asymmetry could be created, for example, by using two different contact metals or by using two adjacent graphene regions of different doping, *e.g.* forming a junction. Photodetection based on the PTE effect in graphene was first shown for visible light, where *interband* absorption of

light occurs[44,83]. More recently, also photoresponses in the THz frequency regime, where absorption occurs through *intraband* processes, were attributed to the PTE effect[42,84]. Moreover, several of the previously mentioned studies exploiting alternative mechanisms also attributed a potentially significant fraction of the observed THz photoresponse to the photo-thermoelectric effect[66,67,78–82]. Clearly, some controversy exist on which photoresponse mechanism dominates for graphene excited by THz light, which has hampered the development of more optimized detectors. Furthermore, the main challenge for exploiting the PTE effect for THz detection is the large mismatch between the large area of the incoming radiation and the small photo-active area of graphene, where the PTE effect occurs.

Here, we solve this issue by introducing an antenna-integrated THz photodetector, based on high-mobility, gate-tunable, hexagonal BN (hBN)-encapsulated graphene, where the incoming THz radiation is concentrated such that it overlaps with the small photoactive area of the graphene. Using the gate-tunability of the detector, we find that the PTE effect is the dominant photoresponse mechanism. We support this with a quantitative comparison of the device response with numerical simulations and an analytical model of the PTE photoresponse. We furthermore show that, owing to its novel device design, our PTE THz photodetector meets all five requirements of an ideal detector. In addition, it has the advantage of being based on low-cost materials with scalable integration capabilities with the well established CMOS electronics for low-cost imaging systems[3]. Finally, it is very low in power consumption, as it is a passive device.

In the following, we will first explain how our antenna-integrated *pn*-junction THz detector works, followed by the experimental characterization of the detector. Subsequently, we provide an analytical model of the PTE detector and numerical simulations of the absorption enhancement of graphene induced by the antenna, and compare these results with the experiments. Finally, we will compare the THz photodection performance to the state of the art.

3.2 Device fabrication

In a nutshell, our THz photodetector consists on two metallic branches that form a dipole antenna. These branches simultaneously work as local gates that can apply independently voltages. We place on top of this antenna a graphene monolayer encapsulated between top and bottom thin layers of hBN. The graphene is patterned and contacted with metallic electrodes. The fabrication of these devices are described as following: first we patterned the antenna/gate structure on transparent SiO_2 (Infrasil) substrate using electron beam lithography followed by evaporation of titanium (2 nm) / gold (30 nm). The antenna gap was 200 nm (100 nm) for device A (B). We then released an hBN/graphene/hBN stack onto the antenna/gate structure. The stack elements (top and bottom hBN and graphene) were mechanically cleaved and exfoliated onto freshly cleaned Si/SiO_2 substrates. The full stack was prepared by the Van der Waals assembly technique[34,56] and released onto the antenna/gate structure. This was followed by patterning source and drain electrodes, using electron beam lithography with a PMMA 950 K resist film and exposing it to a plasma of CHF_3/O_2 gases for partially etching the stack. Consequently, we evaporate side contacts

of chromium (5 nm) / gold (60 nm) and lift off in acetone as described in Ref.[34]. Finally, the encapsulated graphene was etched into the "H" shape using a plasma of CHF_3/O_2 gases. From gate-dependent measurements (varying V_L and V_R simultaneously) on Device A, we extract a mobility >20,000 cm^2/Vs and a contact resistance of 126 Ω (3.8 $k\Omega \cdot \mu m$) (see Fig. 3.2).

We have fabricated two "H-shaped", high-mobility, hBN-encapsulated graphene devices with a dipolar antenna/gating structure, (see Fig. 3.1). We mainly show the results obtained from THz photodetector Device A and will mention some results from THz photodetector Device B. Both Device A and Device B have a width of the central part of the graphene channel (at the junction) of $w = 2$ μm, whereas the gap sizes of the dipolar antennas are 200 and 100 nm, respectively. The vertical distance between antenna and graphene is given by the thickness of the bottom hBN layer, typically ~15 nm, and thus small enough to warrant sufficient overlap between the electric field profile around the antenna gap, and the graphene (see also Fig. 3.5b). The graphene mobility for both devices is on the order of 20,000 cm^2/Vs, which is a lower bound as it is determined from two-terminal measurements (see Fig. 3.2 and Fig. 3.3).

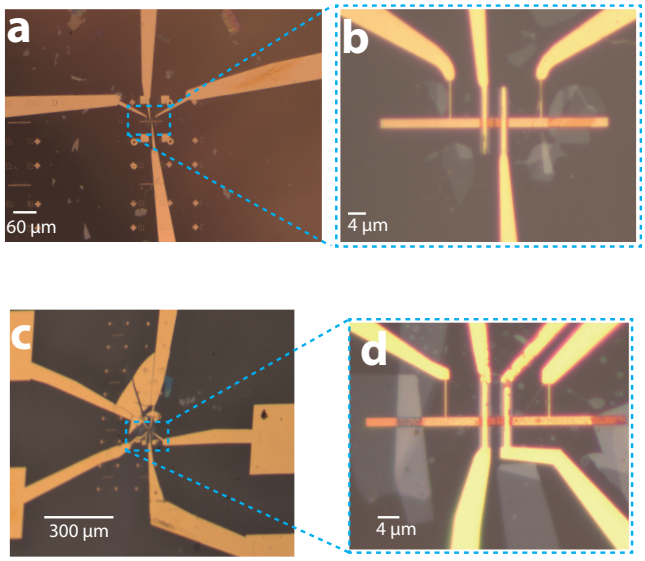

Fig. 3.1: Optical microscope images of the graphene-based THz photodetectors. **a)** 10x magnification image of Device A, showing the metallic rods contacting the antenna branches and source-drain electrodes. **b)** 100x magnification image of Device A, displaying the area of the photodetector containing the antenna/gate structure, source-drain electrodes and "H-shaped", h-BN encapsulated graphene. **c)** 5x magnification image of Device B and **d)** 100x magnification image of Device B.

Additionally, we fabricate a reference device with Hall bar geometry configuration by following the fabrication procedure described above. We achieve a high mobility of 100,000

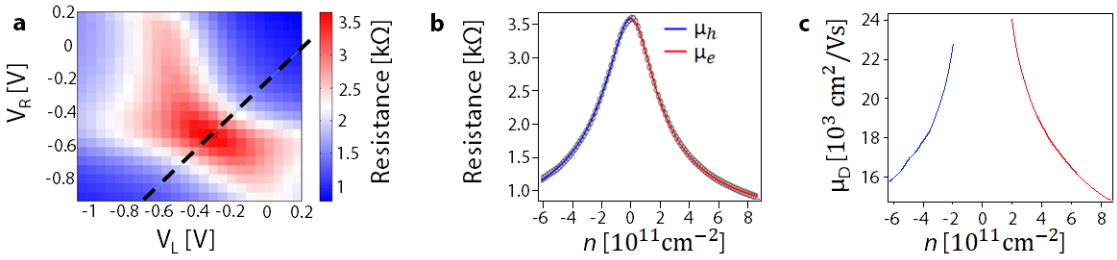

Fig. 3.2: a) Measured resistance map as a function of the right gate (left axis) and left gate (bottom axis) for Device A. **b)** Resistance as a function of graphene charge carrier density (linecut in dashed line shown in **a)**). We fit the resistance R curve using the model from Ref.[85], where $R = R_c + (L/w)(\mu e n)^{-1}$, R_c is contact resistance, L is channel length, w is channel width, μ is mobility, e is elementary charge, and the carrier density is given by $n = \sqrt{(n^*)^2 + (\beta(V_g - V_{\mathbf{Dirac}}))^2}$. Here n^* is the residual doping concentration, V_g is gate voltage, $V_{\mathbf{Dirac}}$ is the gate voltage that corresponds to the Dirac point, and $\beta = \epsilon_0 \epsilon_{\mathbf{hBN}}/d_{\mathbf{hBN}} e$, where ϵ_0 is vacuum permittivity, $\epsilon_{\mathbf{hBN}}$ the dielectric constant of hBN and $d_{\mathbf{hBN}}$ the thickness of the bottom hBN. We obtained 22,000 and 19,000 $\mathrm{cm}^2/\mathrm{Vs}$ for electron (red) and hole (blue) mobility, respectively. We extracted a contact resistance of $R_c = 126\ \Omega$ ($3.8\ \mathrm{k}\Omega \cdot \mu\mathrm{m}$), and a residual doping concentration of $n^* = 1.6{\cdot}10^{11}\ \mathrm{cm}^{-2}$. **c)** Carrier mobility as a function of graphene charge carrier density extracted from the conductance measurement[34], where blue (red) corresponds to hole (electron) mobility.

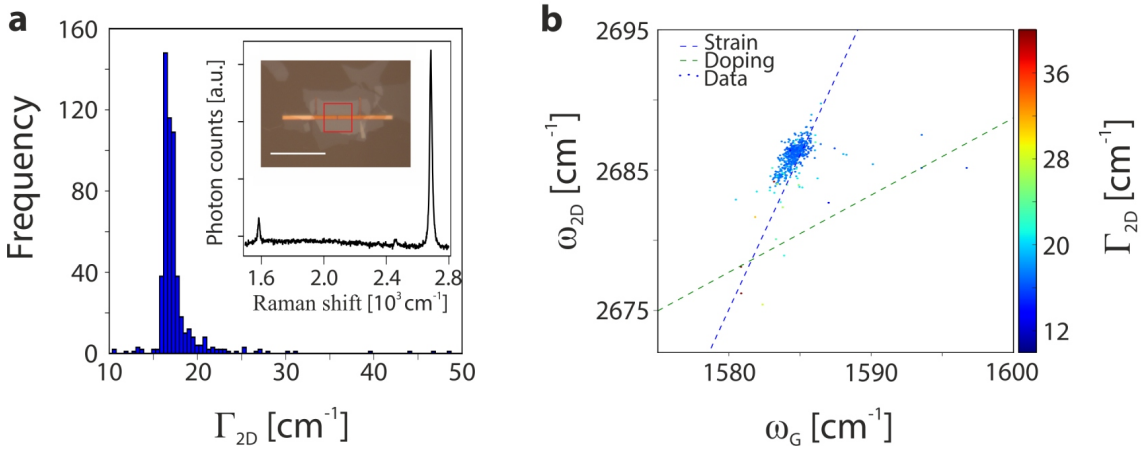

Fig. 3.3: Raman spectroscopy measurements of Device A. **a)** Histogram plot of the full-width-half-maximum of the graphene 2D peak ($\Gamma_{\mathbf{2D}}$) across the ~15x15 $\mu\mathrm{m}^2$ region marked in red on the optical picture (see inset). The white scale bar corresponds to 30 μm. The inset shows a typical Raman spectrum of the monolayer graphene. The mean $\Gamma_{\mathbf{2D}}$ is ~17.5 cm^{-1}, characteristic of high quality single layer graphene[86]. **b)** 2D-peak versus G-peak frequency ($\omega_{\mathbf{2D}}$ and $\omega_{\mathbf{G}}$, respectively) extracted from the same Raman map as in panel **a**. The colorbar represents the $\Gamma_{\mathbf{2D}}$ of the recorded spectrum. The data shows low doping, as confirmed in transport measurements (see Fig. 3.2), and moderate levels of strain[86].

$\mathrm{cm}^2/\mathrm{Vs}$ in this device as shown in Fig 3.4.

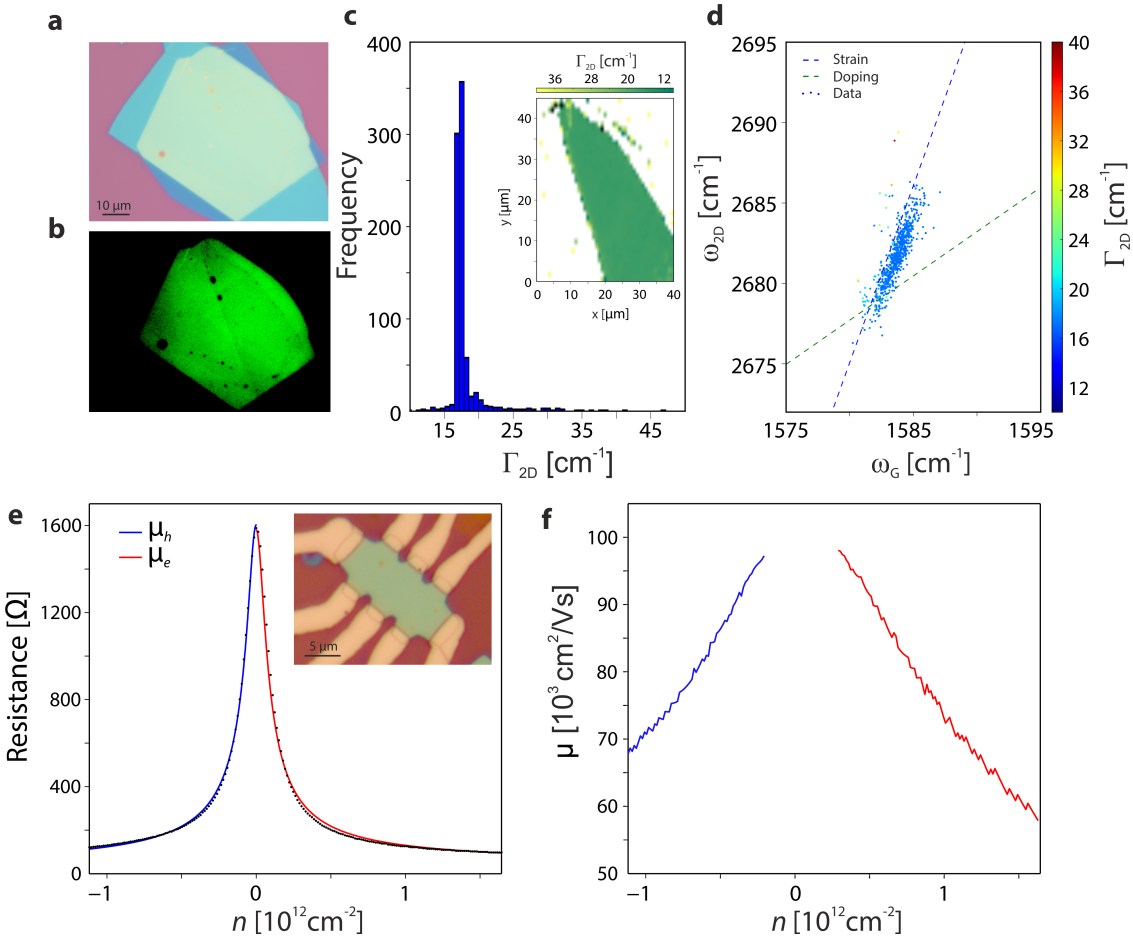

Fig. 3.4: Characterization of the Hall bar reference device fabricated following the same procedure as the photodetector (see Methods). **a)** Optical image of the initial hBN/graphene/hBN stack. **b)** Optical image shown in panel **a** with enhanced contrast. The graphene flake is optically visible (compare the graphene shape with the Raman map shown in the inset of panel **c**). **c)** Histogram plot of the Raman scan (see inset) showing the full-width-half-maximum of the graphene 2D Raman peak (Γ_{2D}). The mean Γ_{2D} is $\sim$ 18.1 cm^{-1}, characteristic of high quality single layer graphene. **d)** Scattering plot of the 2D-peak versus the G-peak frequency (ω_{2D} and ω_G, respectively), where the colorbar represents the Γ_{2D} of the recorded spectrum (inset of panel **c**). The Raman data shows comparable behavior as the photodetector (see Fig. 3.3b) with low Γ_{2D}, low doping and moderate levels of strain[86]. **e)** Resistance as a function of the charge carrier density of the measured Hall bar device (see inset). We fit the resistance R curve using the model from Ref.[85], and obtained 103,000 and 96,000 cm^2/Vs for the electron (red) and hole (blue) mobilities, respectively. **f)** Carrier mobility as a function of the charge carrier density extracted from the conductance measurement[34], where blue (red) corresponds to hole (electron) mobility. These results show that a mobility of 100,000 cm^2/Vs for these kind of photodetector devices is realistic, and therefore a detection speed in the 10 ps-range can be achieved.

3.3 Experimental THz setup

We characterize the performance of the THz photodetector devices using two different setups, both containing a THz laser and optical components to focus the light at our THz detector. One setup contains a pulsed quantum cascade laser (QCL) operating at 3.4 THz, with an expected rise time <1 ns. We use two Picarin (tsupurica) lenses to focus the light. We use this setup for Figs. 3.5d, 3.9c and 3.10. The other setup contains a continuous wave THz beam from a gas laser (FIRL 100 from Edinburgh Instruments) providing a maximum output power in the range of a few tens of milliwatts, and frequencies of 1.83, 2.52, 3.11 and 4.25 THz. We use a parabolic mirror to focus the light with a focal distance of 5 cm. The THz light is usually modulated at 266 Hz by an optical chopper and the generated photocurrent is measured using a pre-amplifier and/or lock-in amplifier (Stanford). We verified that the output THz beam was strongly polarized (only 2% of residual unpolarized light) and mounted the detector with the antenna axis parallel to the polarization. We measure the THz power by using a pyroelectric THz detector from Gentec-EO placed at the sample position. We use typical incident THz powers in the range of several microwatts to several milliwatts.

3.4 Device working principle

Our THz photodetector is based on a novel design (see Fig. 3.5a-c), which works as follows. The detector contains a dipole antenna that is located ∼15 nm below a graphene channel. The antenna consists of two branches that are separated by a very narrow gap, with a size on the order of 100 nm. This antenna gap serves for focusing the incoming THz radiation into a very small spot in the graphene channel. Here, the concentrated field of the antenna leads to (intraband) absorption and the subsequent creation of hot carriers[27]. Since the creation of a photoresponse from hot carriers requires a gradient in the Seebeck coefficient, we use the antenna branches simultaneously as split gates. We apply appropriate voltages (V_L and V_R) to the left and right antenna branch, and through capacitive coupling this creates a *pn*-junction in the graphene channel, and thereby a THz-induced photoresponse. Thus, the antenna simultaneously creates the photoactive area in the graphene channel (located around the *pn*-junction, see Fig. 3.5c) and funnels incident radiation to this photoactive area, due to the very strong field enhancement of incident THz radiation above the gap between the two antenna branches (see Fig. 3.5a-b).

Compared to previous antenna-integrated, graphene-based THz detectors[39,66,67,78–82], the advantage of our design is that the antenna gap is much smaller (100 nm *vs*. several microns), which means that the THz intensity is greatly enhanced (∼4 orders of magnitude, see Fig. 3.5a). Also, there is no direct electrical connection between the antenna and the graphene, which means that there is no need for impedance matching to assure current flow between antenna and graphene. The fact that we simultaneously use our antenna for focusing light and as split gate, has the advantage that there automatically is very good overlap between the region where the incoming THz radiation is focused and the photoactive region of the graphene channel (see Fig. 3.5a-c). Furthermore, we use hBN-encapsulated graphene, which leads to graphene with high mobility and low residual

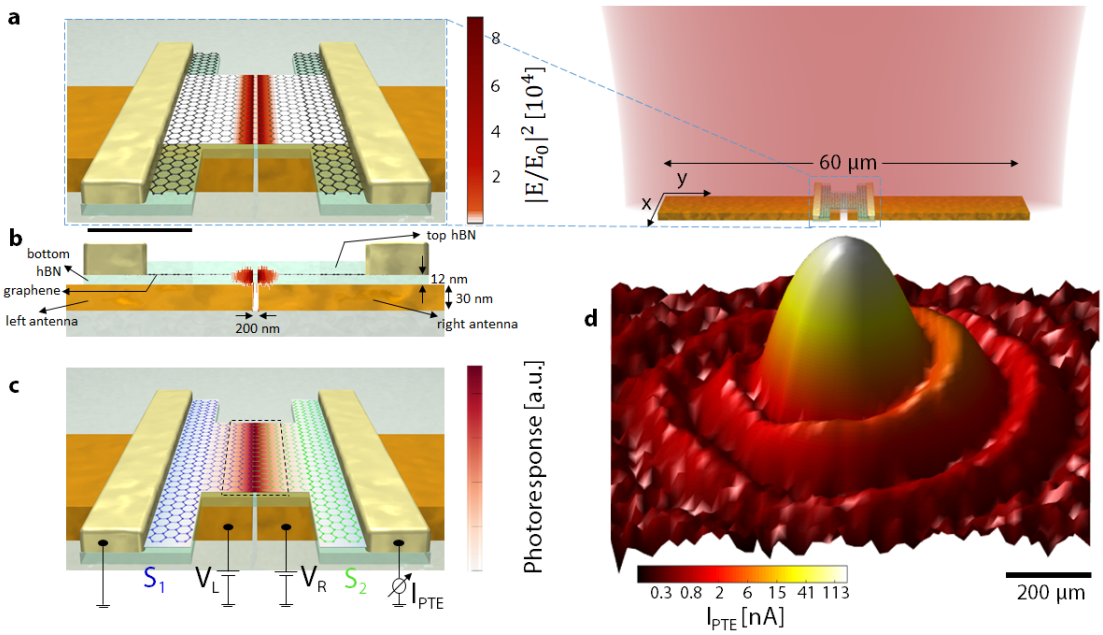

Fig. 3.5: a) Schematic representation (right; not to scale) of the antenna-integrated *pn*-junction device and a zoom of the central part of the THz PTE detector (left; to scale), consisting of an "H-shaped" graphene channel, contacted by source and drain electrodes. Underneath the graphene channel, there are two antenna branches that concentrate the incident THz light around the antenna gap region. The color map superimposed on the device shows the simulated power profile ($|E/E_0|^2$, where E_0 is the incident electric field) at a position 5 nm below the graphene channel. The black scale bar corresponds to 1.6 μm. **b)** Side view of the device design, with the superimposed color map again indicating the normalized power profile as in panel **a**. The region where the field is strongly enhanced by the antenna overlaps with the central part of the graphene channel. **c)** Same as panel **a**, now indicating how the antenna branches serve as local gates by applying voltages V_L and V_R. Appropriate voltages will create a *pn*-junction in the central part of the graphene channel, directly above the antenna gap (which is where incident THz light is concentrated by the antenna). The color map superimposed on the device is a simulation that shows the photoresponse created by local photoexcitation, varying the position of photoexcitation (see also section 3.8). The largest photoresponse is created when photoexcitation occurs around the junction region. The photoresponse then decreases exponentially when moving away on both sides from the junction, with the exponential decay length given by the cooling length ℓ_{cool}. The photoactive area (dashed rectangle) therefore has a length $2 \cdot \ell_{cool}$, and a width w, which is the width of the central part of the graphene channel. **d)** Photocurrent image (log-scale) obtained by scanning the detector in the focal plane of a focused laser beam at 3.4 THz. We use our QCL with an average power of 84.1 μW, and a peak irradiance in the center of the focus of 1200 W/m^2. The THz light is polarized parallel to the antenna axis. The observation of the Airy pattern with multiple observable rings indicates excellent detector sensitivity.

doping. This means that the resistance of the graphene channel will be low, and we can tune the system relatively close to the Dirac point (point of lowest carrier density), where the Seebeck coefficient is largest. Finally, we pattern the graphene channel into an "H-shape" with a relatively narrow (micron-sized) width. The narrow width of the central part of the channel leads to an enhanced photoresponse, as the hot carriers will have a higher temperature. The wider sides of the graphene channel reduce overall device resistance by minimizing contact resistance.

3.5 Results

We first scan our photodetector (Device A) across the THz focus using motorized stages (in the QCL setup, as described in Section 3.3). The dipolar antenna, with a length of 60 μm, is smaller than the THz focus (FWHM $\sim$200 μm), allowing us to spatially map out the intensity of the THz focus through the photocurrent $I_{\mathbf{PTE}}$. The results show a clear Airy pattern (see Fig. 3.5d), where we are able to observe several rings of the diffracted beam pattern. This suggests that our THz photodetector is very sensitive, considering that these rings contain only a very small fraction of total incident power of the THz beam ($P_{\mathbf{in}}$ = 84.1 μW).

Before proceeding with quantifying the sensitivity, we first exploit the gate-tunability to identify the photocurrent generation mechanism and determine the optimal operating point of our THz detector, by mapping out the photoresponse as a function of gate voltages $V_{\mathbf{L}}$ and $V_{\mathbf{R}}$ (see Fig. 3.6a). These measurements were done with the THz gas laser at 2.52 THz, and using Device A. The gate voltages independently control the carrier density (Fermi energy) of the two graphene regions and therefore the Seebeck coefficients S_1 and S_2. The Seebeck coefficient of graphene has a non-monotonous dependence on carrier density, where it first increases upon approaching the Dirac point and then changes sign when crossing the Dirac point, *i.e.* when going from hole to electron doping or vice versa (see Fig. 3.6b). Since the generated photocurrent $I_{\mathbf{PTE}} \propto (S_1 - S_2)$, this leads to the characteristic sixfold pattern, first shown in Ref.[44] for visible light, and explained in Fig. 3.6b. The fact that we also observe a sixfold pattern strongly suggest that our THz photoresponse is dominated by the PTE effect. To further confirm that the PTE mechanism dominates over alternative photocurrent mechanisms, such as bolometric and photogating effects, we measured the photocurrent as a function of bias voltage applied between the source and drain contacts. The drain current increases linearly with applied bias voltage, whereas the photocurrent remains constant (see Fig. 3.7), in contradiction with what is expected for the bolometric and photogating effects. Thus, these results show that the photo-thermoelectric effect is responsible for the observed THz photoresponse. We find the largest photoresponse in the *pn*-junction and *np*-junction regimes, as expected, relatively close to the Dirac point.

We now proceed with quantifying the sensitivity of our THz photodetector. First, we identify the largest responsivity $\mathbb{R} = I_{\mathbf{PTE}}/P_{\mathbf{diff}}$ at the optimal gate configuration for Device A. We note that the responsivity that we use is the responsivity *normalized by the power in a diffraction-limited spot with NA = 1*. In some of the literature, a responsivity is provided

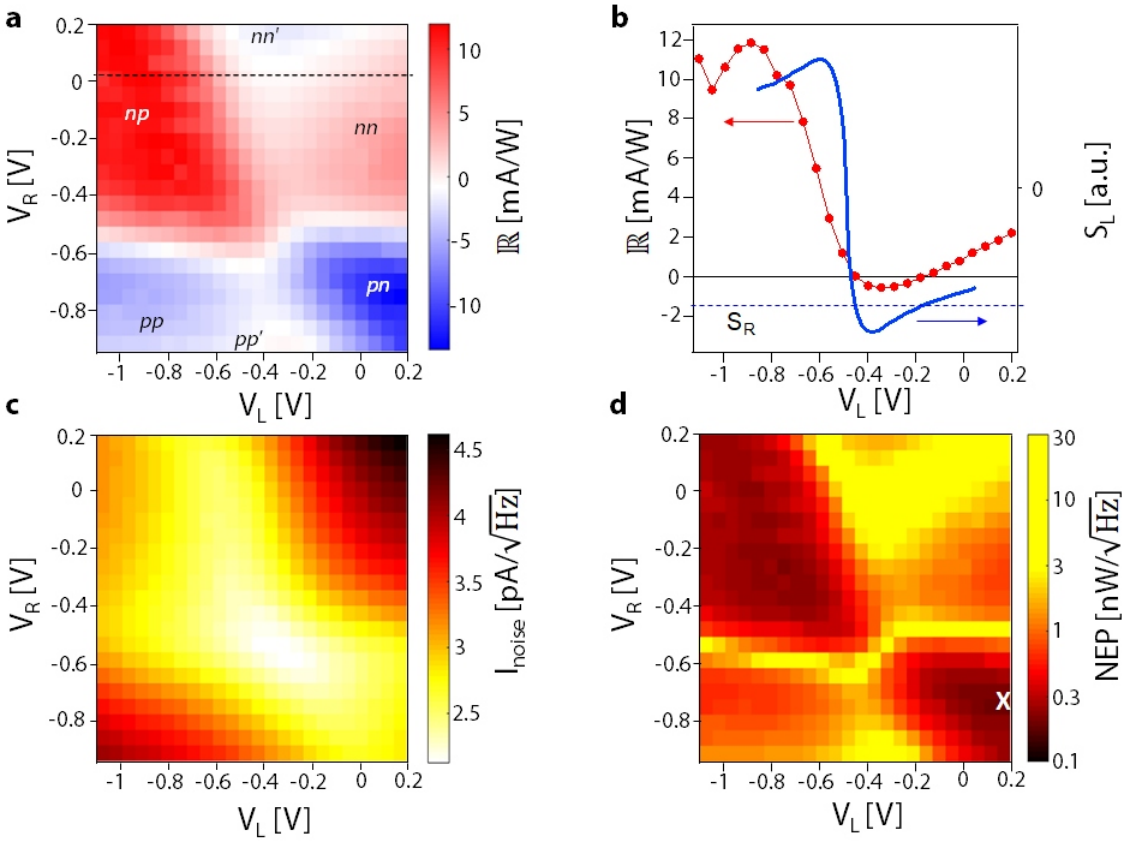

Fig. 3.6: a) Photoresponse as a function of voltages applied to the two antenna branches/gates, with radiation at 2.52 THz. We use our THz gas laser with an average incident power of $P_{in} = 5$ mW, and a peak irradiance in the center of the focus of $1.8{\cdot}10^4$ W/m^2. The THz light is polarized parallel to the antenna axis. The sixfold pattern, as in Refs.[43,44], indicates that the photoresponse is generated through the PTE effect. The photoresponse is the photocurrent normalized by the power in a diffraction-limited spot, *i.e.* the responsivity $\mathbb{R}$. The maximum responsivity occurs in the *pn*- and *np*-regions. **b)** Line cut at the location of the dashed line in panel a, showing a double sign change (red dots and line; left vertical axis) as a function of carrier density (controlled through gate voltage V_L). The blue line represents the Seebeck coefficient (calculated from the experimentally obtained graphene mobility, right vertical axis). The double sign change occurs due to the non-monotonous dependence of the Seebeck coefficient on carrier density: for a constant Seebeck coefficient in one region (dashed horizontal line), the Seebeck coefficient of the other region is first higher, then lower and then again higher, giving rise to two sign changes, as indeed observed experimentally. **c)** The extracted Johnson noise current, calculated from the resistance that was measured simultaneously with the result in panel **a**. **d)** The noise-equivalent power (NEP), extracted from the results in panels **a** and **c**, normalized to a diffraction-limited spot. The white cross indicates the gate configuration that corresponds to the lowest NEP: the left (right) gate at 0.20 V (-0.72 V), corresponding to an electron density of $7.5{\cdot}10^{11}$ cm^{-2}, $E_F = +100$ meV (hole density of $3.6{\cdot}10^{11}$ cm^{-2}, $E_F = -70$ meV).

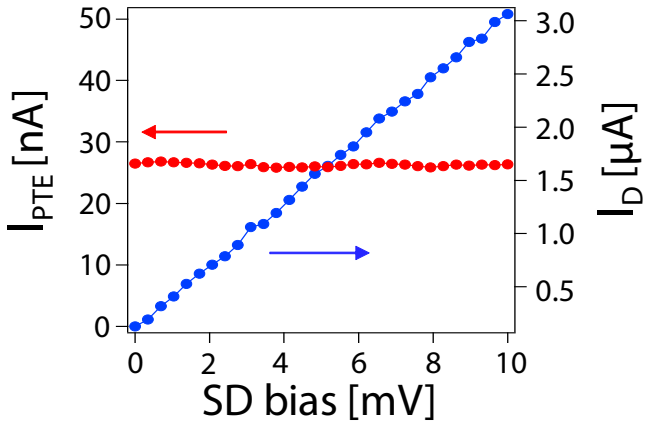

Fig. 3.7: Photocurrent and drain current measured simultaneously as a function of applied bias voltage between the source and drain contacts. We notice a linear increase of the drain current while increasing the bias, whereas the photocurrent remains constant.

that is normalized by the amount of power that is actually incident in the experiment $P_{\mathbf{in}}$. However in the case where the wavelength is larger than the photodetector device this number does not only depend on the device performance, but also on how well the THz light is focused. Alternatively, one can use the responsivity normalized to the power that is absorbed in the actual graphene channel or in the photoactive area, which would yield an artificially high number[42], as it is impossible to focus the THz light in such a small area. Here we choose the responsivity normalized by the incident power in a diffraction-limited spot, because this is arguably the most technologically relevant number (as this represents what will be reached when combining the detector with an optimized focusing system, such as using a silicon hemispherical lens[79–81]), and it is the convention that is most commonly used in the literature on THz photodetection (see also Table 3.2). We calculate the power in a diffraction-limited spot using $P_{\mathbf{diff}} = P_{\mathbf{in}} \cdot A_{\mathbf{diff}}/A_{\mathbf{focus}}$, where $P_{\mathbf{in}}$ is the measured total incident THz power, $A_{\mathbf{diff}}$ is the calculated area of a diffraction-limited spot and $A_{\mathbf{focus}}$ is the measured area of the focused THz beam. Typically, we have $A_{\mathbf{diff}}/A_{\mathbf{focus}} \approx 1/60$ (corresponding to a NA of $\sim$0.13 for our focusing system based on a parabolic mirror). From Fig. 3.6a we extract a maximum responsivity of $\mathbb{R} = 14$ mA/W (32 V/W). For Device B, we find a maximum responsivity value of $\mathbb{R} = 25$ mA/W (105 V/W) as shown in Fig. 3.8. In both cases the THz light was at 2.52 THz (corresponding to a wavelength of 118.96 μm, 84 cm^{-1}).

Using the extracted responsivity, we now determine the sensitivity of the detector. For this, we note that our detector operates without bias, which means that it is limited by the Johnson or thermal noise, given by: $I_{\mathbf{noise}} = \sqrt{\frac{4k_{\mathbf{B}}T\Delta f}{R}}$. Here, $k_{\mathbf{B}}$ is the Boltzmann constant, T is the temperature of operation, Δf is the spectral bandwidth and R the resistance. We show the Johnson noise current of Device A as a function of the two gates voltages in Fig. 3.6c, calculated from the measured resistance R. The resistance was measured simultaneously with the photoresponse in Fig. 3.6a, which we used to de-

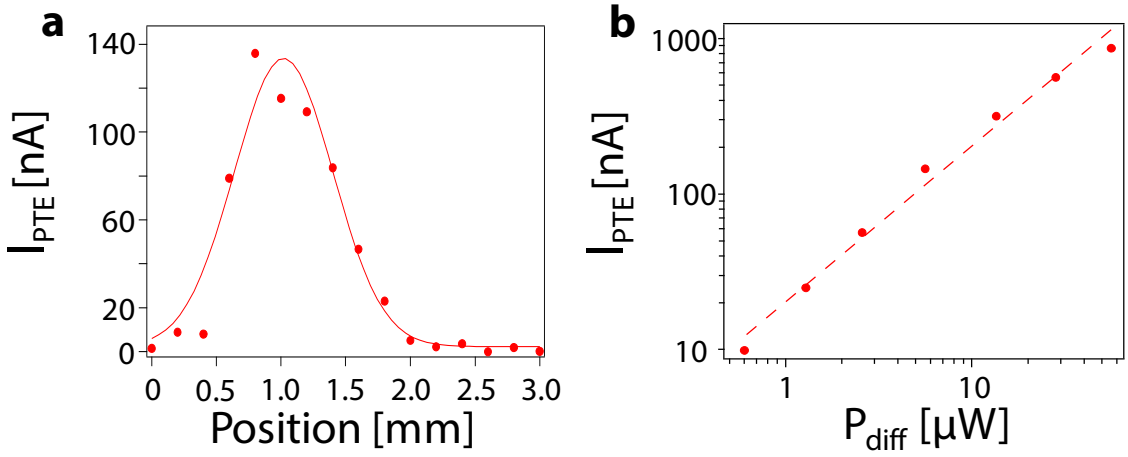

Fig. 3.8: Photoresponse of Device B. **a)** Photocurrent generated as a function of the scan position of the device. The red circles correspond to the experimental points and the red line to the Gaussian distribution fit. We obtain a beam focus FWHM of 897 μm at 2.52 THz. We observe a maximum $I_{\mathbf{PTE}}$ of 136 nA for an incident power ($P_{\mathbf{in}}$) of 2.88 mW ($P_{\mathbf{diff}} = P_{\mathbf{in}} \cdot A_{\mathbf{diff}}/A_{\mathbf{focus}} = 7.1$ μW). Thus, the responsivity is $\mathbb{R} = I_{\mathbf{PTE}}/P_{\mathbf{diff}} = 19$ mA/W (80.4 V/W). The sample was electrostatically doped with the left (*n*-doped, 60 meV) and right gate (*p*-doped, 50 meV) forming a *pn*-junction. **b)** Photocurrent as a function of incident power. It shows a linear trend over three orders of magnitude according to the fit displayed in dashed line. The maximum responsivity was $\mathbb{R} = 25$ mA/W (105 V/W), from a photocurrent of $I_{\mathbf{PTE}} = 145$ nA, for an incident power of $P_{\mathbf{in}} = 2.28$ mW ($P_{\mathbf{diff}} = 5.6$ μW, for the same beam focus at 2.5 THz and *pn*-junction configuration as in panel **a)**. Using this responsivity and the Johnson noise that corresponds to the 4.2 kΩ measured device resistance, we find an NEP of 80 pW/$\sqrt{\mathbf{Hz}}$.

termine the responsivity $\mathbb{R}$. As expected, we see that a higher noise current occurs for lower resistance values (away from the Dirac point), whereas we obtain lower noise values closer to the Dirac point, where the graphene resistance is higher. The photodetection sensitivity is given by NEP$= I_{\mathbf{noise}}/\mathbb{R}$, which we show as a function of the two gate voltages in Fig. 3.6d. The lowest values for the NEP occur at the *pn*- and *np*-regions close to the Dirac point, where the responsivity is highest and the noise is lowest. The lowest value of the NEP map was 200 pW/$\sqrt{\mathbf{Hz}}$ for Device A and 80 pW/$\sqrt{\mathbf{Hz}}$ for Device B (see Fig. 3.8).

An important characteristic of an ideal THz detector is having a large range of powers over which the response is linear, *i.e.* a large dynamic range. Thus, we measure the photocurrent *vs.* $P_{\mathbf{diff}}$ for four different THz frequencies as shown in Fig. 3.9a. We vary the THz power over more than 3 orders of magnitude (using the THz gas laser setup), and fit the data with a simple power law $I_{\mathbf{PTE}} \propto P_{\mathbf{diff}}^{\gamma}$. We obtain for Device A at 2.5 THz a power of $\gamma = 1.1 \pm 0.2$ and for Device B $\gamma = 1.1 \pm 0.15$ (95% confidence intervals). This shows that the photoresponse depends linearly on the THz power over a range of more than three orders of magnitude. The reason for the linear photoresponse as a function of power is the fact that the photodetector operates in the weak heating regime, where $\Delta T \ll T_{\mathbf{ambient}}$, *i.e.* the change in temperature of the electronic system is smaller than the ambient temperature $T_{\mathbf{ambient}}$. When ΔT approaches $T_{\mathbf{ambient}}$, we expect a sub-linear dependence of photocurrent on power, with an exponent that tends to $\gamma = 0.5$.

Regarding the range of frequencies where our detectors operate, we note that this is only limited by the antenna structure. The reason behind the spectrally ultra-broad photoresponse of graphene is the efficient heating of the electrons, which occurs irrespective of the wavelength of the incident light, *i.e.* whether intraband or interband light absorption occurs[23,27]. We characterize the spectral response of our detector by measuring the responsivity, while varying the frequency from 1.83 to 4.25 THz (see Fig. 3.9b). We observe a trend where the responsivity peaks around 3 THz. This corresponds reasonably well with the antenna being optimized for a frequency of 2 THz using full wave simulations (see Fig. 3.9b). The discrepancy likely comes from the fact that a simplified structure was simulated, which didn't contain all the metallic parts that the actual device has. Importantly, these results confirm that the spectral range where the THz detector operates is currently limited only by the antenna. Thus, using more spectrally broad antennas or a combination of antennas one could extend the spectral range of our photodetector, covering the spectrum all the way from the ultraviolet, through the visible and infrared to the terahertz.

3.6 Speed measurements and calculations

In the following, we discuss the speed of our PTE THz photodetector. We analyze the speed in Fig. 3.9c, where we rapidly switch the THz radiation on (white) and off (yellow) using our pulsed THz QCL. We observe that the photoresponse of our detector $V_{\mathbf{PTE}}$ closely follows the laser switching behavior. We quantify the detector speed by fitting the $V_{\mathbf{PTE}}$ rise and fall dynamics (see Fig. 3.10) with simple exponential equations, and obtain an exponential (1/e) response time of 32$\pm$11 ns, corresponding to a bandwidth of $\sim$5 MHz. In this measurement, the speed is most likely limited by the measurement

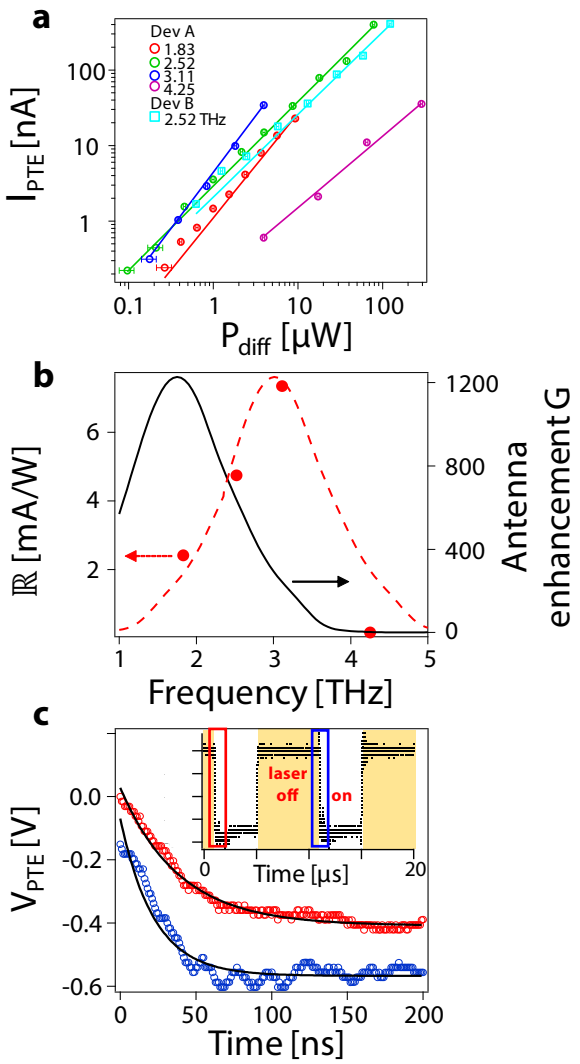

Fig. 3.9: a) Photocurrent as a function of THz laser power (in a diffraction-limited spot) P_{diff} in log-log scale. All round data points correspond to Device A, whereas the light blue squares correspond to Device B. The lines through the experimental data points are fits according to $I_{\mathrm{PTE}} \propto P_{\mathrm{diff}}^{\gamma}$. The obtained exponent is close to 1 for all data sets. For Device A, these data correspond to a gate configuration of $V_{\mathrm{L}} = 0$ V and $V_{\mathrm{R}} =$ -0.67 V, corresponding to an electron (hole) density of $4.2{\cdot}10^{11}$ ($-2.7{\cdot}10^{11}$) cm^{-2}. **b)** Responsivity $\mathbb{R}$ as a function of THz wavelength (red dots, left vertical axis), with the same (sub-optimal) gate configuration as in panel **a**. The black line (right vertical axis) shows the result for the antenna-induced absorption enhancement in the graphene channel. The red dashed line illustrates the trend of the experimental points. **c)** Results of the pulsed laser experiment, where the photocurrent was amplified by a fast current pre-amplifer (Femto) and the data were acquired with a fast oscilloscope. The inset shows how the photovoltage V_{PTE} follows the switching of the pulsed laser. The red and blue (plotted with an offset) open dots show the obtained photovoltage in a small time window marked in the inset, with the black line giving the result of exponential fits with timescales of 40 (24) ns for the red (blue) curve.

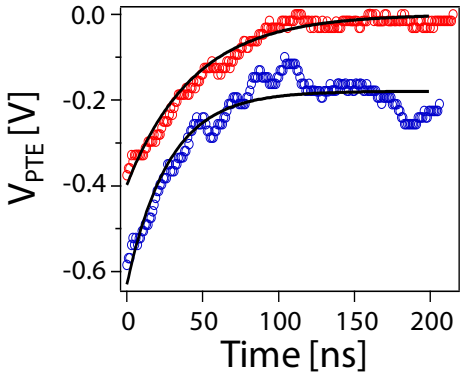

Fig. 3.10: Results of the pulsed laser experiment, showing the fall time corresponding to the two regions (red and blue, the latter one plotted with an offset) of the inset of Fig. 3.9c of the main text. The open dots show the acquired photovoltage and the black lines represent the fit results with the exponential fits. We obtain an exponential fall time of 47 (28) ns for the red (blue) curve. As in the case of the rise time determination in the main text, this timescale is limited by the current amplifier with a bandwidth of 3.5 MHz.

electronics, namely by the 3.5 MHz bandwidth of the current pre-amplifier, rather than by the PTE THz detector itself. Indeed, the intrinsic speed of the detector is expected to be significantly higher, since the PTE effect that drives the photoresponse relies on the heating and cooling dynamics of the photoexcited carriers in graphene that occur at picosecond time scales.[23,43–45] The hot carriers are created by light absorption that quickly relax ($<$100 fs)[23] into a local hot equilibrium Fermi-Dirac distribution by electron-electron scattering. Subsequent cooling mechanisms include electronic heat diffusion and electron–phonon scattering ($\sim$1 ps)[43–45]. Hence the upper limit of the response time is limited by the RC-time of the detector.

The electrically-limited operation frequency of the detector is related to the RC-time constant $\tau = RC$, with R total graphene resistance (graphene sheet resistance $R_{\mathbf{SLG}}$ and contact resistance $R_{\mathbf{contact}}$), and C total graphene capacitance. We obtain a value of 925 Ω for $R_{\mathbf{SLG}}$ for a Fermi level of 0.1 eV using the extracted Device A mobility of 20,000 cm^2/Vs. We also consider the $R_{\mathbf{contact}}$ extracted from Device A with a value of 507 Ω (3.8 k$\Omega \cdot \mu$m). In order to calculate C, we use electrostatic simulations performed in COMSOL in collaboration with Elefterios Lidorikis group. We apply an electrostatic potential with opposite sign on each antenna branch as depicted in Fig. 3.11. We then determine the surface charge density of graphene using the parallel plate capacitor model with hBN dielectric permittivity ($\epsilon_{\mathbf{hBN}} = 3.5$) as shown in Fig. 3.12. We obtain a capacitance in the order of 20 fF.

The operating speed is then given by the rate $f = (2\pi\tau)^{-1}$. The rise time $\tau_{\mathbf{rise}}$ is the measure of the photodetector response speed to a stepped light input signal. It is the time required for the photodetector to increase its output signal from 10% to 90% of the final steady-state output level. The rise time is calculated as $\tau_{\mathbf{rise}} = \tau \cdot \ln(9) = (2\pi f)^{-1} \cdot \ln(9) = 0.35/f$. Performing this calculation, we obtain a rise time of 56 ps, corresponding to

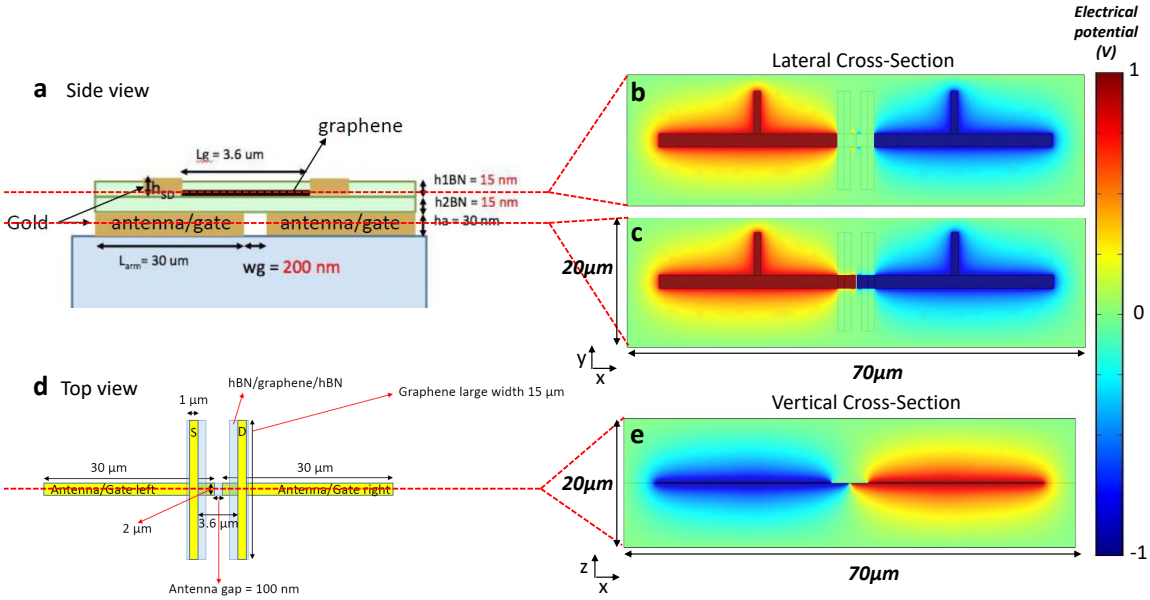

Fig. 3.11: Electrostatic simulations. **a)** Side view of the device. **b)** and **c)** represent the lateral cross section view of the electrostatic potential profile at different device levels, across the antenna branches and across the graphene sheet respectively. We point out the opposite sign voltage applied to each antenna branch to form the graphene pn-junction configuration. **d)** Top view of the device. **e)** Vertical cross section view of the electrostatic potential profile.

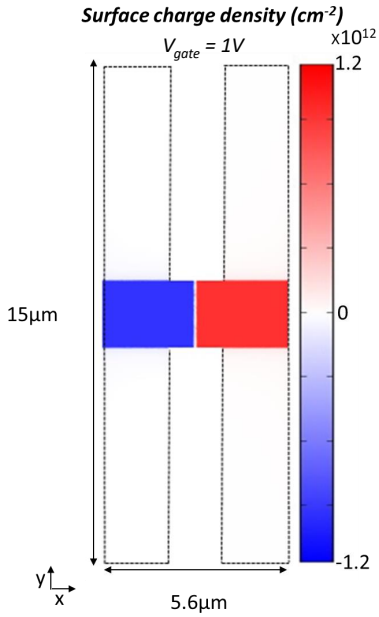

Fig. 3.12: Surface charge density profile distribution across the graphene sheet.

a detection rate of 6 GHz for our device with a mobility of 20,000 cm^2/Vs. For a device with a mobility of 100,000 cm^2/Vs (see reference device in Fig. 3.4), we find 9 ps, corresponding to 40 GHz. Thus, extremely fast THz photodetection with switching times in the picosecond range should be possible.

3.7 Analytical model and discussion

We now discuss more of the underlying physics of the PTE detector, using a simple analytical model that provides the rationale behind our detector design. Owing to the difference in Seebeck coefficients at the *pn*-junction, a local photo-thermoelectric voltage is created, which leads to the flow of a photocurrent between the source and drain contacts that are connected to the graphene channel. The PTE photocurrent is then given by[43]

$$I_{PTE} = \frac{(S_1 - S_2)\,\Delta T}{R} \quad , \tag{3.1}$$

where S_1 and S_2 are the Seebeck coefficients (also called thermopower) of the two regions of the graphene channel that are independently controlled by the gates/antenna branches, ΔT is the temperature increase of the electronic system induced by THz radiation, and R is the total electrical resistance, accounting for the graphene and contact resistances. It is worth mentioning that this current is generated under zero applied source-drain bias voltage, resulting in very low detector noise (Johnson noise) and extremely low power consumption.

Graphene is an ideal material to exploit the PTE effect for THz detection, because the term $(S_1 - S_2)\,\Delta T$ can be large and R is typically small, in particular for high-quality, hBN-encapsulated graphene. The Seebeck coefficient of graphene is intrinsically quite large, on the order of 100 $\mu V/K$[87] and S_1 and S_2 are independently tunable through the gates, meaning that $(S_1 - S_2)$ can be maximized. Furthermore, ΔT can be large in graphene (up to several thousand K), because of efficient heating of the electrons after absorbing THz light, due to strong electron-electron interactions, and because the hot carriers are relatively weakly coupled to the crystal lattice[27].

Our photodetector design maximizes the PTE THz photoresponse, particularly by maximizing ΔT and minimizing R. From a simple heat equation, the temperature increase ΔT (averaged over all charge carriers in the photoactive area) is given by

$$\Delta T \approx \frac{P_{\mathbf{abs}}}{A_{\mathbf{active}}\Gamma_{\mathbf{cool}}} \tag{3.2}$$

where $P_{\mathbf{abs}}$ is the amount of THz power that is absorbed in the active area of the graphene channel and $\Gamma_{\mathbf{cool}}$ is the heat conductivity that describes the coupling of the heated electron systems to its environment. The photoactive area is given by $A_{\mathbf{active}} = 2\ell_{\mathbf{cool}} \cdot w$, where $\ell_{\mathbf{cool}}$ is the hot-carrier cooling length, which can be seen as the length scale over which hot carriers can move before cooling down (typically 0.5 – 1 μm at room temperature[23,43–45,88], see also Fig. 3.5c). In the case of hBN-encapsulated graphene, $\Gamma_{\mathbf{cool}}$ is the out-of-plane, interfacial heat conductivity where hot graphene carriers couple to hyperbolic hBN phonons[45]. We optimize ΔT by maximizing $P_{\mathbf{abs}}$ and minimizing

$A_{\mathbf{active}}$. We maximize the amount of absorbed THz power $P_{\mathbf{abs}}$ by using a dipole antenna with a narrow gap, which focuses the incoming THz radiation down to the small (compared to the THz radiation wavelength) graphene photoactive region. We further maximize ΔT by using a narrow channel width w of 2 μm. Basically, the smaller the area where the incident power is absorbed, the smaller the amount of electrons that will share the heat, and therefore the larger the increase in temperature of the electronic system, ΔT.

In order to further increase the responsivity, we reduce the overall resistance R of the device, and optimize the shape of the graphene channel. We achieve low R by using high-quality hBN-encapsulated graphene (see Fig. 3.5b)[34,56]. This method enables mobility values as high as 100,000 cm^2/Vs at room temperature, and low levels of intrinsic doping (see Fig.3.4). We furthermore pattern the graphene channel in an "H-shape" (see Fig. 3.5a), in order to reduce the overall device resistance R. This shape is crucial because it has a small width w in the central part of the channel – ensuring small $A_{\mathbf{active}}$ and thus large ΔT – while having a larger width towards the contacts – minimizing the graphene sheet resistance. Furthermore, the large interface with the source and drain contacts minimizes the contribution of contact resistance to the overall resistance R.

Based on the analytical model for the PTE response, we now examine our experimental results quantitatively. We have measured a photocurrent of $I_{\mathbf{PTE}} = 1.14$ μA (Device A, 2.5 THz) for an incident power of $P_{\mathbf{in}} = 5$ mW (focused to a spot size $A_{\mathbf{focus}}$, see Methods). Using Eq. 3.1 with $(S_1 - S_2) = 160$ μV/K (estimated from Ref.[26]) and $R = 2.3$ kΩ (measured), we find an experimental temperature increase of $\sim$16 K (confirming the weak heating regime). Then using Eq. 3.2 with interfacial heat conductivity $\Gamma_{\mathbf{cool}} = 7{\cdot}10^4$ W/m^{2}K (determined in Ref.[45]), cooling length $\ell_{\mathbf{cool}} = 510$ nm (from the mobility and interfacial heat conductivity), and channel width $w = 2$ μm (measured), we find the absorbed power (in the active area of the graphene channel) to be $P_{\mathbf{abs}} = 2.3$ μW. We compare this value with the absorbed power we find from numerical simulations of the antenna-graphene structure, using the same irradiance as in the experiment (see Methods). These simulations give an absorbed power (in the entire graphene channel) of $P_{\mathbf{abs,sim}} = 7$ μW (at 2.5 THz). This number is close to the number we obtained experimentally, adding credibility to our assignment of the PTE as the dominant photoresponse mechanism and to the validity of our analytical model. We ascribe the lower experimental value (by a factor $\sim$3) to non-optimal performance of the actual antenna in the photodetector device, most likely due to the presence of metallic regions around the antenna (see Fig. 3.1). Furthermore, the simulations consider the absorption in the entire graphene sheet, rather than only in the photoactive area of the graphene channel. Notably, we point out that without the antenna, the amount of incident THz light from a diffraction-limited spot that would be absorbed in the photoactive area of the graphene channel would be more than three orders of magnitude lower, highlighting the importance of the antenna-integration. We illustrate this in Fig. 3.9b, where we show the antenna-induced absorption enhancement, defined as $G = \frac{P_{\mathbf{abs,sim,w/\ antenna}}}{P_{\mathbf{abs,sim,w/o\ antenna}}}$. These simulations show that the antenna enhances the graphene absorption by more than three orders of magnitude.

3.8 Thermoelectric simulations

We also assess the validity of the analytical model of Eqs. 3.1-3.2, by comparing the results with numerical simulations of the PTE photocurrent generated in different graphene geometries (see Fig. 3.13). In the following we introduce the thermoeletric modeling of the device that was developed by the group member Mark Lundeberg[89]. In order to calculate the PTE response of our device we solved numerically the linearized thermoelectric equations[90]:

$$j_Q(r) = -\sigma(r)\nabla V(r) - \sigma(r)S(r)\nabla T(r), \tag{3.3}$$
$$j_E(r) = -\Pi(r)\sigma(r)\nabla V(r) - [\kappa(r) + \Pi(r)\sigma(r)S(r)]\nabla T(r), \tag{3.4}$$

where $j_Q(r)$, $j_E(r)$ are the electric and energy current density respectively, $V(r)$ is the voltage, $T(r)$ is the local temperature, $\sigma(r)$ is the electrical conductivity, $S(r)$ is the Seebeck coefficient, $\Pi(r)$ is the Peltier coefficient, and $\kappa(r)$ is thermal conductivity. These two equations are coupled to the continuity equations for the charge and energy currents:

$$\nabla \cdot j_Q(r) = 0, \tag{3.5}$$
$$\nabla \cdot j_E(r) = -g(r)[T(r) - T_0] + J_E(r). \tag{3.6}$$

Here $g(r)$ parametrizes the thermal conduction to the substrate[45], T_0 is the substrate temperature, and $J_E(r)$ is a local heat source, that in our case is due to light absorption. We solved these equations inside a 2D simulation box $[0, L_{\mathbf{tot}}] \times [0, W_{\mathbf{tot}}]$ illustrated in Fig. S5 that includes the graphene sheet and the gold contacts. We artificially included a small rectangular region of dimension $\delta \times W$ between the graphene and the gold contacts to account for finite contact resistance by choosing the value of its conductivity $\sigma = \delta / R_{\mathbf{cont}}$ with $R_{\mathbf{cont}}$ being the value of the gold-graphene contact resistance. We assumed that the material parameters $\sigma(r)$, $S(r)$, $\Pi(r)$, $\kappa(r)$, and $g(r)$ are piecewise constant in the regions described in Fig. 3.13. Since, because of Onsager relations, $\Pi(r) = T_0 S(r)$, and the thermal conductivity is related to the electrical conductivity by the Wiedemann-Franz law $\kappa(r) = \mathcal{L}_0 \sigma(r) T_0$, with $\mathcal{L}_0 \equiv \pi^2 k_{\mathbf{B}}^2/(3e^2) = 2.44 \cdot 10^{-8} \mathbf{W\Omega K}^{-2}$, we have only three independent parameters $(\sigma(r), S(r), g(r))$ that are listed in Table 3.1.

Eqs. (3.3,3.4,3.5,3.6) need to be supplemented with boundary conditions (BCs). We used Dirichlet BCs at $x = 0, L_{\mathbf{tot}}$. These read:

$$V(x = 0, y) = V_{\mathbf{sd}}, \tag{3.7}$$
$$V(x = L_{\mathbf{tot}}, y) = 0, \tag{3.8}$$
$$T(x = 0, y) = T(x = L_{\mathbf{tot}}, y) = T_0. \tag{3.9}$$

We assumed instead homogeneous Neumann condition on the remaining part of the boundary

$$\hat{n} \cdot j_Q(r) = 0, \tag{3.10}$$
$$\hat{n} \cdot j_E(r) = 0, \tag{3.11}$$

$\hat{n}$ being the outward normal unit vector. We solved numerically Eqs. (3.3,3.4,3.5,3.6), with BCs (3.7,3.11) using the Finite Volume Method (FVM) on a regular square grid of 400×240 cells. Once the solution is found, the current flowing in the device can be calculated as

$$I \equiv \int_0^{W_{\mathbf{tot}}} J_x(0,y)dy = \int_0^{W_{\mathbf{tot}}} J_x(L_{\mathbf{tot}},y)dy = \frac{V_{\mathbf{sd}}}{R} + I_{\mathbf{PTE}}, \tag{3.12}$$

where the last equality holds because of linearity, R is the resistance, and

$$I_{\mathbf{PTE}} = \int dr \mathbb{R}_{\mathbf{int}}(r) J_E(r). \tag{3.13}$$

To find R we simply calculate the current by setting $J_{\mathbf{E}}(r) = 0$. The responsivity $\mathbb{R}_{\mathbf{int}}(r_0)$ at a given position r_0 is instead calculated by setting $V_{\mathbf{sd}} = 0$ and $J_{\mathbf{E}} = \delta(r - r_0)$, and calculating the corresponding current. This step is repeated for every r_0 in the simulation grid to obtain the responsivity maps in Fig. 3.13.

Material	$\sigma[S]$	$S[\mu V/K]$	$\Gamma_{cool}[W/m^2K]$
Graphene n (p) doped	$1.3{\cdot}10^{-3}$ [a]	80 (-80) [26]	$7{\cdot}10^4$ [45]
Gold	4 [b]	0 [c]	$300{\cdot}10^4$ [91,92]
Interface contact	$2.5{\cdot}10^{-6}$ [d]	0 [c]	$100{\cdot}10^4$

[a] When considering E_F = 50 (-50) meV, T = 300 K and 200 fs relaxation time for both doping type n (p). [b] For 100 nm gold. [c] We neglect the contribution of the Seebeck coefficient of the metal. [d] For a δ = 25 nm.

Table 3.1: Material parameters

We find agreement between the analytical and numerical results as depicted in Fig. 3.13, showing the validity of our analytical approach. Importantly, the analytical model gives us insights into the physics that determines the detector response, thus allowing for optimization strategies. The advantage of the numerical simulations is that they are also valid for non-rectangular graphene shapes. Our detector design is the result of these analytical and numerical simulations.

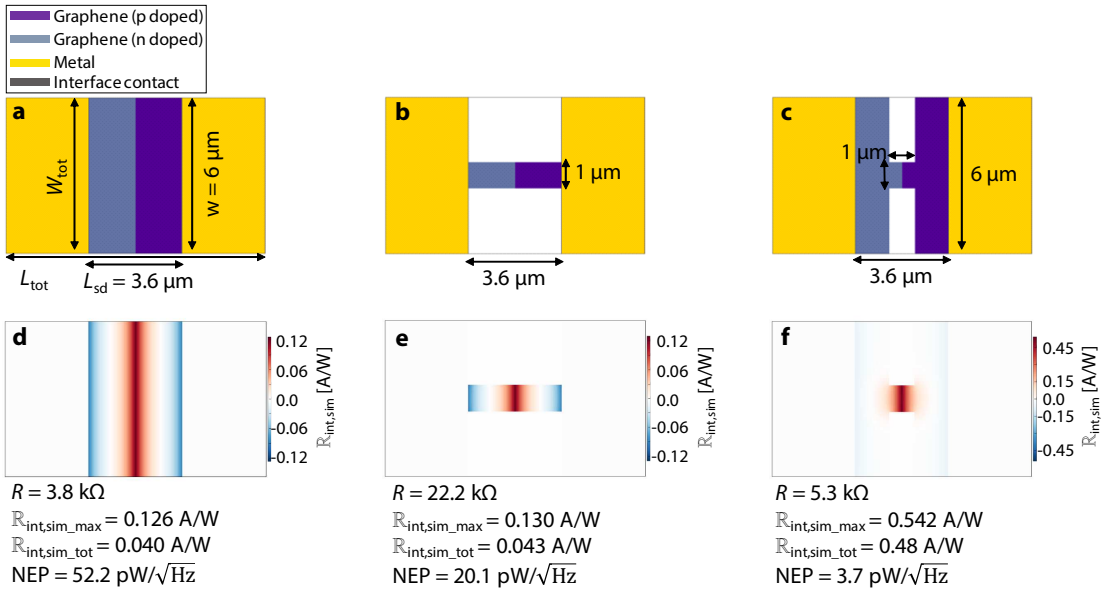

Fig. 3.13: Thermoelectric simulations results[89], as in Fig. 1c, which represent the resulting photoresponse after local photoexcitation, expressed in photocurrent normalized by absorbed power, *i.e.* internal responsivity ($\mathbb{R}_{int,sim}$ as defined in Eq. S11, where $J_E(r)$ represents the locally absorbed power). These simulations were based on similar characteristics of the measured samples, with a graphene scattering time of 200 fs (mobility 20,000 cm^2/Vs), contact resistance of 10 $k\Omega \cdot \mu m$, 3.6 μm of source-drain distance (L_{sd}), $\Gamma_{cool} = 7{\cdot}10^4$ W/m^2K, $E_F = 50$ meV and -50 meV for *n*- and *p*-doped graphene regions respectively. Panels **a-c)** show the simulated device geometries and panels **d-f)** the internal responsivity ($\mathbb{R}_{int,sim}$) calculated at each position across the device. The R, $\mathbb{R}_{int,sim\_max}$, $\mathbb{R}_{int,sim\_tot}$ and NEP below panels **d-f)** indicate total device resistance (including graphene sheet and contact resistance), the maximum internal responsivity generated at the *pn*−junction, total internal responsivity (which takes into account also the opposite sign responsivity generated at the metal-graphene interface, i.e. $\mathbb{R}_{int,sim\_tot} = \mathbb{R}_{int,sim\_max} - |\,\mathbb{R}_{int,sim\_min}\,|$) and noise-equivalent power, respectively. The simulations show that decreasing the width of the graphene channel (going from the design of panel **a** to the design of panel **b**) does not lead to any change in responsivity, but a decrease in noise-equivalent power. The responsivity is constant because of the trade-off between the increased ΔT due to the smaller active area and the increased device resistance due to the smaller width. The NEP is reduced, because the higher device resistance leads to reduced thermal noise. Then, by using the design with an "H-shaped" graphene channel in panel **c**, we both increase responsivity and decrease NEP. The main reason is that the active area is significantly reduced, without increasing too much the device resistance. Furthermore, the maximum responsivity and total internal responsivity are now very similar, because the PTE response at the *pn*-junction dominates. Therefore, this is the preferred design. We compare the simulation results for the internal responsivity $\mathbb{R}_{int,sim}$ with the analytically obtained values ($\mathbb{R}_{int,analyt}$) using the equations in the main text and the device resistances obtained from these simulations, and obtain $\mathbb{R}_{int,analyt} = 0.12$, 0.13 and 0.55 A/W for the designs from panels **a)**, **b)** and **c)** respectively. These analytical values are in excellent agreement with the $\mathbb{R}_{int,sim\_max}$ values obtained from simulations.

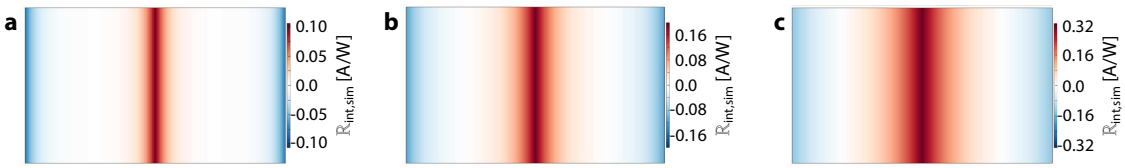

Fig. 3.14: Thermoelectric simulations[89], showing the internal responsivity ($\mathbb{R}_{\mathbf{int,sim}}$ as defined in Eq. 3.13, where $J_E(r)$ represents the locally absorbed power) for a fixed device geometry and three different values of the interfacial heat conductivity $\Gamma_{\mathbf{cool}}$. For all these three cases the device length and width dimensions are 10 and 6 μm respectively, E_F = 50 meV (-50 meV) for *n*- (*p*-) doped region and with a contact resistance of 10 k$\Omega \cdot \mu$m. The $\Gamma_{\mathbf{cool}}$ is $7{\cdot}10^4$, $2{\cdot}10^4$ and $0.7{\cdot}10^4$ W/m^{2}K for **a)**, **b)** and **c)** respectively. As predicted from Eq. 3.2, when decreasing $\Gamma_{\mathbf{cool}}$, ΔT increases and therefore $\mathbb{R}_{\mathbf{int,analyt}}$. In fact, by calculating the $\mathbb{R}_{\mathbf{int,analyt}} = I_{\mathbf{PTE}}/P_{\mathbf{abs}} = \frac{\Delta S \Delta T}{P_{\mathbf{abs}} R} = \frac{\Delta S}{A_{\mathbf{active}} \Gamma_{\mathbf{cool}} R}$, we obtain excellent agreement between these calculations and the thermoelectric simulations values of $\mathbb{R}_{\mathbf{int,sim}}$ for all three cases, namely $\mathbb{R}_{\mathbf{int,analyt}}$ = 0.10, 0.19 and 0.33 A/W for **a)**, **b)** and **c)** respectively. These results show that the responsivity increases (and the NEP decreases) with the square-root of the decrease in interfacial heat conductivity.

3.9 Device benchmark

Finally, we compare the performance of our photodetector with respect to other graphene-based THz photodetectors in the literature. We first compare with other detectors where the photodetection mechanism was explicitly ascribed to the PTE effect (see Table 3.2). Since not every report used the same power normalization procedure for the responsivity and NEP, we mention explicitly the normalization procedure that was used. We note that our THz detector is 2–4 orders of magnitude more sensitive than any other THz PTE photodetector (if the same normalization procedure would be applied). We attribute this to our novel design with the antenna/gating structure, the optimal graphene channel geometry and the use of high-mobility hBN-encapsulated graphene. Furthermore, the sensitivity that we obtain is very similar to, or better than, the most sensitive graphene-based THz detectors reported in the literature[80,82]. The operation of those detectors, however, has only been shown for frequencies below 1 THz and no response times have been measured. Additionally, it's important to point out that the Drude optical conductivity and therefore absorption in graphene is higher in the GHz range than in THz[93,94], hence a direct comparison with detectors operating below 1 THz is not straightforward since we do not normalize the detector responsivity by the graphene absorption. We point out that a recent work from our collaborators[95] incorporates our design and reproduces our results successfully by reporting a similar NEP value as shown at the last row of Table 3.2. However, they are able to modulate at higher speed the QCL pulses and have a faster model of current amplifier (operating up to ∼1 GHz), hence they are able to measure faster rise and fall times below 1 ns that are setup-limited by the QCL modulation.[95]

Reference	Mechanism	NEP ($pW/\sqrt{Hz}$)	Normalization area A_{norm}[a]	Speed (ns)	Freq. range (THz)
This work	PTE	80	λ^2/π	<30	1.8 – 4.25
[42]	PTE	1100	$\sim \lambda^2/3350$	0.11	2.5
[84]	PTE	350	$\sim \lambda^2/450$	9000	0.08 – 0.3
[80]	Plasma waves	130	none	-	0.4
[67]	Plasma waves	2000	$\lambda^2/4$	-	0.29 – 0.38
[81]	PTE/plasma waves	600	none[b]	-	0.13 – 0.45
[82]	Ballistic rectification	34	$\lambda^2/4\pi$	-	0.07-0.69
[95]	PTE	120	$\lambda^2/4$	<0.9	3.4

[a] The normalization area A_{norm} refers to the area to which the incident power was normalized: $P_{norm} = P_{in} \cdot A_{norm}/A_{focus}$. In our work, for example, we use the power in a diffraction-limited spot $P_{diff} = P_{in} \cdot A_{diff}/A_{focus}$, *i.e.* we use $A_{norm} = A_{diff} = \lambda^2/\pi$.
[b] Whereas the incident power was not normalized to any area, a correction of the incident power was applied to account for losses occurring in the focusing system.

Table 3.2: Comparison of graphene-based THz photodetectors

3.10 Conclusions and outlook

In conclusion, we have demonstrated a novel THz photodetector, which is dominated by the photo-thermoelectric effect. It operates at room temperature, is highly sensitive and very fast, has a wide dynamic range and operates over a broad range of THz frequencies. We have optimized the PTE THz detector by using a split-gate/antenna structure with narrow gap, which funnels the incident THz light exactly at the small photoactive area of the detector leading to strongly enhanced THz absorption in graphene. This structure simultaneously allows for tuning the detector to the optimal gating configuration, where a *pn*-junction is created in the graphene channel. Furthermore, we have used an "H-shaped", high-quality, hBN-encapsulated graphene channel with a narrow width, in order to have a small photo-active area, thus achieving a large THz-induced change in temperature, and a low overall device resistance.

Given the qualitative and quantitative understanding we have developed of the performance of our detector, we identify strategies for further improving its performance. Most importantly, by optimizing the antenna, a higher absorption and therefore lower NEP can be achieved. Additionally, by using a more broadband antenna, the detector will be sensitive for a larger range of THz frequencies. The sensitivity can be further enhanced by having a lower thermal conductivity $\Gamma_{\mathbf{cool}}$ (see Fig. 3.14). This could be achieved by exploring alternative encapsulation materials, rather than hBN, *e.g.* a transition metal dichalcogenide (TMD) material, and by operating at a lower temperature. We estimate that it will be possible to reach an NEP in the low pW/$\sqrt{\mathbf{Hz}}$-regime. We expect that the unique combination of high sensitivity and fast operation means that these THz PTE detectors will play an important role in a large spectrum of applications.

4 Plasmonic antenna coupling to hyperbolic polaritons for mid-infrared photodetection with graphene

4.1 Introduction

Hyperbolic phonon-polaritons (HPPs) are hybridized modes of ionic oscillations and light present in polar dielectric materials, such as hexagonal-BN (hBN)[14–16,33,35,55,96] that show interesting optical properties such as extreme subwavelength ray-like propagation and sub-diffraction light confinement ($\sim \lambda_0/100$)[4,35,97–99], among others. In fact, novel nano-optoelectronic platforms can be attained by merging HPPs functionalities with other 2D materials-based devices, such as graphene photodetectors governed by the photothermoelectric (PTE) effect. This mechanism generates a photoresponse in graphene *pn*-junctions[19,43,44,83,100–103] driven by a temperature gradient and Fermi level asymmetry across the channel. Nevertheless, one of the limitations of these detectors is the low light absorption of graphene, especially for mid-IR frequencies where the photon energy becomes comparable to the typical doping level of graphene reaching the Pauli blocking regime[20,21]. This is further exacerbated by the small photoactive area of graphene *pn*-junctions[45,100], limited by the cooling length of the hot carriers (0.5-1 µm)[23,43–45]. These limitations can be overcome by exciting HPPs and focusing them towards the photoactive area and consequently absorbing them in graphene. However, efficient exploitation of HPPs for mid-IR photodetection still remains unexplored.[64,104] In this work, we embed hBN and graphene within metallic antennas in order to couple their plasmonic interactions with HPPs and achieve highly concentrated mid-IR light on a graphene *pn*-junction for sensitive and fast mid-IR photodetection.

4.2 Device fabrication

First, we fabricate the H-shaped local gates structure with a total length of 4.2 µm, a total width of 2 µm and a narrow width region (tip) of 500 nm on a Si/SiO_2 substrate using electron beam lithography (EBL) followed by evaporation of titanium (2 nm) / gold (30 nm). The gap between the gates is 155 nm. Afterwards, we transfer a hBN/graphene/hBN stack onto the metallic gates. We cleave and exfoliate the top and bottom hBN and the graphene onto freshly cleaned Si/SiO_2 substrates, stack them following the Van der Waals assembly technique[34,56] and release onto the gates. We then use electron beam lithography with a PMMA 950 K resist film to pattern source and drain electrodes and expose the device to a plasma of CHF_3/O_2 gases to partially etch the Van der Waals stack. Subsequently, we deposit side contacts of chromium (5 nm) / gold (80 nm) and lift off in acetone as described in Ref. 34. We then etch the hBN-encapsulated graphene into an H-shape using a CHF_3/O_2 plasma and deposit 17 nm of Al_2O_3 using atomic layer deposition (ALD). Finally we pattern the bow-tie antenna of 2.7 µm total length (L) and with a small gap of 200 nm between its branches with EBL and deposit titanium (2 nm) / gold (80 nm). An optical image of the device is depicted in Fig. 4.3c. We point out that the bow-tie antenna and gate dimensions were selected based on preliminary optical simulations based on a simplified device, ignoring bow-tie antenna interactions with gates and metal electrodes, resulting in the non-optimal performance as evident from Fig. 4.13. By performing 2-terminal configuration electrical measurements as a function of the gate voltages (varying $V_{\mathbf{L}}$ and $V_{\mathbf{R}}$ both at the same potential), we attain 12,000 $cm^2V^{-1}s^{-1}$ as a lower bound of the estimated mobility (see Figs. 4.1-4.2 and section 4.6.4).

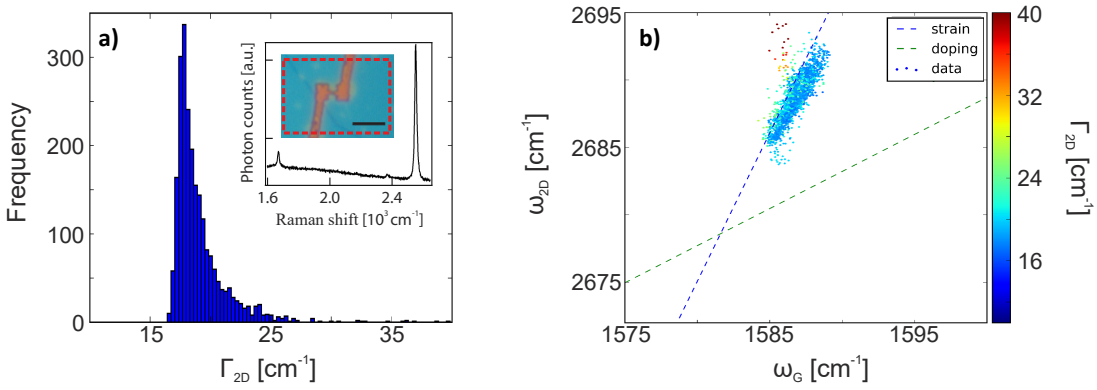

Fig. 4.1: Raman spectroscopy measurements of the 2D stack on top of the metal gates. **a)** Histogram plot of the full-width-half-maximum of the graphene 2D peak (Γ_{2D}) across a region of ∼13.5×9 μm^2 as shown in the inset in red dashed line. The inset scale bar corresponds to 4.2 μm. The mean Γ_{2D} is ∼ 18 cm^{-1}, which reflects the high quality of the monolayer graphene encapsulated in hBN. The inset plot corresponds to the usual spectrum obtained in these measurements for single layer graphene. **b)** 2D frequency peak (ω_{2D}) as a function of G frequency peak (ω_G) obtained from the Raman map in panel **a**, where the colorbar corresponds to the Γ_{2D} of the measured map. We obtained low doping values consistent with transport measurements (see Fig. 4.2) and modest strain values[86].

4.3 Experimental mid-IR setup

We use a pulsed QCL mid-IR laser (LaserScope from Block Engineering) that is linearly polarized and has a wavelength tuning range from $\lambda = 6.1$ to 10 μm. We scan the device position with motorized xyz-stage. We modulate the mid-IR laser employing an optical chopper at 422 Hz and we measure the photocurrent using a lock-in amplifier (Stanford Research). We focus the mid-IR light with a reflective objective with a numerical aperture (NA) of 0.5. We measure the mid-IR power using a thermopile detector from Thorlabs placed at the sample position.
For the time-resolved measurements, we set the QCL wavelength to $\lambda = 6.6$ μm with a pulse width of 496 ns. We use a MCT as a reference detector from VIGO System model PCI-2TE-13. We measure the photoresponse using a current amplifier from FEMTO model DHPCA-100 with switchable gain and acquire the signal with an oscilloscope from Teledyne Lecroy model HDO6000.

4.4 Device working principle

Our design (depicted in Fig. 4.3a-c) combines several mechanisms to achieve high field concentration for both incident light polarizations. Specifically, when the incident mid-IR light is polarized parallel to the bow-tie antenna main axis (Transverse Magnetic, TM-polarization, Fig. 4.3d), it excites its localized surface plasmon resonance (LSPR) spectrally located at $\lambda \approx$ 5-7 μm (see Fig. 4.4). As a result, the antenna concentrates the incoming mid-IR light into its gap that is situated just above the graphene *pn*-junction (i.e.

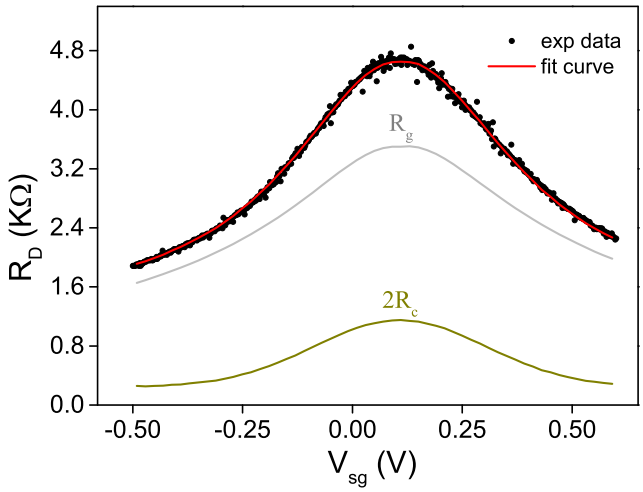

Fig. 4.2: Measured device resistance (R_D) as a function of the two gate voltages (V_L and V_R) both sweeping at the same voltage (V_{sg}). We fit the resistance curve using the model described in section 4.6.4. Contributions of both contact resistance ($2R_c$) and graphene channel resistance (R_g) to R_D for all V_{sg} are also presented.

the detector photoactive area[100]). At the same time, the near-fields produced within the antenna hot-spot contain high momenta and thus efficiently launch HPPs ascribed to the spectral overlap of the antenna's LSPR with the hBN upper reststrahlen band (RB) range ($\lambda \approx$ 6-7 μm). These HPPs propagate as guided modes and interfere within the graphene *pn*-junction, producing high absorption across this small localized region. Likewise, when the incident mid-IR light is polarized perpendicularly to the bow-tie antenna main axis (Transverse Electric, TE-polarization, Fig. 4.3e), it produces strong light concentration in the gap of the H-shaped antenna, acting as the split-gate, ascribed again to its LSPR spectrally located at $\lambda \approx$ 5.5-7.5 μm (see Fig. 4.5). This phenomenon will also launch hBN HPPs at the gate edges, which will be guided and interfered within the photoactive area.

The absorption process in the graphene is mediated mostly by interband transitions, which mainly occur in the regions within the gap of the gates where the graphene doping is sufficiently small to avoid Pauli blocking (see Figs. 4.20-4.21). The excited carriers quickly relax (<100 fs)[23] into a local hot equilibrium Fermi-Dirac distribution by electron-electron scattering. Subsequent cooling mechanisms include electron-phonon scattering (∼1 ps)[23,43–45,88] and heat diffusion away from the junction area. As a result, a symmetric electronic temperature profile $T_e(x)$ is produced in the graphene junction[43,44,64], giving rise to a thermoelectric voltage $V_{PTE} \propto S(x)\nabla T_e(x)$, where x runs along the graphene channel and $S(x)$ represents the Seebeck coefficient which is tunable by the gates. Since $\nabla T_e(x)$ is antisymmetric, an antisymmetric $S(x)$ is also needed to maximize the net PTE response, which is achieved by applying opposite voltages to the two gates (see Figs. 4.20-4.21). In addition to HPPs promoting absorption in graphene, they also absorb light themselves. However, due to the large ($\sim 10^3$) heat capacitance mismatch between graphene electrons and lattice, the HPP absorption does not amount to any meaningful temperature rise and

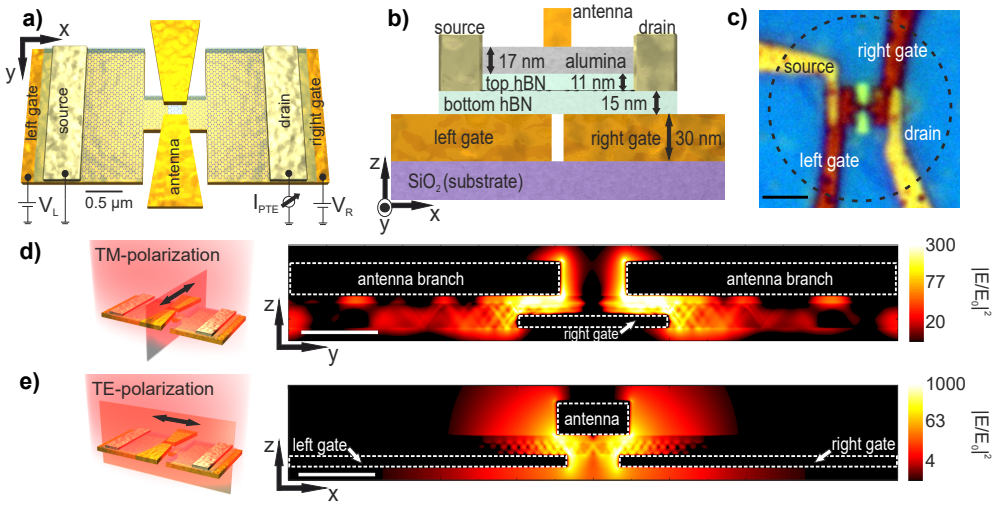

Fig. 4.3: Device schematic and operation principle. **a)** Schematic representation of the photodetector consisting of H-shaped resonant gates of 4.2 μm of total length, with a hBN encapsulated H-shaped graphene channel transferred on top, contacted by source and drain electrodes. A bow-tie antenna of 2.7 μm of total length is placed on top of the 2D stack. The local gates serve to create a *pn*-junction in the central part of the graphene channel (by applying voltages V_L and V_R), where the antenna gap and gate gap are located. Both narrow gaps are on the order of ∼100 nm. The scale bar corresponds to 0.5 μm. **b)** Side view of the device design (not to scale) with indications of the materials' thicknesses. **c)** Optical image of the photodetector. The dashed lined circle indicates the typical beam spot size obtained at $\lambda = 6.6$ μm. The scale bar corresponds to 2.5 μm. **d)** Cross section view of the simulated total electric field intensity ($|E|^2$) normalized to the incident one ($|E_0|^2$) along the antenna main axis when light is polarized parallel to the bow-tie antenna (TM-polarization) axis as indicated in the illustration on the left. The white scale bar corresponds to 250 nm. **e)** Same as **d** but for light polarization perpendicular to the bow-tie antenna (TE-polarization) and parallel to the local gates as shown in the schematic on the left.

thus does not contribute to the device PTE response.

4.5 Results

4.5.1 Photocurrent measurements and spectral response.

To reveal the spatial intensity profile of the beam focus at $\lambda = 6.6$ μm, we scan the sample with *xyz*-motorized stages and measure the photocurrent (I_{PTE}) as shown in Fig. 4.6a. As a result, we observe the Airy pattern of the beam, which implies that we obtain a well-focused beam and high sensitivity at this wavelength considering the small irradiance input of 0.2 μW/μm^2. Next, we investigate the photoresponse as a function of the two gate voltages (V_L and V_R), shown in Fig. 4.6b, which reveals the photocurrent mechanism and optimal doping level. We find that when sweeping the gate voltages independently, the photocurrent follows several sign changes resulting in a 6-fold pattern, which indicates that the photodetection is driven by the PTE effect, as also shown in other studies in the mid-IR range[64,105,106]. The highest values of photocurrent occur at *pn* or *np* configuration, specifically at $V_L = 1.6$ V (170 meV) and $V_R = -0.82$ V (-130 meV), which are relatively

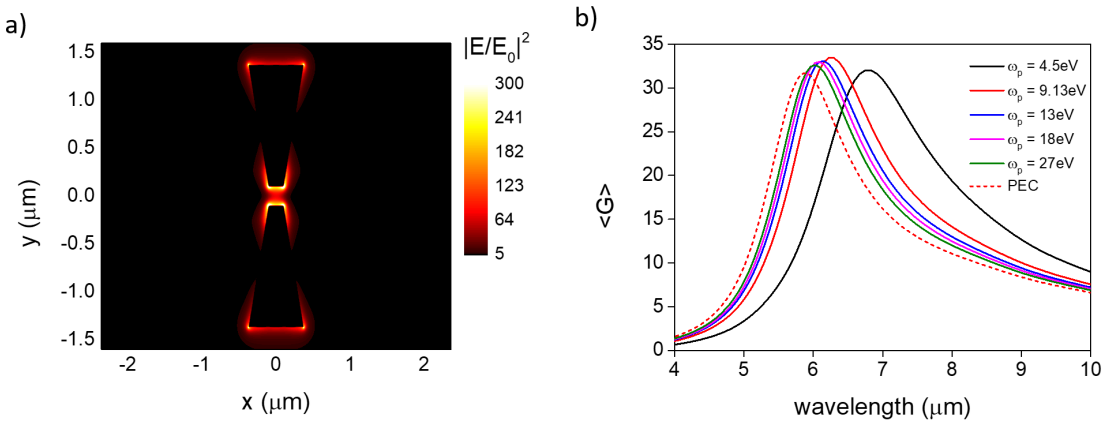

Fig. 4.4: a) Simulated electric field intensity enhancement for the incident mid-IR light polarized parallel to the bow-tie antenna main axis (TM-polarization) at $\lambda = 5.5$ μm for the full experimental structure described in section 4.2. The antenna exhibits a dipole field distribution with high field confinement in the antenna gap and small field penetration inside the metal. **b)** Average absorption enhancement $< G >$ (G is defined as $G(\lambda, \mathbf{r}) = \mathbf{Abs_{device}}(\lambda, \mathbf{r})/\mathbf{Abs_{air}}(\lambda, \mathbf{r})$, which is the ratio between the graphene absorption incorporating all the elements of the device (e.g. antenna, contacts, etc.) to that of suspended graphene as a function of λ and the position vector $\mathbf{r}$.) within a 0.2×0.2 μm^2 area at the device center ($x = y = 0$, see also Fig. 4.3a-b for axis definition). For simplicity, we use wavelength-independent refractive indices for the other materials $n_{\mathbf{hBN}} = 2.4$, $n_{\mathbf{SiO_2}} = 1.5$ and $n_{\mathbf{Al_2O_3}} = 1.6$. Different antenna metals are considered in the Drude model by assuming different plasma frequencies (9.13 eV for Au). We observe that the response changes in both amplitude and spectral position for different plasma frequencies and is different from the PEC case (to which they eventually converge for increasing plasma frequency). We conclude that while the Au plasmons do not directly influence the device physics, they do modulate the antenna response and are thus needed for an accurate quantitative description of the metal antenna response.

low doping levels. We note that when applying a voltage bias in the graphene channel, the photocurrent remains constant while the source-drain current increases linearly with bias (see Fig. 4.7). This allows us to discard other mechanisms such as photogating and bolometric effects that would increase significantly with voltage bias.

To determine the photodetector spectral response, we measure the TM-polarization (Fig. 4.6c) external responsivity (see section 2.3.4) as a function of excitation wavelength. We obtain high values up to 15 mA/W within 6-7 μm at the hBN RB. On the other hand, for TE-polarization (Fig. 4.6d) we observe two responsivity peaks, the first one (up to 22 mA/W) again within the hBN RB (6-7 μm) and a second peak (3.5 mA/W) around 8 μm. We also plot the simulated responsivity that is extracted from the multiphysics simulations, which considers the exact geometry of the photodetector and the whole device photoresponse (optical excitation, carrier distribution and relaxation, heat diffusion and thermoelectric current collection. See further details in section 4.6). We observe very good qualitative and quantitative agreement between experimental and theoretical responsivity, which we explore in the following by analyzing each component involved in

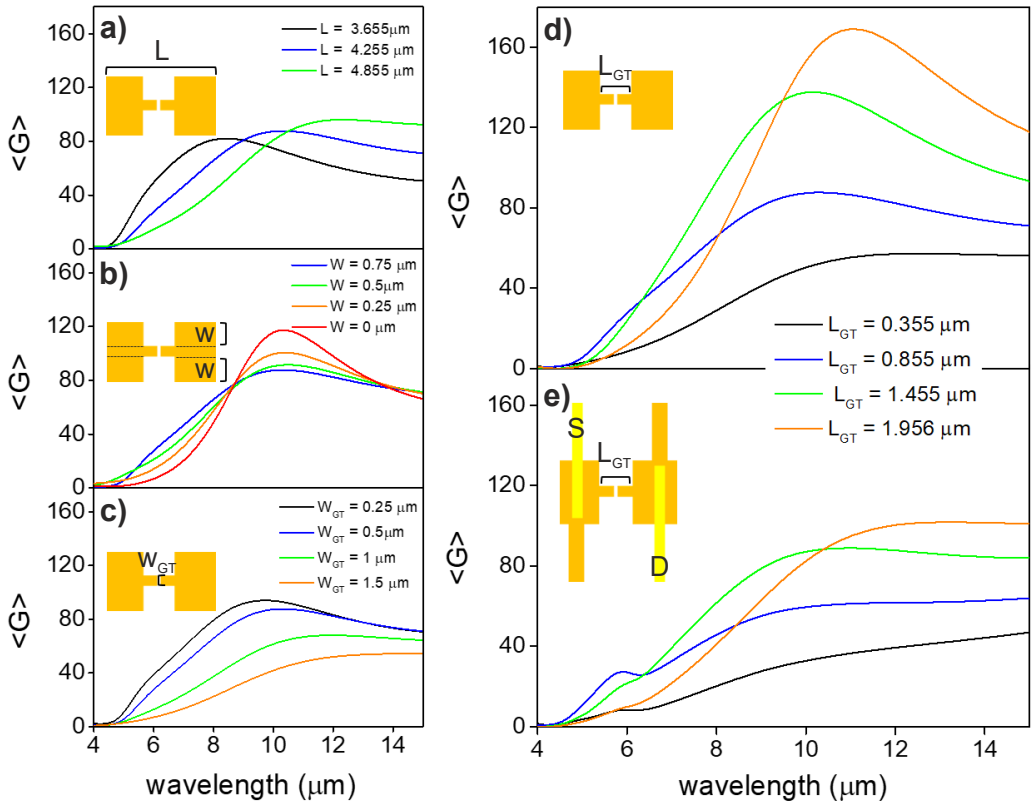

Fig. 4.5: Simulated $<G>$, which is G averaged over the 0.2×0.2 μm^2 rectangular space around the center of the device ($x = 0$, $y = 0$, see Figs. 4.3a-b and 4.4 for axis definition), for TE-polarization as a function of the geometrical parameters of the H-shaped gates and additional metal components for the spectral range from 4 to 15 μm. In all cases, we use wavelength-independent refractive indices for hBN ($n = 2.4$), SiO_2 ($n = 1.5$) and alumina ($n = 1.6$), hence we can clearly observe the plasmonic response of the local gates without additional resonances coming from the phonon-polaritons of hBN or SiO_2. In all cases the blue line corresponds to the response of the configuration where the varied parameter has the same value as the one it has in the experimental device. **a)** $<G>$ values for different total lengths (L) of the local gates. We observe resonant peaks for all cases which shift to longer wavelengths as we increase L, a typical trend of metallic plasmonic resonators. In **b)** the width (W) of both extended parts of the H-shaped local gates is reduced starting from 0.75 μm (blue line) down to 0 μm (red line) while keeping L fixed at 4.255 μm. We clearly observe that the resonance peak is not shifted spectrally and also as W is reduced the spectral response converges to that of a dipole antenna (red line), thus proving the plasmonic behavior of the local gate geometry. In **c)**, we vary the gate tip width (W_{GT}) and notice that when increasing it, its plasmonic resonance is redshifted, its $<G>$ amplitude drops down and the resonance becomes broader. In **d)** we vary the length of the gate tip (L_{GT}) while keeping L and W fixed at 4.255 μm and 0.75 μm respectively. We observe that the plasmonic response can be strongly tuned both spectrally and in amplitude when changing L_{GT}. Finally, in **e)** we add the extended electrodes to the local gates and also the source-drain contacts. We observe that these additional metal components further alter the response which is now lowered and broadened while we also notice an extra resonance peak at 5.8 μm. Note also that in the wavelength range of the hBN upper RB (6-7 μm) the optimum L_{GT} should be around 1.4 μm as shown in **d** and **e**. Due to the complexity of the H-shape configuration there are a large number of parameters that can strongly tune the plasmonic resonance of the local gates, meaning that we can further improve the device performance.

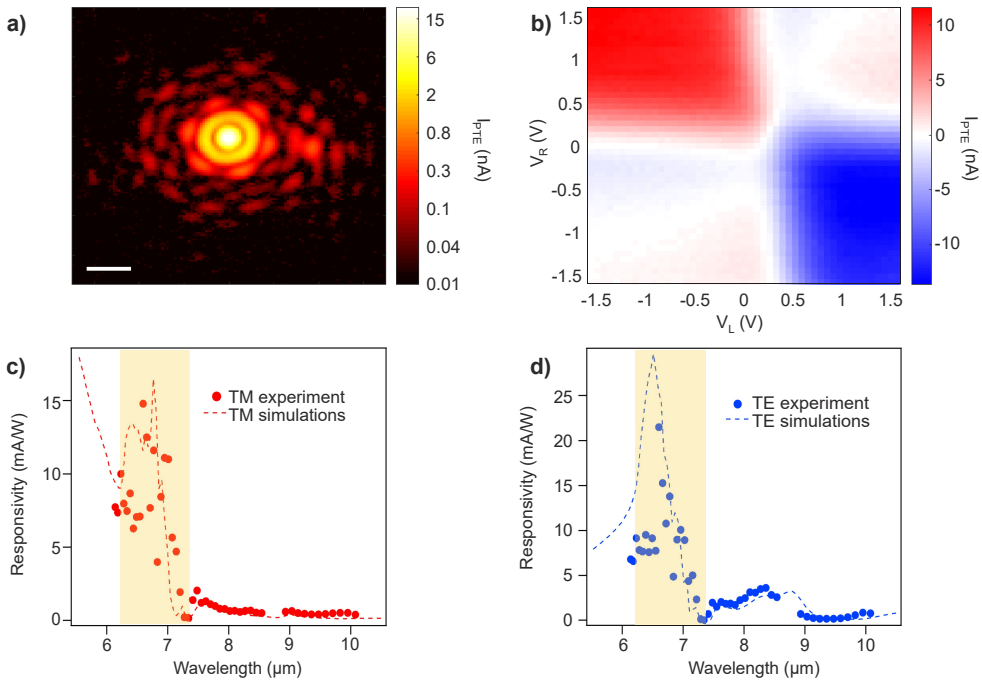

Fig. 4.6: Photocurrent generation and spectral photoresponse a) Scanning photocurrent map (log scale) across the mid-IR beam focus at $\lambda = 6.6$ μm. The white scale bar corresponds to 20 μm. We obtain a FWHM of 6.1 μm. We use a small input power ($P_{\mathbf{in}}$) of 13.7 μW (irradiance of 0.2 μW/μm^2). **b)** Photocurrent map as a function of the two gate voltages at $\lambda = 6.6$ μm. **c)** Experimental (dots) and theoretical (dashed lines) spectral external responsivity of the device for TM-polarization and **d)** for TE-polarization. The highlighted region corresponds to the hBN RB ($\lambda = 6.2$ - 7.3 μm). For **c** and **d**, we set the gate voltages to a *pn*-junction configuration close to the optimal with $V_{\mathbf{L}} = 0.5$ V (97 meV) and $V_{\mathbf{R}} = -0.5$ V (-100 meV). We use the same doping level for the theoretical simulations.

the photoresponse.

4.5.2 Spectral and spatial analysis of the photoresponse.

We first identify the behavior of the resonant mechanisms, in terms of field intensity enhancement and spatial localization by studying the absorption enhancement in graphene (G) across the channel in the x direction (averaging over 500 nm in y direction, see Fig. 4.3a-b for axis definition) and as a function of the wavelength as shown in Fig. 4.8. We define G as following: $G(\lambda, \mathbf{r}) = \mathbf{Abs_{device}}(\lambda, \mathbf{r})/\mathbf{Abs_{air}}(\lambda, \mathbf{r})$, which is the ratio between the graphene absorption incorporating all the elements of the device (e.g. antenna, contacts, etc.) to that of suspended graphene as a function of λ and the position vector $\mathbf{r}$. G and responsivity are proportionally related via the electronic temperature gradient as shown in Fig. 4.21 and section 4.6.2.

In the TM-polarization case shown in Fig. 4.8a, we observe very high G values at the antenna LSPR ($\lambda \sim 6$ μm). The value of G peaks around 6.8 μm due to the hybridization

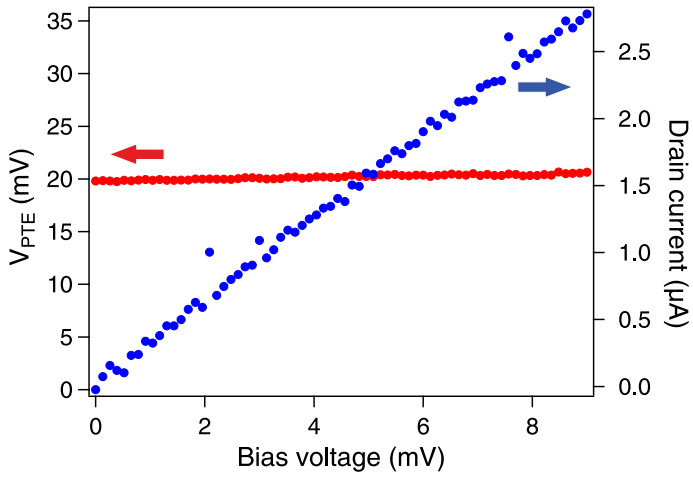

Fig. 4.7: Photovoltage (red) and source-drain current (blue) as a function of the graphene channel bias. We observe that the photocurrent remains constant, whereas the source-drain current increases linearly when increasing the bias voltage.

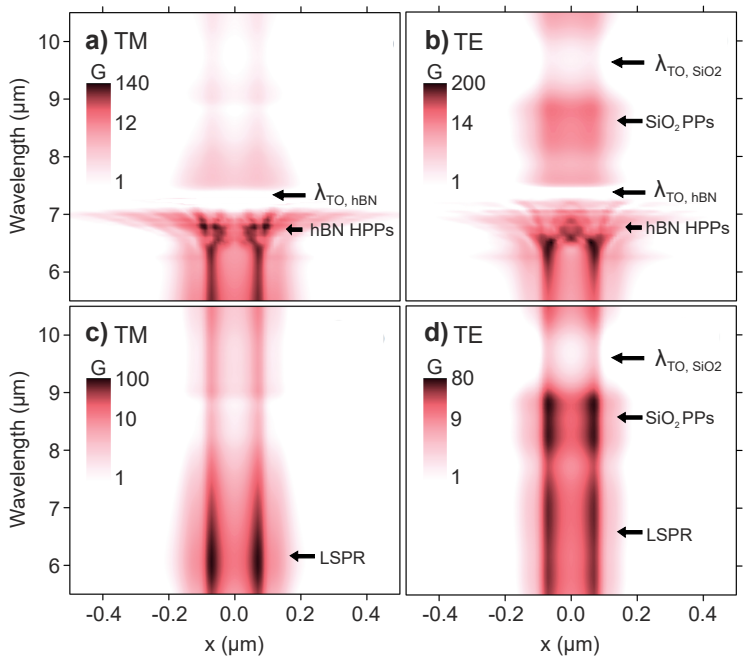

Fig. 4.8: Absorption enhancement spectra. Simulations of the absorption enhancement in graphene (G) along the source-drain direction (x direction as shown in Fig. 4.3a-b, where $x = 0$ is located at the center of the gate gap) as a function of the wavelength, for TM (**a**) and TE-polarization (**b**). **c)** and **d)** correspond to **a** and **b** respectively but with wavelength-independent refractive index for hBN ($n = 2.4$).

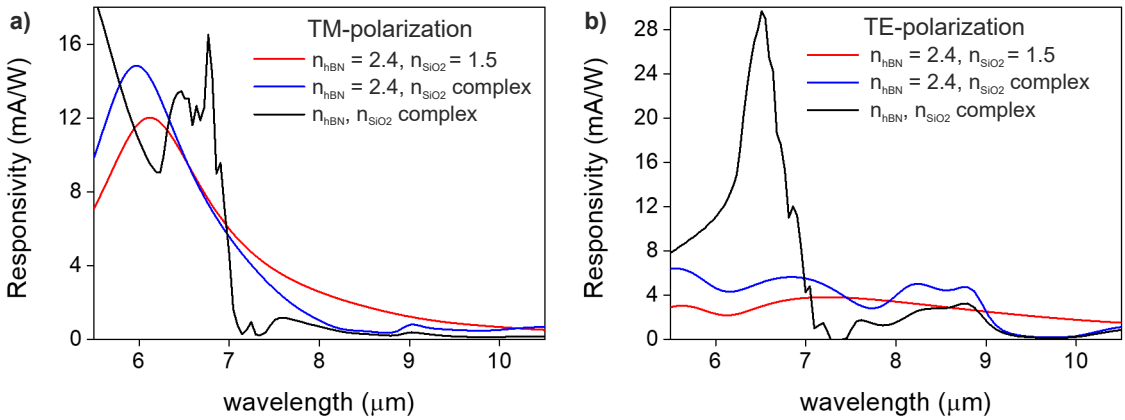

Fig. 4.9: Simulated spectral responsivities of **a)** TM and **b)** TE-polarization using different refractive indices configurations. Red solid line represents the case of wavelength-independent refractive indices for hBN ($n = 2.4$), SiO_2 ($n = 1.5$) and alumina ($n = 1.6$). For blue solid line we use the full dispersive optical model for the SiO_2 but not for the hBN, for which we use a wavelength independent refractive index of $n = 2.4$. Finally, for the black solid line we use full dispersive optical model for both SiO_2 and hBN.

of the hBN HPPs with the antenna LSPR and to the constructive interference of the propagating HPPs occurring at $x \sim +/-100$ nm. In fact, the different spatial patterns of G arise from the wavelength dependence of the HPP propagation angle in hBN following the equation $\tan\theta(\omega) = i\sqrt{\varepsilon_{x,y}(\omega)}/\sqrt{\varepsilon_z(\omega)}$ [35,64,107]. For longer wavelengths, we find a negligible G between 7-7.3 μm that corresponds to the hBN transverse optical (TO) phonon. We observe that the highest G values are only found for the spatially confined region (from $x \sim$ -100 to 100 nm) where the antenna and gates overlap, which is designed to coincide with the graphene *pn*-junction (see Figs. 4.10-4.11 and section 4.8. Nevertheless, in the hBN RB we find large G values outside this tightly localized region due to HPP propagation.

For TE-polarization (see Fig. 4.8b), we find the maximum values of G between 6.2 to 6.6 μm due to the gate LSPR hybridization with HPPs and their strong constructive interference at $x = 0$. For longer wavelengths, we identify a G peak centered at 8.5 μm that corresponds to SiO_2 phonon-polaritons (PPs) hybridization with the gate LSPR as presented in Figs. 4.9 and 4.12

To further elucidate the role of the antennas in G, we simulate the system without the contribution of the HPPs using wavelength-independent refractive index values for the hBN (Fig. 4.8c-d). For TM-polarization (Fig. 4.8c), we observe a peak around 6 μm that corresponds to the antenna LSPR and its resonance tail extending up to 8 μm. For TE-polarization, in contrast, Fig. 4.8d shows high values of G across a broader wavelength range (5.5-7.5 μm) due to the complex shape of the gates and their interactions with the source-drain contacts (see Fig. 4.5). Although in Fig. 4.8d we observe lower G values compared to Fig. 4.8c (see also Fig. 4.9), we obtain higher values of G in TE-polarization when combining the gate LSPR with HPPs (Fig. 4.8b) ascribed to its higher spectral overlap with the hBN RB and due to the stronger constructive interferences of the HPPs excited by the gates.

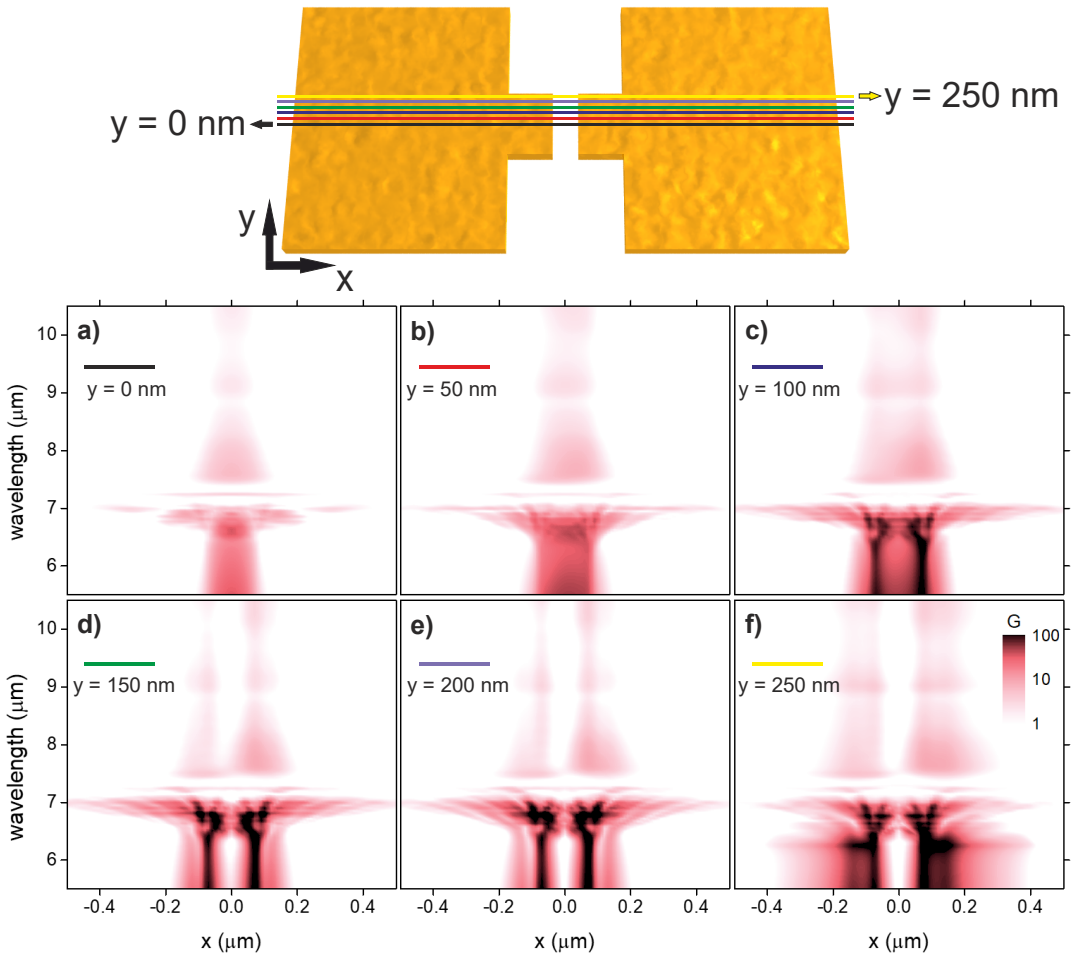

Fig. 4.10: G values for TM-polarization for different cross-sections across the gates along the source-drain direction (x direction, where x =0 is located at the center of the gate gap. This gap is 155 nm. See Fig. 4.3a-b for axis definition) as a function of wavelength. **a)** corresponds to a linecut of G across the center of the gates ($y = 0$) as indicated in the top schematic. Then, the rest indicate linecuts of G **b)** 50 nm, **c)** 100 nm, **d)** 150 nm, **e)** 200 nm and **f)** 250 nm above the center of the gates. The gates and antenna overlap at $y > 100$ nm (or $y <$ -100 nm) away from the center ($y = 0$ nm). The upper antenna branch tip is located at $y = 100$ nm. We observe that the spatial pattern of G varies with y and that G increases significantly where these two metal regions overlap ($y > 100$ nm).

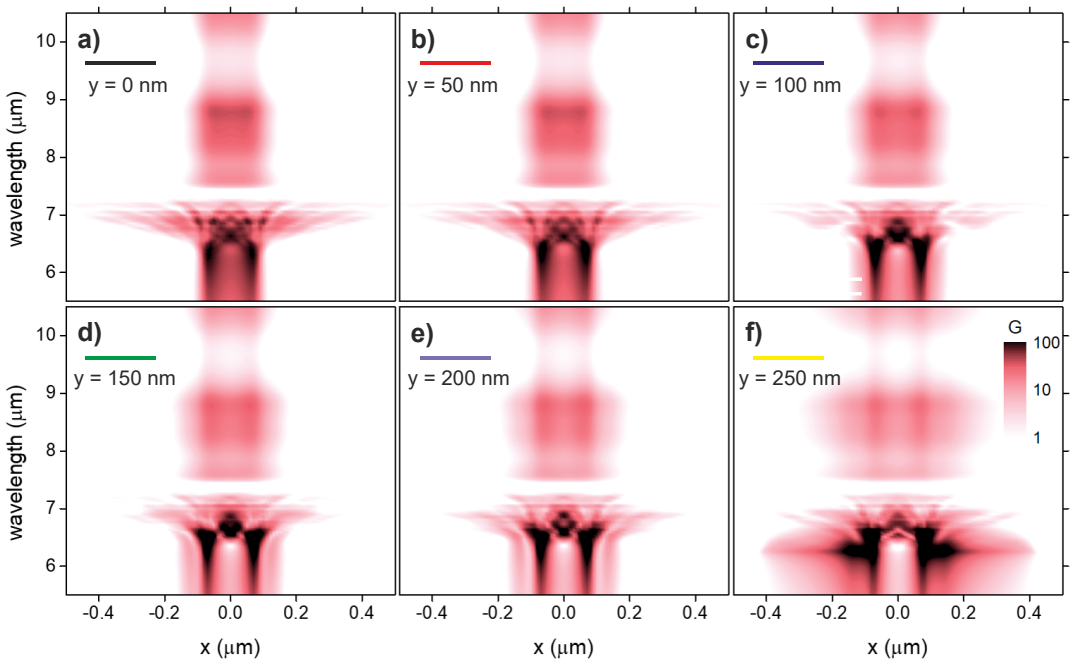

Fig. 4.11: Same as Fig. 4.10 but for TE-polarization. **a)** corresponds to a linecut of G across the center of the gates ($y = 0$). The rest indicate linecuts of G **b)** 50 nm, **c)** 100 nm, **d)** 150 nm, **e)** 200 nm and **f)** 250 nm above the the center of the gates. We observe that the spatial pattern of G varies while looking at it along different locations and that G greatly increases where the gate and antenna regions overlap ($y > 100$ nm).

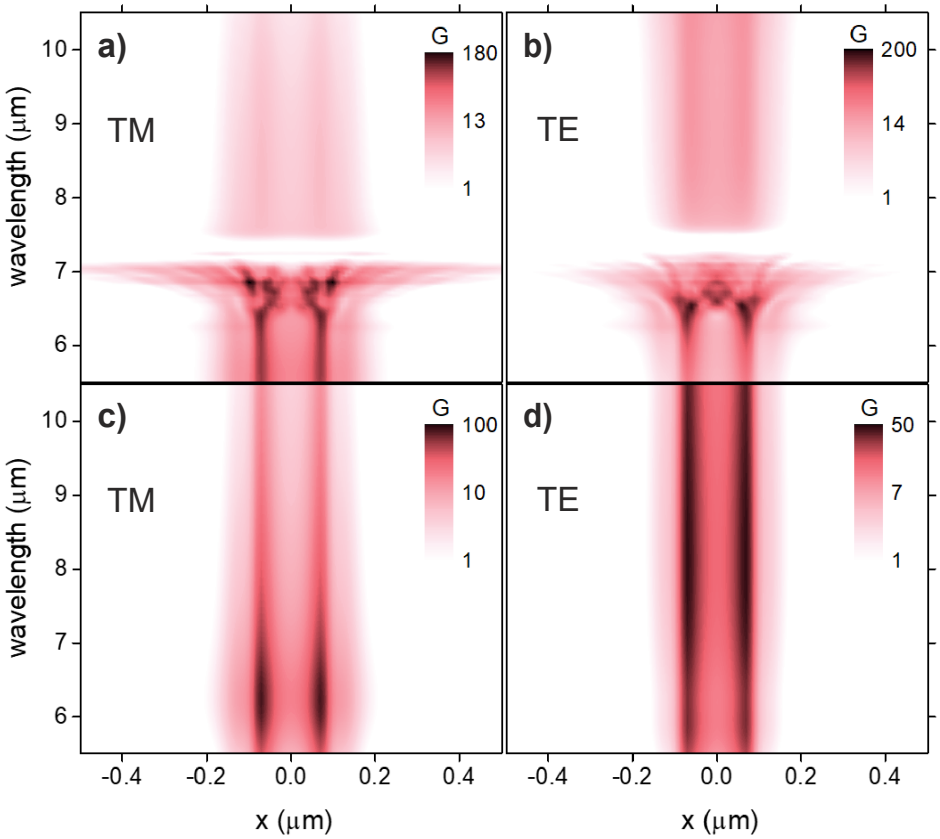

Fig. 4.12: Simulations of the absorption enhancement G along the source-drain direction (x direction and averaging over 500 nm in y direction, where $x = 0$ is located at the center of the gate gap. This gap is 155 nm. See Fig. 4.3a-b for axis definition) as a function of wavelength using different hBN and SiO_2 refractive indices configurations for TM (first column, **a, c**) and TE-polarization (second column, **b, d**). In **a)** and **b)**, we use the full dispersive optical model for the hBN but not for the SiO_2, for which we use a wavelength independent refractive index of $n = 1.5$. In **c)** and **d)**, we use wavelength-independent refractive indices for hBN ($n = 2.4$), SiO_2 ($n = 1.5$) and alumina ($n = 1.6$).

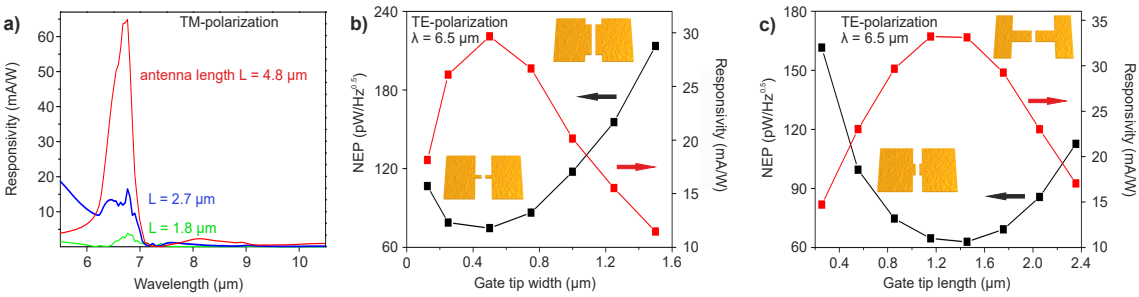

Fig. 4.13: Dependence of the simulated responsivity and NEP on the geometry of the antenna and H-shaped gates. **a)** Simulations of responsivity for TM-polarization for different antenna lengths. Different cases are presented: non-resonant antenna within the hBN RB spectral range (antenna total length of $L = 1.8$ μm, shown in green), semi-resonant antenna ($L = 2.7$ μm shown in blue, which corresponds to the experimental antenna) and resonant antenna ($L = 4.8$ μm, shown in red). **b)** Simulations of responsivity and NEP as a function of gate tip width and graphene (following the exact shape of the gates) as shown in the schematic for TE-polarization at $\lambda =$ 6.5 μm. The tip length is 855 nm, which includes the gap between the gates of 155 nm. The source-drain distance is 2.6 μm and electrodes width is 2 μm as in the measured device. **c)** Same as **b** but as a function of the gate tip length as shown in schematic. The tip width is 500 nm.

To evaluate the coupling between the bow-tie antenna LSPR and the hBN HPPs, we study the responsivity as a function of the antenna length for TM-polarization as shown in Fig. 4.13a (see also Fig. 4.14). We observe some hBN HPP excitation when using an antenna non-resonant (green line) within the hBN RB range, in which case we obtain a maximum responsitivity of 4 mA/W. In the case of the semi-resonant antenna (experimental antenna, shown in blue line), whose LSPR partially overlaps with the RB spectral range[104], the responsivity increases to 17 mA/W respectively. However, this can be significantly improved if we use a longer antenna (red line) such that its LSPR peak fully overlaps with the hBN HPPs peak, thus obtaining 65 mA/W.

Next, we examine the impact of the H-shaped gates excited at $\lambda =$ 6.5 μm with TE-polarization on the responsivity and NEP (noise-equivalent power, see 2.3.4) by varying the width and length of the gate tip and graphene, while keeping the source-drain distance and width fixed as indicated in Fig. 4.13b-c. Fig. 4.13b shows that the responsivity (NEP) increases (decreases) when decreasing the tip width down to an optimal value of 500 nm (same as the experimental value). This is ascribed to the balancing act of absorption, electrical resistance and thermal conductance: larger absorption and lower thermal conductance increase the temperature gradients, but a smaller electrical conductance also reduces the photocurrent and thus the responsivity (see also Fig. 4.15 and section 4.8). Note that electrical and thermal conductivity are ultimately proportional through the Wiedemann-Franz law. For the case of the gate tip length, however, the optimum is found around 1.45 μm, which is larger than the experimental one (855 nm), pointing to future design and performance improvements (see also Figs. 4.5 and 4.15). These results highlight the importance of the gate and graphene channel shapes on PTE performance and the vital role of multiphysics modeling in understanding and optimizing such a complex device.

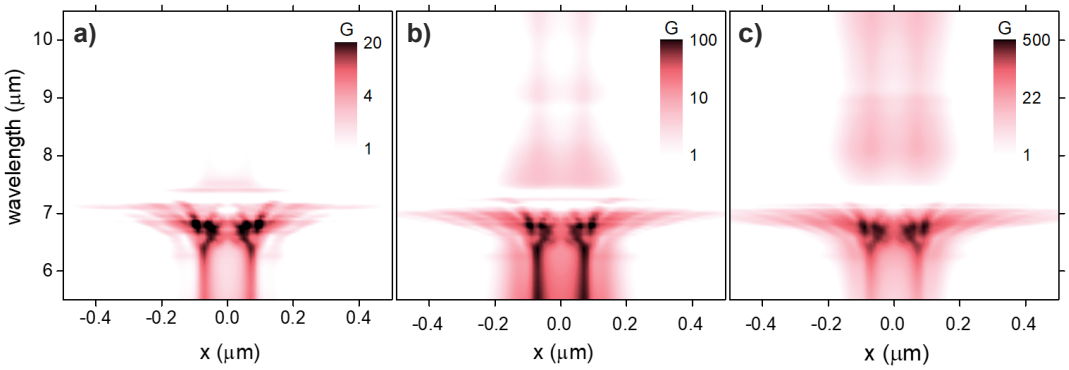

Fig. 4.14: 2D map of the simulated absorption enhancement G for TM-polarization along the source-drain direction (x direction and averaging over 500 nm in y direction, where $x = 0$ is located at the center of the gate gap. This gap is 155 nm. See Fig. 4.3a-b for axis definition) as a function of the wavelength (y-axis of the map) for total antenna lengths of **a)** $L = 1.8$ µm (non-resonant antenna within hBN RB), **b)** $L = 2.7$ µm (experimental/semi-resonant antenna within hBN RB) and **c)** $L = 4.8$ µm (resonant antenna within hBN RB). For longer antennas, we notice that the LSPR of the antenna is strongly coupled with the hBN HPPs as observed in the G map in **c**.

4.5.3 Speed, sensitivity and device benchmark.

Now we discuss the technological relevance of our photodetector. First, we measure the photodetection speed by using as reference a commercial fast mercury-cadmium-telluride (MCT) detector. We plot in Fig. 4.16a the quantum cascade laser (QCL) voltage (brown line) together with the photoresponses of the MCT (blue line) and our device (black circles). The signal of the MCT detector reveals the pulse shape of the laser. We fit an exponential function to the initial peak to determine the rise time (shown in red lines), obtaining a value of 9.5 ns, which is close to its datasheet value of 4.4 ns. In the case of our photodetector, we find a rise time of 17 ns (22 MHz) when using a current amplifier with 14 MHz bandwidth. This suggests that our time-resolved measurements are limited by the current amplifier bandwidth (see Fig. 4.17), meaning that the actual rise time may be shorter. In fact, our theoretical calculations predict a speed of 53 ps (see section 4.7).

The sensitivity of the detector is best expressed in terms of external responsivity, which the maximum measured value is 27 mA/W (92 V/W, see Fig. 4.18), yielding a noise-equivalent-power of 82 pW/$\sqrt{\text{Hz}}$[13,64,108–110], assuming the graphene thermal noise as the dominating noise source[66,80,100]. We emphasize that the zero-bias operation leads to low noise levels and a very low power consumption, which is given by the voltage applied to the gates. Furthermore, our design allows sensitive detection in different polarizations (see also Fig. 4.19), which is a limitation for the mentioned graphene detectors[13,64,108,109]. Additionally, our device exhibits a wide dynamic range by showing linear photoresponse over three orders of magnitude as shown in Fig. 4.16b, which is an issue for other types of graphene detectors[108] and commercial detectors such as MCT[2]. It also has a very small active area given by the antennas' cross-sections, which implies high spatial resolution and opens the possibility of arranging it into high density photodetector pixels[1,13] that are CMOS compatible[3]. All of these performance parameters combined make our device an

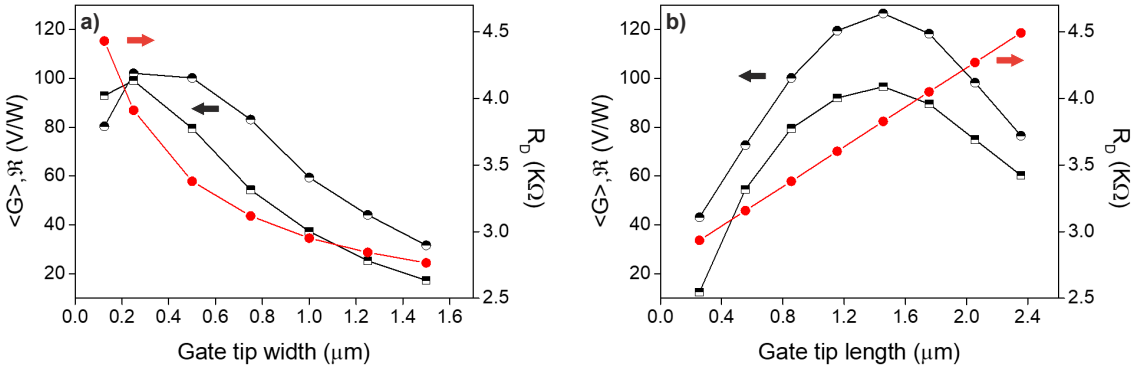

Fig. 4.15: Simulated responsivity (Re in V/W, shown in black circles), $<G>$ (defined in Fig. 4.5, black squares) and device resistance ($R_{\mathbf{D}}$, shown in red circles) as a function of the geometric parameters of the H-shaped gates for TE-polarization at λ= 6.5 μm. **a)** Here we vary the tip width ($W_{\mathbf{GT}}$). The gate tip length ($L_{\mathbf{GT}}$) is fixed at 855 nm. We observe that $W_{\mathbf{GT}}$ correlates inversely with $<G>$. We attribute this trend to the fact that the plasmonic response of the local gates decreases with the increase of $W_{\mathbf{GT}}$ as shown in Fig. 4.5c. The only case that does not follow this trend is the case of $W_{\mathbf{GT}}$ =0.125 μm. In this case $<G>$ decreases because $W_{\mathbf{GT}}$ is smaller than the 0.2 μm gap between the branches of the bow-tie antenna, thus preventing the gates and antenna from overlapping, while the overlap region precisely contains the highest values of G as shown in Fig. 4.11. As shown in Fig. 4.21, lower $<G>$ values lead to smaller temperature gradients and consequently lower responsivities, since the responsivity is positively correlated with $<G>$. Finally, as $W_{\mathbf{GT}}$ increases the width of the doped graphene channel also increases leading to smaller $R_{\mathbf{D}}$. The interplay between responsivity and $R_{\mathbf{D}}$ gives the optimum $W_{\mathbf{GT}}$ case as shown in Fig. 4.13b. **b)** Here we vary $L_{\mathbf{GT}}$. $W_{\mathbf{GT}}$ is fixed at 500 nm. We observe that $<G>$ has a clear peak at $L_{\mathbf{GT}}$ = 1.455 μm. This trend is in excellent agreement with results in Fig. 4.5d-e, where the configuration using the same value of $L_{\mathbf{GT}}$ has the strongest response in the spectral position of the hBN upper RB. As in **a**, the responsivity positively correlates with $<G>$ and although $R_{\mathbf{D}}$ increases with $L_{\mathbf{GT}}$, the optimum cases among all figures of merit (FOM) (Responsivity in V/W, A/W and NEP) remain roughly the same.

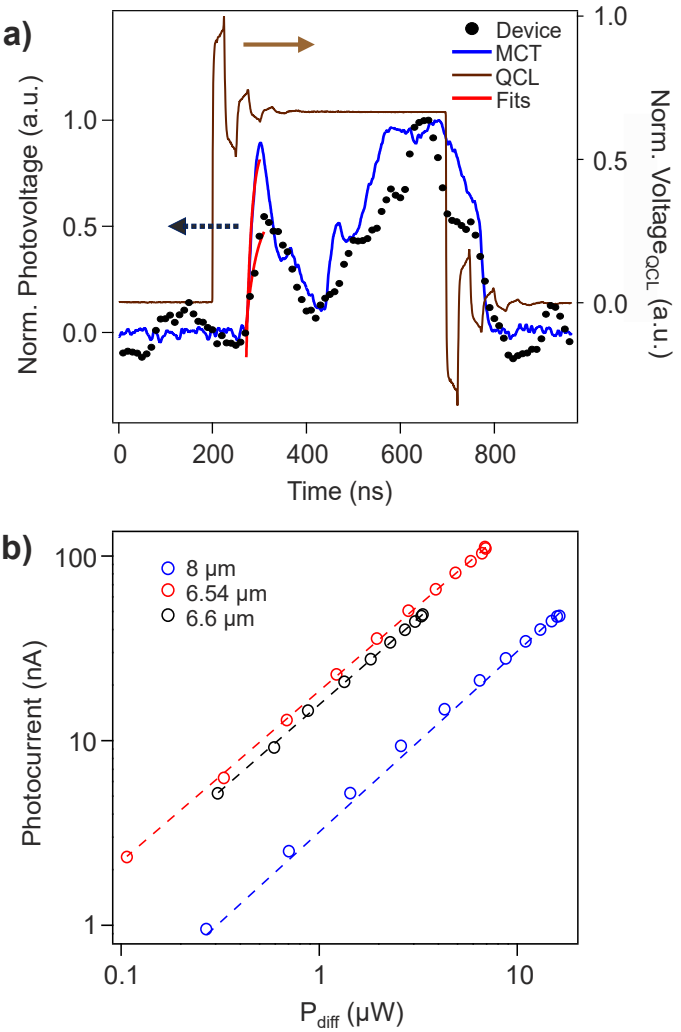

Fig. 4.16: Photodetection speed and power dependence. **a)** Time-resolved photodetection traces at $\lambda = 6.6$ µm, compared with a MCT detector (both plotted in black dots and blue line respectively) and the respective QCL voltage signal (brown line). The QCL pulse width corresponds to 496 ns. The photovoltage fits are shown in red lines. We obtain rise times of 9 $\pm$ 3 ns and 17 $\pm$ 3 ns for the MCT and our device respectively. **b)** Photocurrent as a function of laser power ($P_{\mathbf{diff}} = P_{\mathbf{in}} \times A_{\mathbf{diff}} / A_{\mathbf{focus}}$, see Methods) for different wavelengths on a log-log scale. Circles correspond to the data points, while the dashed lines represent the fits according to $I_{\mathbf{PTE}} \propto P_{\mathbf{diff}}^{\gamma}$. Among all cases, γ ranges from 0.92-0.98. We observe linear photoresponse over three orders of magnitude of power (limited by the power meter sensitivity range for $P_{\mathbf{in}}$ calibration). These results suggest that we are operating in the weak heating regime ($T_{\mathbf{e}} - T_{\mathbf{l}} << T_{\mathbf{l}}$)[23,100], as in the strong heating regime ($T_{\mathbf{e}} - T_{\mathbf{l}} >> T_{\mathbf{l}}$), a sublinear behavior is expected ($\gamma = 0.5$)[23,100]. Here $T_{\mathbf{e}}$ is the electronic temperature and $T_{\mathbf{l}}$ is the graphene lattice temperature, which the latter is in thermal equilibrium with the environment.

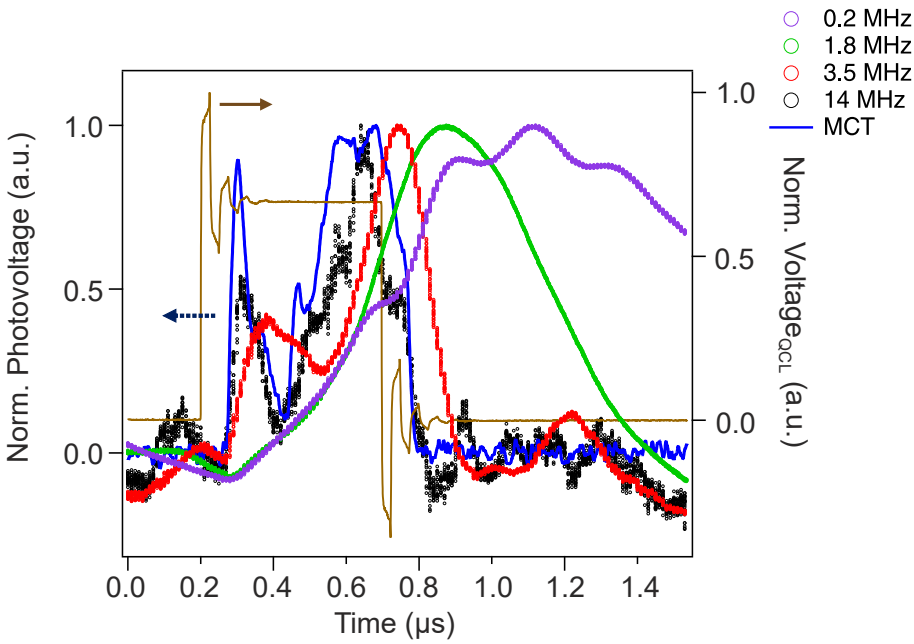

Fig. 4.17: Time-resolved photodetection traces for different operation bandwidths of the current amplifier. The speed increases (shorter rise time) with increasing bandwidth and the temporal response curve also resembles the photovoltage measured with the reference MCT detector as shown in blue solid line. The corresponding QCL voltage signal is shown in brown solid line.

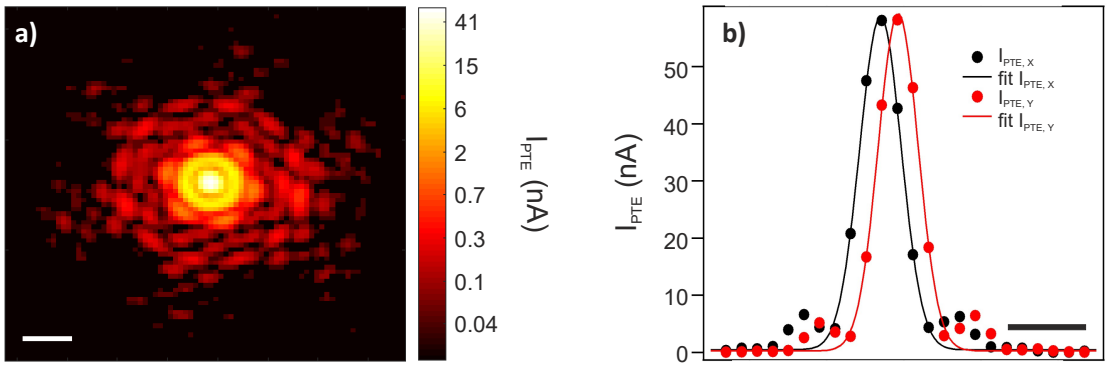

Fig. 4.18: Scanning photocurrent map at $\lambda = 6.6$ μm with TE-polarization. **a)** Scanning photocurrent map (log scale) over the x and y scan directions. We observe an Airy beam pattern consisting of a central spot followed by several rings that contain a very small fraction of the total input power ($P_{\mathbf{in}} = 13.7$ μW, $P_{\mathbf{diff}} = 2.1$ μW). The white scale bar stands for 20 μm. **b)** Linecuts of the map in **a**, showing $I_{\mathbf{PTE}}$ across the x (black) and y (red) direction. The scale bar corresponds to 10 μm. The dots represent the experimental $I_{\mathbf{PTE}}$ and the curves represent Gaussian fits. We obtain $w_{0,\mathbf{x}} = 5.4$ μm and $w_{0,\mathbf{y}} = 5.2$ μm. The maximum responsivity value achieved was 27 mA/W (92 V/W) which corresponds to a NEP of 82 pW/$\sqrt{\mathbf{Hz}}$, with a noise spectral density of 2.21 pA/$\sqrt{\mathbf{Hz}}$ for a device resistance of 3.38 kΩ at the *pn*-junction configuration given by $E_{\mathbf{F,L}} = 85$ meV, $E_{\mathbf{F,R}} =$ -105 meV.

interesting platform that fulfills the ongoing trend of decreasing the size, weight and power consumption (SWaP) of infrared imaging systems[2].

4.6 Photoresponse modeling

We develop the modeling of the photoresponse in collaboration with Elefterios Lidorikis group from University of Ioannina as discussed in the following sections.

4.6.1 Optical modeling

We perform optical calculations with the full vector 3D finite-difference time domain (FDTD) method using Lumerical software. The computational cell dimensions are 6×6×6 μm^2 with perfectly matched layer (PML) conditions employed on all boundaries. We use a grid of 5 nm in lateral (x,y) and 2 nm in vertical (z) directions. The light source is modeled as an incident plane wave reaching the device through an open aperture of 5.9×5.9 μm^2 with spectral range 5.5-10.5 μm. The dimensions of the device layers are described in section 4.2.

We fit the Au dielectric function using the Drude model $\varepsilon(\omega) = \varepsilon_\infty - \omega_{\mathbf{P}}^2/(\omega^2 + \mathrm{i}\Gamma\omega)$ with $\omega_{\mathbf{P}}$ the plasma frequency and Γ the plasma collision rate. hBN is optically anisotropic [28], with different permittivities along the in-plane ($\perp c$) and out-of-plane ($\| c$) directions. We fit both using the Lorentz model $\varepsilon(\omega) = \varepsilon_\infty + s\omega_0^2/(\omega_0^2 - \omega^2 - \mathrm{i}\gamma\omega)$, where s is a

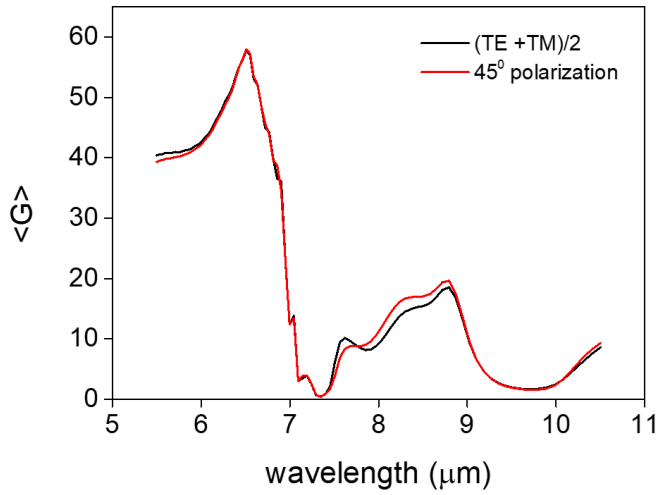

Fig. 4.19: Simulated absorption enhancement averaged over an area of 0.2×0.2 μm^2 around the device center ($x = y = 0$) for a 45 degree incident polarization respect to the bowtie antenna main axis (red curve) compared to the average TE and TM response (black curve). This result demonstrates that our system is linear and the photoresponse for an incident oblique polarization is the sum of the two components (TE and TM).

dimensionless coupling factor, ω_0 the normal frequency of vibration and γ the decay rate amplitude. Table 4.1 shows the parameters for Au and hBN. The refractive indices used for SiO_2 and Al_2O_3 are taken from literature[111], while for Si we use $n_{\mathbf{Si}} = 3.42$. Graphene is implemented as a 2D surface with optical response modeled by the Kubo conductance[112] $\sigma = \sigma_{\mathbf{intra}} + \sigma_{\mathbf{inter}}$, where:

$$\sigma_{\mathbf{intra}} = \frac{ie^2}{\pi\hbar^2\Omega}\int_0^\infty \epsilon(\partial_\epsilon f(-\epsilon;\mu,T_{\mathbf{e}}) - \partial_\epsilon f(\epsilon;\mu,T_{\mathbf{e}}))d\epsilon \tag{4.1}$$

$$\sigma_{\mathbf{inter}} = \frac{ie^2\Omega}{\pi\hbar^2}\int_0^\infty \left(\frac{f(-\epsilon;\mu,T_{\mathbf{e}}) - f(\epsilon;\mu,T_e)}{\Omega^2 - 4(\epsilon/\hbar)^2}\right)d\epsilon \tag{4.2}$$

Here Ω is defined as $\Omega = \omega + i\tau_{\mathbf{opt}}^{-1}$, $\tau_{\mathbf{opt}} = 200$ fs is the assumed electron relaxation time, $f(\epsilon;\mu,T_e) = [e^{(\epsilon-\mu)/k_B T_e} + 1]^{-1}$ is the Fermi-Dirac distribution and $\partial_\epsilon = \partial/\partial\epsilon$.

Material	ε_∞	s	ω_0, ω_P [eV]	γ_0, Γ [eV]
hBN[28] $\perp c$	4.87	1.83	0.17	0.87
hBN[28] $\parallel c$	2.95	0.61	0.0925	0.25
Au[113]	10.78	-	9.13	0.07

Table 4.1: Dielectric permittivity parameters of Au and hBN.

4.6.2 Thermoelectric modeling

We assume the quasi-continuous-wave case and solve the heat dissipation equation[43]:

$$-\nabla\cdot(\kappa\nabla T_{\mathbf{e}}) = \nabla\Pi\cdot\mathbf{j_q} - \tau_{\mathbf{e-ph}}^{-1}c_{\mathbf{e}}\Delta T + \alpha P_{\mathbf{dens}} \tag{4.3}$$

where κ is the electronic thermal conductivity, T_e the electronic temperature, $\Pi = S T_e$ the Peltier coefficient, S the Seebeck coefficient, $\mathbf{j_q} = -\sigma S \nabla T_e$ the local thermoelectric current, σ the electrical conductivity, τ_{e-ph} the average cooling time (3 ps), c_e the electronic heat capacity, $\Delta T = T_e - T_l$, T_l is the lattice temperature, α the absorption fraction and the incident power density $P_{dens} = P_{in}/A_{diff}$, where P_{in} is the source power and $A_{diff} = \lambda^2/\pi$ is the diffraction-limited area. The term c_e/τ_{e-ph} in Equation 4.3 is equivalent to Γ_{cool}, where Γ_{cool} ($\sim$ 4-5$\times 10^4$ W/Km^2) is the interfacial heat conductivity[45,100]. Due to the large lattice heat capacity (compared to the electronic one) we assume constant T_l = 300 K. The graphene parameters $\sigma, S, c_e, \kappa, \Gamma_{cool}$ and α are functions of position, depending on both the local Fermi level E_F and the local temperature T_e, making this a highly non-linear problem. The self-consistent solution of Equation 4.3 provides the T_e distribution from which the thermoelectric voltage is obtained:

$$V_{PTE} = W^{-1} \int_0^W \int_0^L S \nabla T_e dx dy \tag{4.4}$$

where the length L is the distance between the contacts (assumed in the x direction, as shown in Fig. 4.3a-b in the main text) and W the width of the graphene channel (y direction, as shown in Fig. 4.3a-b). The photocurrent is then $I_{PTE} = V_{PTE}/R_D$, where $R_D = R_g + 2R_c$ with R_g is the resistance of graphene channel $R_g = \int_0^L \sigma^{-1}(x)dx$, $\sigma(x) = \int_0^W \sigma(x,y)dy$ and R_c the contact resistance of the device. The responsivity and NEP are calculated following the description in section 2.3.4.

Most parameters in the above equations depend on the local Fermi level and electronic temperature. The former is obtained from the graphene charge density $E_F = \hbar v_F \sqrt{\pi n^{(0)}}$, where $n^{(0)}$ is calculated by electrostatic simulations (see section 4.6.3 and Fig. 4.20) using the ratio ϵ_{hBN}/d_{hBN} as determined by fitting the measured device resistance (see section 4.6.4). At finite temperature we obtain the chemical potential from the solution of $\int_0^\infty \nu(\epsilon) f(\epsilon; \mu, T_e) - f(\epsilon; -\mu, T_e) d\epsilon = E_F^2/\pi\hbar^2 v_F^2$, where $\nu(\epsilon) = \frac{2|\epsilon|}{\pi\hbar^2 v_F^2}$ is the graphene density of states at energy ϵ and $v_F = 1\times 10^6$ m/s the graphene Fermi velocity. The rest of the graphene electrical and thermal parameters are calculated as follows:

Electrical conductivity:
$\sigma(\mu, T_e) = \int_{-\infty}^{\infty} \sigma(\epsilon) \partial_\epsilon f(\epsilon; \mu, T_e) d\epsilon$, where $\sigma(\epsilon) = q[\mu_q n(\epsilon) + \bar{\mu} n^*(\epsilon)]$, with charge carrier mobility $\mu_q = \mu_e(\mu_h)$ for $\epsilon > 0 (\epsilon < 0)$ and $\bar{\mu} = (\mu_e + \mu_h)/2$. The effective residual local charge fluctuation at energy ϵ is assumed to be $n^*(\epsilon) = \sqrt{n(\epsilon)^2 + n_0^{*2}} - n(\epsilon)$, where $n(\epsilon) = \frac{\epsilon^2}{\pi\hbar^2 v_F^2}$ is the graphene charge density at energy ϵ and n_0^* is the residual local charge fluctuations in the charge neutrality point[85,87].
Seebeck coefficient is given by the general Mott formula[114]:
$S(\mu, T_e) = -(|e| T_e \sigma)^{-1} \int_{-\infty}^{\infty} (\epsilon - \mu)\sigma(\epsilon) \partial_\epsilon f(\epsilon; \mu, T_e) d\epsilon$
Thermal capacity[115]:
$c_e(\mu, T_e) = \partial_{T_e} \int_0^\infty (\nu(\epsilon)\epsilon [f(\epsilon; \mu, T_e) + f(\epsilon; -\mu, T_e)] d\epsilon$
Thermal conductivity: is given by the Wiedemann-Franz law $\kappa(\mu, T_e) = L_0 \sigma(\mu, T_e) T_e$, where $L_0 = 2.44 \times 10^{-8} W\Omega K^{-2}$ is the Lorenz number.

4.6.3 Electrostatic modeling

The surface charge density of the graphene sheet is calculated by solving the Poisson equation after applying the appropriate voltages $V_{\mathbf{L}}$ and $V_{\mathbf{R}}$ at the two branches of the split gate. The graphene channel is introduced as a grounded surface above the hBN dielectric spacer layer. The nearby metal contacts are also set to ground. The dielectric constants of Si, SiO_2 and hBN are set to 11.7, 3.9 and 3.5[46,116,117] respectively. The surface charge density is calculated for both symmetric and anti-symmetric gating cases (see Fig. 4.20a).

4.6.4 Device resistance modeling

The measured device resistance $R_{\mathbf{D}}$ as a function of symmetric gate voltage ($V_{\mathbf{L}}$=$V_{\mathbf{R}}$) is fitted considering $R_{\mathbf{D}} = R_{\mathbf{g}} + 2R_{\mathbf{c}}$ and with fitting parameters the electron-hole mobilities, the residual local charge fluctuations n_0^*, the value of $\varepsilon_{\mathbf{hBN}}/d_{\mathbf{hBN}}$, the Dirac voltage $V_{\mathbf{D}}$ (for charge neutrality) and the contact resistance $R_{\mathbf{c}}$. The charge density distribution is obtained by the electrostatic calculations. We obtain $\mu_{\mathbf{e}}(\mu_{\mathbf{h}})$ =10,200 (11,900) $cm^2V^{-1}s^{-1}$, $n_0^* = 1.72 \times 10^{11}$ cm^{-2}, $V_{\mathbf{D}} = 0.108$ V and $\varepsilon_{\mathbf{hBN}}/d_{\mathbf{hBN}} = 0.222$ nm^{-1}. From the latter we extract hBN thickness $d_{\mathbf{hBN}} = 15.7$ nm, in excellent agreement with the 15 nm used in this work, validating our approach. The contact resistance is described with a Gaussian distribution around the charge neutrality point[118], with $R_{\mathbf{c}} = 0.2$ (0.9) kΩ at high (low) doping (see Fig. 4.2).

4.7 Speed calculations

The operation frequency of the photodetector is intrinsically related to the RC-time constant $\tau = R_{\mathbf{D}} C_{\mathbf{D}}$, with $R_{\mathbf{D}}$ as the total device resistance (see section 4.6.2 and 4.6.4) and $C_{\mathbf{D}}$[119] as the total device capacitance given by $C_{\mathbf{D}}^{-1} = C_{\mathbf{q}}^{-1} + C_{\mathbf{G}}^{-1}$, where $C_{\mathbf{q}}$ is the quantum graphene capacitance and $C_{\mathbf{G}}$ is the capacitance of the system as given by the normal formula for parallel-plate capacitors (for the case where $V_{\mathbf{L}} = V_{\mathbf{R}} = 0.5$ V and $\varepsilon_{\mathbf{hBN}}/d_{\mathbf{hBN}} = 0.222$ nm^{-1} as described in section 4.6.3 and 4.6.4. The operating speed is then described by the rate $f = (2\pi\tau)^{-1}$ and the rise time $\tau_{\mathbf{rise}}$, which is the time required for the photodetector to increase its output signal from 10% to 90% of the final steady-state output level. The rise time is calculated as $\tau_{\mathbf{rise}} = \tau \times \ln(9) = (2\pi f)^{-1} \cdot \ln(9) = 0.35/f$.

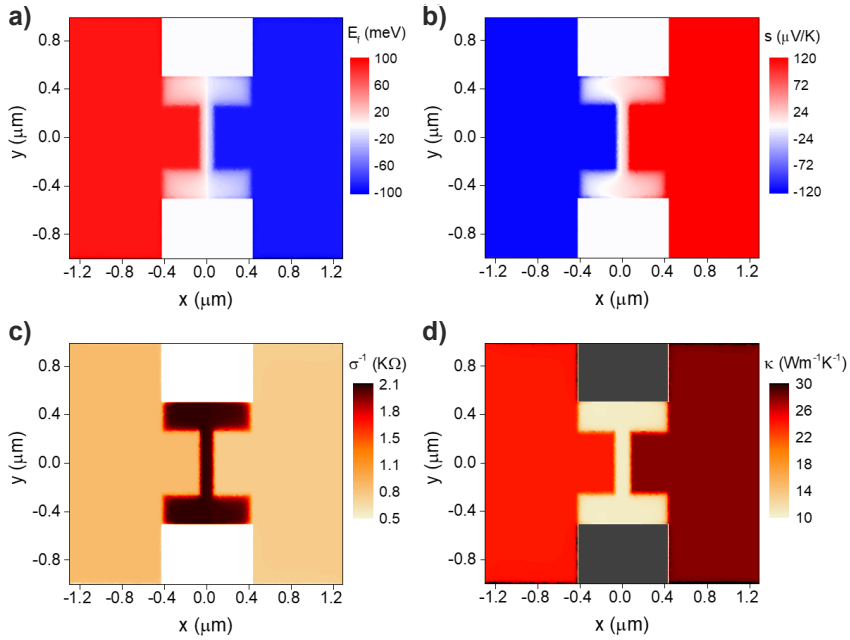

Fig. 4.20: Electrical and thermal properties of the graphene channel when applying 0.5 V (-0.5 V) to the left (right) gate. **a)** Calculated Fermi energy for the *n*-doped region (above left gate region) and *p*-doped region (above right gate region). In the gate gap, which is 155 nm, the Fermi energy drops to zero as we move from the *n*-doped to the *p*-doped gated region. Low values of the Fermi energy are also present in the graphene patches that extend 250 nm above and below the gate tips. **b)** Calculated Seebeck coefficient of the different graphene regions. As with the Fermi energy, the Seebeck coefficient drops to zero in the gate gap. Due to the difference in electron and hole mobilities, an imbalance is present in the weakly doped regions. Calculated **c)** resistivity and **d)** thermal conductivity. These two parameters are inversely proportional via the Wiedemann-Franz law.

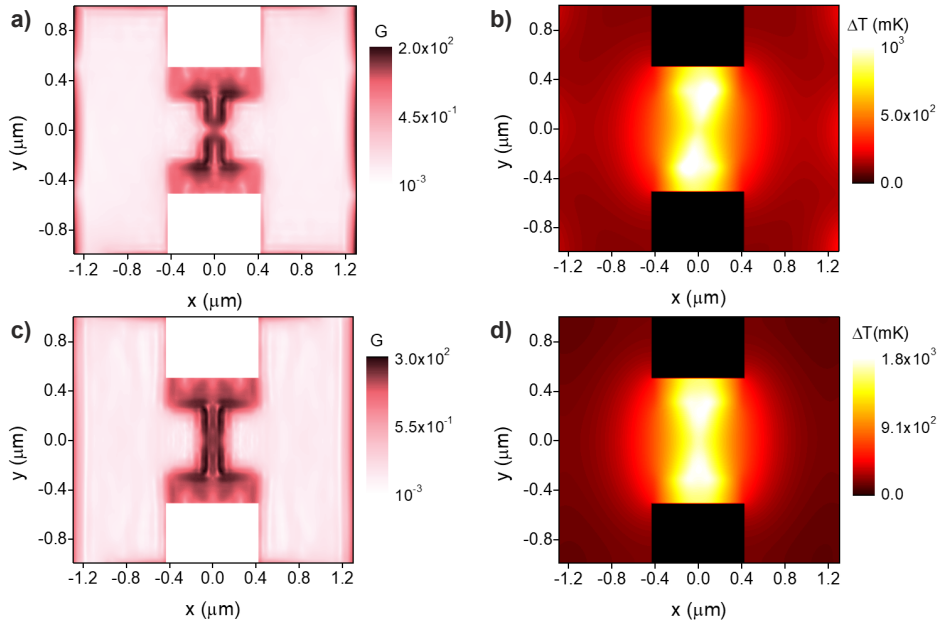

Fig. 4.21: a) G values in the graphene channel and **b)** temperature distribution for TM-polarization and **c)** and **d)** for TE-polarization respectively. For both cases the incident wavelength is 6.5 μm. In both polarizations we observe the maximum values of G in an area of 0.4×0.5 μm^2 around the center of the *pn*-junction (x=0, y=0). The fact that in the rest of the graphene channel G values are 3-4 orders of magnitude lower compared to the ones above indicates efficient light focusing in the *pn*-junction. This enhanced absorption and low thermal conductivity (shown in Fig. 4.20d) across the *pn*-junction results in high temperature concentration, as is evident in **b** and **d**. Note that the difference in G values for the two cases corresponds to a difference in peak temperatures and finally in difference a responsivity as shown in Fig. 4.6.

4.8 Gate gap effect on the photoresponse

We perform a set of simulations for the TM-polarization case changing the gate gap between 100 nm and 400 nm to observe its effect on the photoresponse performance. Specifically, as shown in Fig. 4.22a, the averaged spectral absorption enhancement profile $<G>$ is different for all cases, especially for the case of 400 nm gap where the peak values are much lower than the rest of the cases. This indicates that the interference patterns of hBN HPPs are affected by the gate gap. In terms of responsivity (Fig. 4.22b), these differences become more pronounced, as we can observe a clear optimum case for the 100 nm gap (the lower limit in terms of fabrication), while the performance of the 400 nm gap case is by far inferior. To elucidate this behaviour, we examine the spatial profiles of the parameters that affect the device performance, such as absorption (Fig. 4.23), hot electron temperature distribution (Fig. 4.25) and PTE voltage density (Fig. 4.27) for the cases of 100, 200, 300 and 400 nm gap at the wavelength where the maximum responsivity is observed for each case. Absorption profiles in Fig. 4.23 clearly explains the trends in Fig. 4.22a. As the overlap between the bowtie antenna and the tips of the gates decreases (by increasing the gap of the latter), both relative strength and spatial pattern is strongly altered. For 100 nm gap we observe large values of absorption, which however are concentrated beyond the gate edges where thermal conductivity is high (see Fig. 4.24). For 400 nm gap, on the other hand (no gate-antenna overlap) the absorption is strongly diminished but also more uniformly distributed inside the gap where thermal conductivity is low (see Fig. 4.24). These two conflicting attributes determine the temperature distribution as presented in Fig. 4.25. Indeed, as we increase the gap the differences we observe in peak temperature are smaller than those in absorption. Nonetheless, if we consider that for larger gaps the temperature peak is well centred within the gap area where the Seebeck coefficient (Fig. 4.26) has low values, we understand why PTE voltage generation diminishes for larger gaps, as is evident in Fig. 4.27. Taking also into account that resistance increases for larger gaps (see Fig. 4.28) explains the performance of our device as presented in Fig. 4.22b.

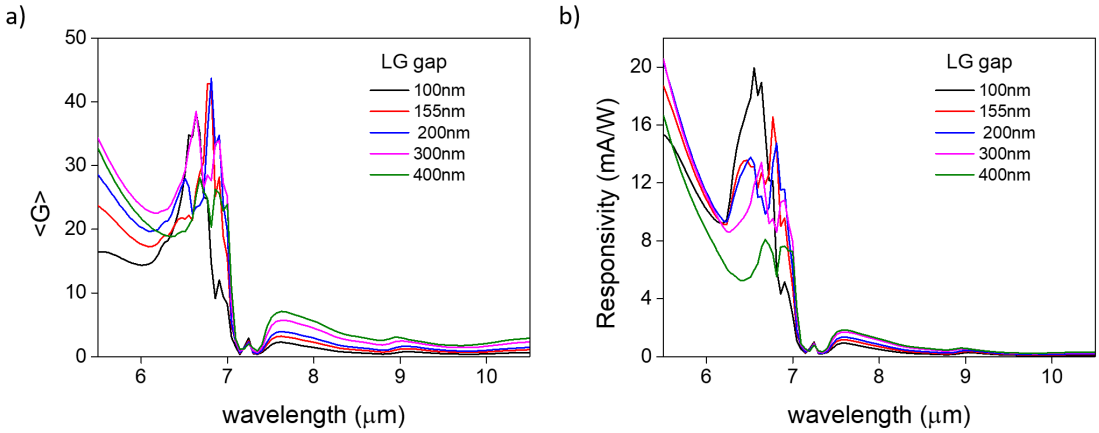

Fig. 4.22: a) Simulated $<G>$ (averaged over an area 0.5×0.5 μm^2 around the device center $x = y = 0$) for devices with different gate gaps with incident TM-polarization, **b)** corresponding spectral responsivity. The gate voltages configuration is $V_{L,R} = \pm 0.5$ V ($E_F = \pm 100$ meV).

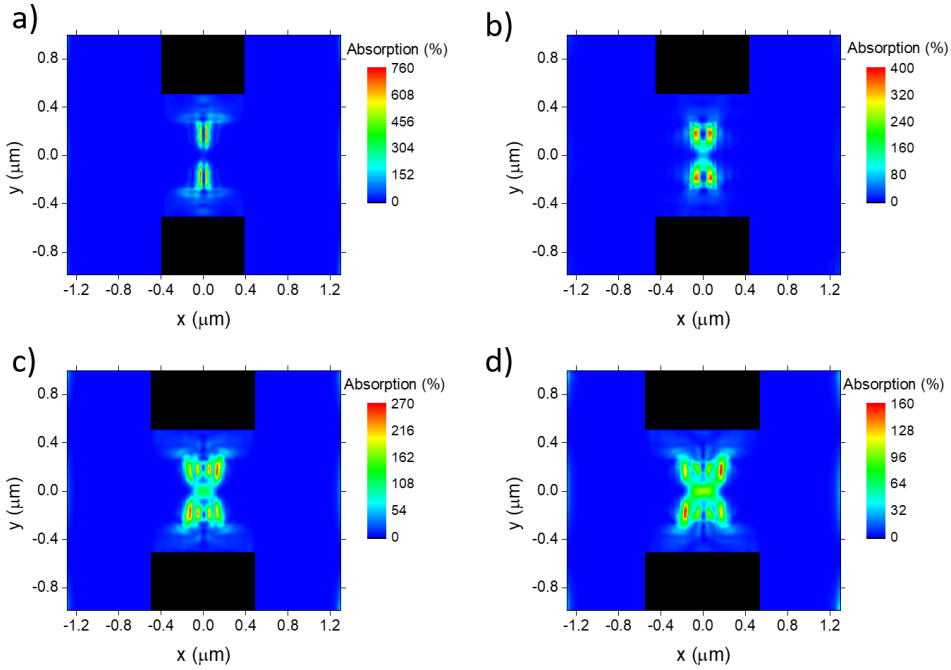

Fig. 4.23: Absorption distribution in graphene for TM-polarization with gate gap of **a)** 100 nm, **b)** 200 nm, **c)** 300 nm and **d)** 400 nm. The peak wavelength is chosen in each case ($\lambda = 6.551$, 6.767, 6.636 and 6.679 μm respectively). The gate voltage configuration is the same as displayed in Fig. 4.22.

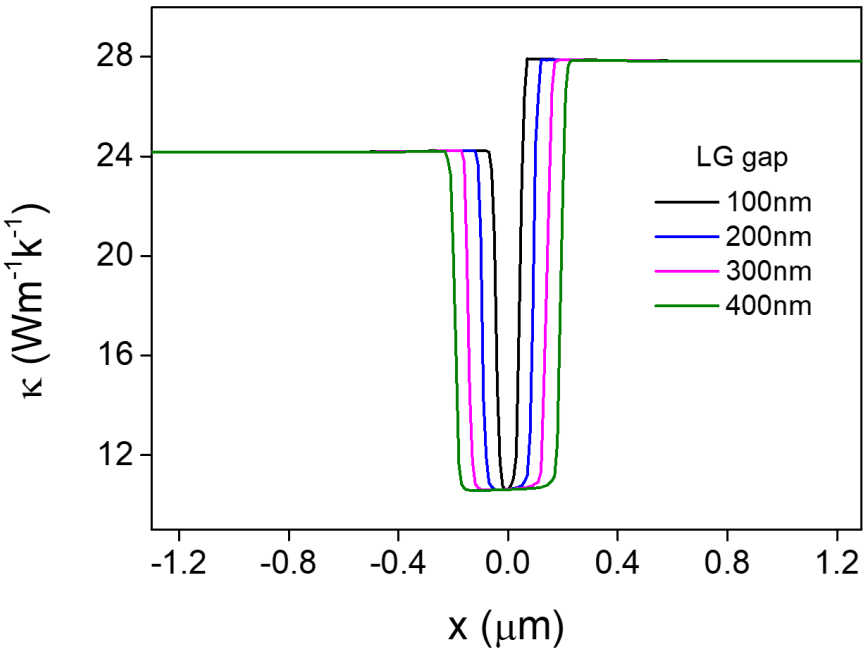

Fig. 4.24: Thermal conductivity across the graphene channel (at $y = 0$) for the devices with the different gate gaps and gate voltage configuration $V_{L,R} = \pm 0.5$ V ($E_F = \pm 100$ meV). The small imbalance is due to the difference in electron and hole mobilities.

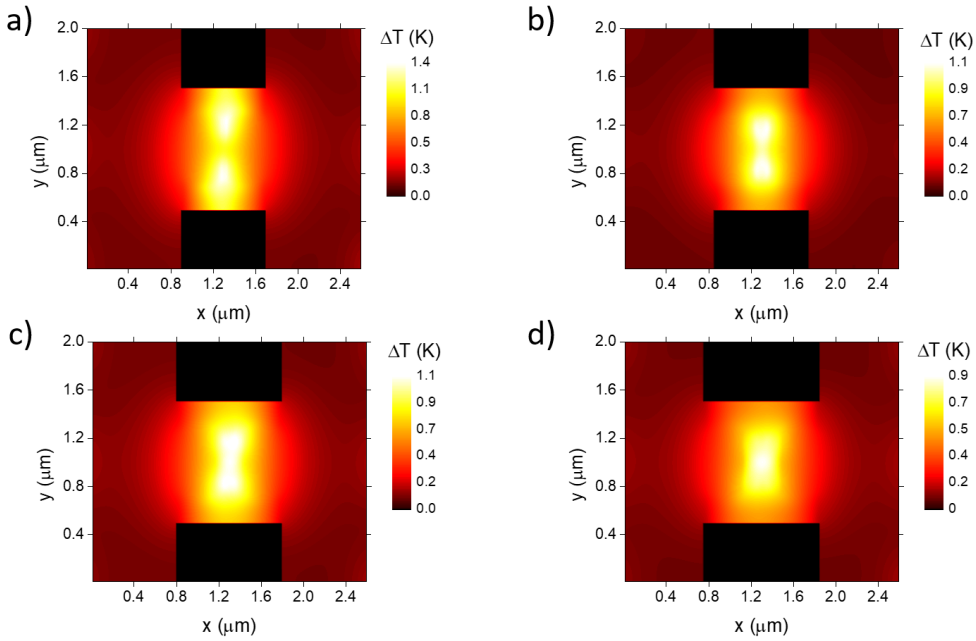

Fig. 4.25: Temperature distribution in graphene electrons for TM-polarization with gate gap of **a)** 100 nm, **b)** 200 nm, **c)** 300 nm and **d)** 400 nm. The peak wavelength chosen in each case is explained in Fig. 4.23. The gate voltages configuration is $V_{L,R} = \pm 0.5$ V ($E_F = \pm 100$ meV).

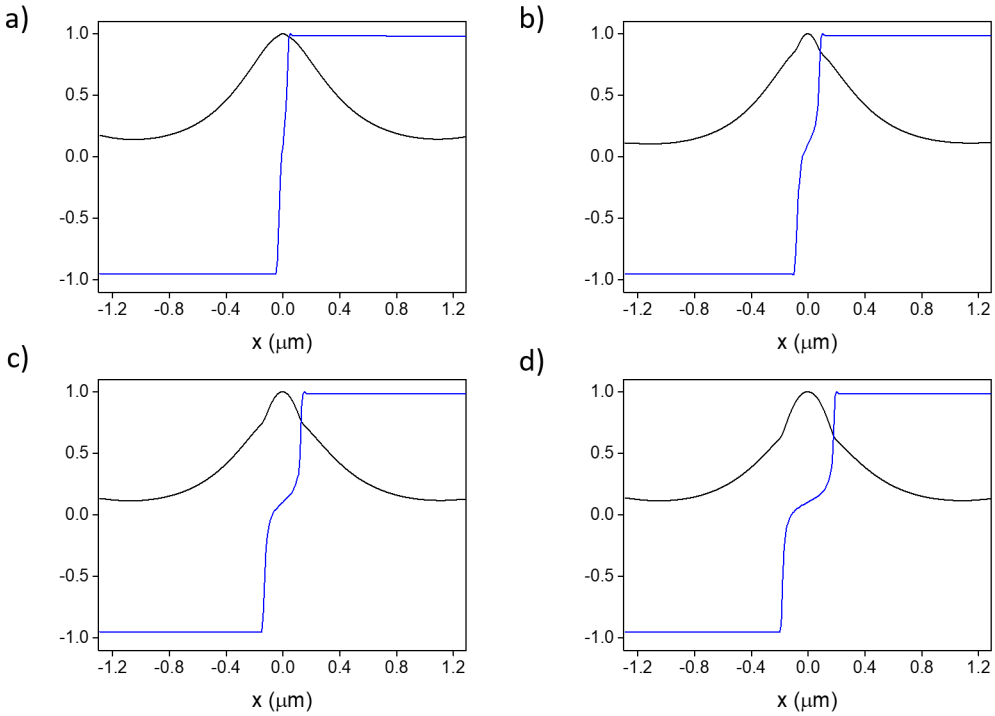

Fig. 4.26: Normalized ΔT (black lines) and Seebeck coefficient (blue lines) across the graphene channel (at $y = 0$) for TM-polarization with gate gap of **a)** 100 nm, **b)** 200 nm, **c)** 300 nm and **d)** 400 nm. The peak wavelength chosen in each case is explained in Fig. 4.23. The gate voltages configuration is $V_{\mathbf{L,R}} = \pm 0.5$ V ($E_{\mathbf{F}} = \pm 100$ meV).

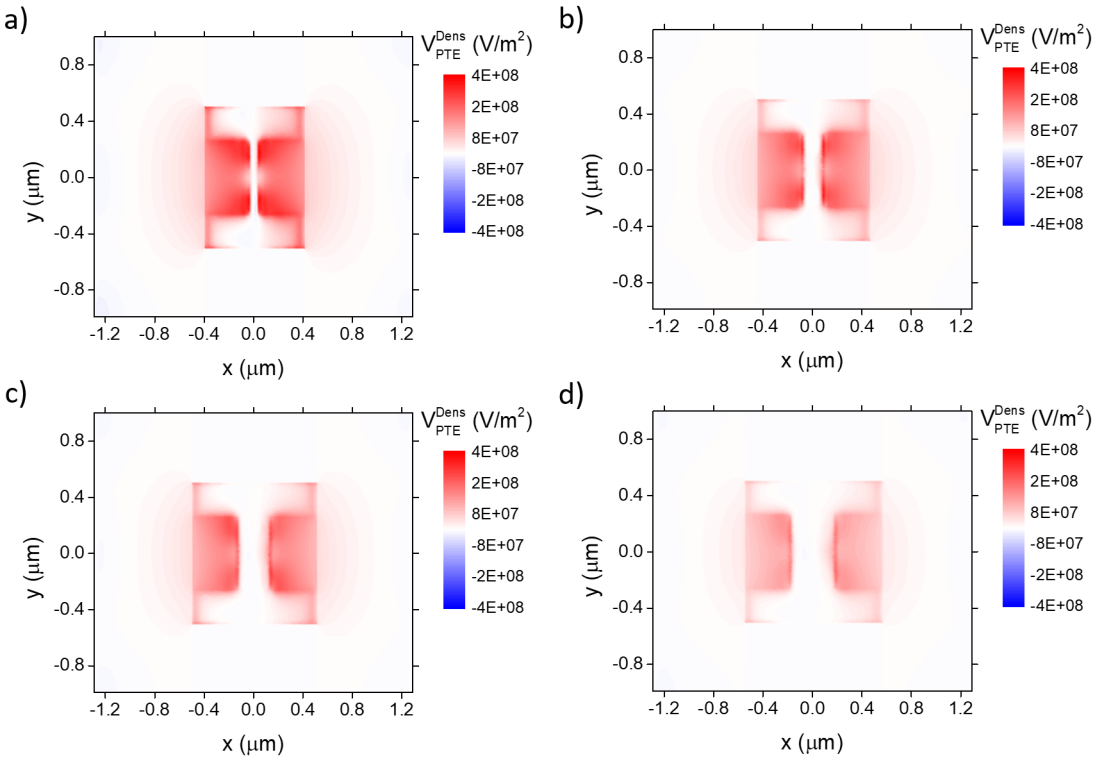

Fig. 4.27: PTE voltage density distribution in graphene for TM-polarization with gate gap of **a)** 100 nm, **b)** 200 nm, **c)** 300 nm and **d)** 400 nm. The peak wavelength chosen in each case is explained in Fig. 4.23. The gate voltages configuration is $V_{L,R} = \pm 0.5$ V ($E_F = \pm 100$ meV).

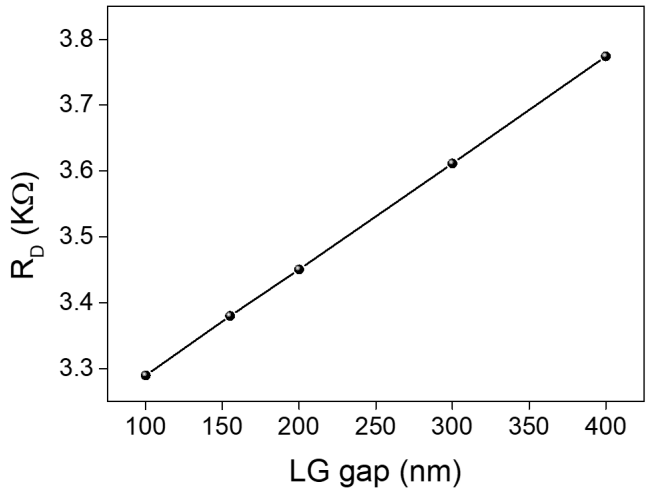

Fig. 4.28: Device resistance as function of the gate gap for the gate configuration $V_{L,R} = \pm 0.5$ V ($E_F = \pm 100$ meV).

4.9 Conclusions

In conclusion, we developed an efficient platform for coupling plasmonic antennas' resonances with HPPs launched towards a graphene *pn*-junction for sensitive and fast mid-IR photodetection. Additionally, we established a graphene *pn*-junction design that exploits the PTE response effectively by using a nearly optimum H-shaped graphene and gate design geometry and obtained a record performance of our room temperature photodetector in the mid-IR. Moreover, we developed a multiphysics model that elucidates the involved physics and predicts quantitatively the device photoresponse, which is useful for further investigation even beyond the mid-IR range. The device concept introduced in this work can be extended to detectors for other wavelengths or more specific functionalities such as hyperspectral imaging and spectroscopy. Our approach can also be combined with HPPs in other regions of the mid-IR and long-wave infrared range such as MoO_3 [120–122]. Additional tuning and wavelength sensitivity can be realized by controlling the hyperbolic material's thickness[64,123] or shape[35,124–126]. These above mentioned reasons make our platform very rich to further explore for fundamental and applications purposes.

5 Mid-infrared photocurrent spectroscopy via electrical detection of 2D polaritonic nanoresonators

5.1 Introduction

Spectral selectivity for mid and long-wave infrared detection is at the heart of a myriad of applications such as molecular spectroscopy,[4–6,127] thermal imaging,[13,106] etc. In particular, the energy range of the polaritons (e.g. plasmons, phonon polaritons) in 2D materials is spectrally located at these long wavelengths. The 2D polaritons have been widely explored in the last years due to its intriguing optoelectronic properties.[14,15,24] However, its employment for efficient photodetection in the mid-IR and LWIR range at room temperature has remained unexplored and typically an external detector (e.g. mercury cadmium telluride, also known as MCT) is required to probe them.

The electrical detection of graphene plasmons in the mid-infrared range was shown in ref. 13. It consisted on an array of graphene disks linked together with a narrow graphene ribbon[13]. A significant drawback of this approach is that it requires a high input bias in the graphene channel (1 V) for operation, which increases the noise level and the power consumption. Moreover, this approach requires to pattern the graphene, thus reducing significantly its mobility. Another related work was carried on by Bandurin et al. (ref. 81), which demonstrated bilayer graphene plasmons by measuring the device photoresponse in the terahertz regime (2.5 THz) that show high order of resonances produced at the channel as a function of the gate voltage. Nevertheless, the device required cryogenic temperatures ($\sim$5 K) to observe noticeable features in the photovoltage. We stress that despite the considerable advances shown in these investigations, none of them demonstrated infrared spectroscopy via the device photoresponse. Mainly, the photocurrent measurements were performed at a fixed value of frequency/wavelength that also prevents to exploit the underlying physics of these 2D polaritons, hence remaining elusive in particular for high quality graphene devices.

In this work, we merge into one single platform the polaritonic material and the detector. Hence, this approach prevents the need of using an external detector. The device can operate at ambient conditions and room temperature, under zero-bias and does not require graphene patterning. We fabricated 4 devices based on high quality graphene encapsulated by hexagonal boron nitride (hBN) on top of metallic rod arrays that serve to launch the hBN phonon polaritons and/or graphene plasmons. We also doped graphene via an electrostatic potential applied between these rods and graphene separated by a thin hBN layer. By following this approach we reach high Fermi level values of the order of 0.4 eV.

The design of these devices is meant to exploit the photothermoelectric effect by creating a graphene pn-junction using metallic gratings as local gates. This photocurrent mechanism has been described extensively in the previous chapters 3-4. However, in this case the rise in temperature is not caused by a strong light concentration at the gap of an antenna at the pn-junction interface as demonstated in previous chapters 3-4. Here, the strong absorption in graphene is designed to be mediated by graphene plasmons or hybridized plasmon phonon polaritons launched by the grating gates. The natural decay product of these polaritons is electronic heat diffusion, which causes a temperature gradient across the graphene channel that together with the doping asymmetry produce a photovoltage.[128] The main pathways of damping are due to dielectric losses in hBN and

graphene's thermal phonons.[128]

5.2 Device fabrication and working principle

We have produced 4 devices for transmission and photocurrent measurements. We use different device configurations depending the type of measurements, by mainly varying the grating location. For instance, we place the gratings on top of the 2D stack for the device used for transmission measurements (see Fig. 5.3a). Although this configuration provides an ideal situation for launching efficiently the polaritons[31,32] and achieving uniform gating across the graphene channel by using a Si backgate, its fabrication yield is quite low. One of the main challenges for this geometry is that for FTIR measurements we need a relatively large 2D stack area of around 30×30 μm^2 (see Fig. 5.1a) to obtain a decent signal-to-noise-ratio (SNR). The second reason is the metallic nano-gratings arduous lift-off step as shown in Fig. 5.1b, which sometimes needs sonication that harms the graphene quality.

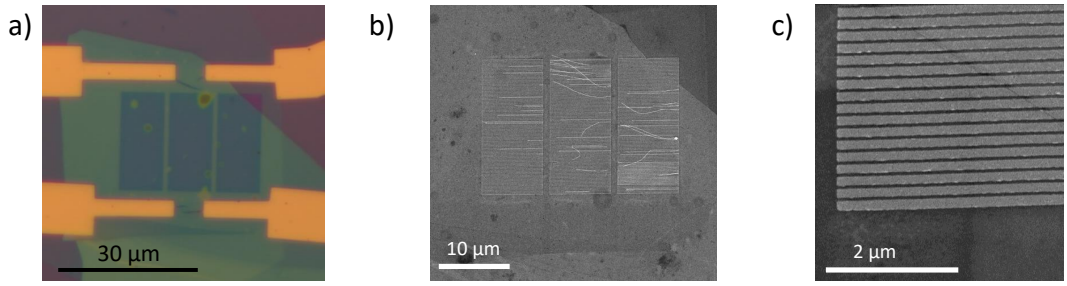

Fig. 5.1: **a)** Optical images of device 1. **b)** SEM picture of the gratings on top of the 2D stack of device 1. **c)** Zoomed SEM image of the gratings in **b**.

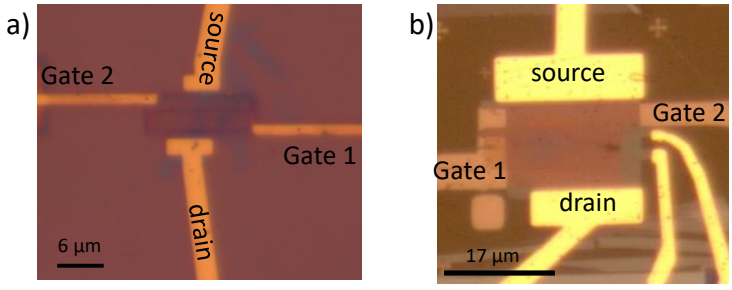

Fig. 5.2: Optical images of **a)** device 3 and **b)** device 4. Each picture indicates the correspondent scale bar.

In order to obtain higher yield of fabrication for these devices, we change the device configuration by placing the gratings below the 2D stack (for devices 2-4, see Fig. 5.4a). In fact, since the first fabrication steps are to pattern and evaporate the metallic gratings,

we can sonicate the substrate to avoid any lift-off issues thus achieving a high yield of fabrication of these nanostructures. We also pattern the metallic gratings of device 3 and 4 using Ga FIB (gallium focused ion beam), which allows us to obtain sharper metallic edges of the gratings and higher resolution of the features as shown in Fig. 5.4c. In contrast to the device 1, in devices 2-4 we use the gratings with a two-fold purpose: 1) to provide enough momentum to launch the 2D polaritons and 2) to dope graphene by using them as a bottom split gate to create a graphene pn-junction as shown in Fig. 5.4b. We use devices 2-4 for the photocurrent measurements. For this type of measurements, the 2D stack area can be small (below 20 μm^2, see Fig. 5.2) since the laser power used is high (achieving values up to 10 mW and irradiance of 33.6 $mW/\mu m^2$) and we focus the light with a high NA objective, thus obtaining a good SNR.

The 4 devices are listed in Table 5.1 with their respective characteristics. We mainly vary the grating period (L is the period of the metallic rods that consists on the sum of the metallic width (w) and the gap between these rods (g)), substrate, gratings fabrication procedure (fabricated using EBL or FIB) and hBN type: natural or enriched isotope. In this thesis, we report mainly the results of device 1 and 2.

Sample	**Grating location respect to 2D stack**	**Grating fbarication**	**Grating period ($L = w + g$)**	**Substrate**	**hBN type**
Device 1	above	EBL	150 = 100 + 50 nm	SiO_2	natural
Device 2	below	EBL	100 = 50 + 50 nm	CaF_2	natural
Device 3	below	FIB	75 = 40 + 35 nm	SiO_2	iso-B10
Device 4	below	FIB	140 = 75 + 65 nm	CaF_2	iso-B10

Table 5.1: Characteristics of the fabricated devices.

Finally, we point out that after these fabrication steps, we shape graphene via a patterned etching mask with EBL. Then, we use SF_6 gas to etch the top hBN, followed by etching step for graphene using O_2 gas. As a last step we produce the 1D contact between metal and graphene, by patterning with EBL the metal electrodes overlapping with graphene as explained in previous chapters. Subsequently, we perform the same etching procedure mentioned above and followed by a thermal evaporation step of Cr/Au contacts and lift off in acetone as described in Ref. 34. We obtain graphene mobilities of these devices between 5,000 - 10,000 cm^2/Vs, extracted from the resistance curves as a function of gate voltage as shown in previous chapters.

5.3 FTIR and mid-IR/LWIR setup

For the transmission measurements of device 1 we use a commercial FTIR (fourier transform infrared) spectrometer (Bruker Tensor FTIR with a Bruker Hyperion 2000 microscope and nitrogen cooled MCT detector), which its spectral range goes from 6500 to 650 cm^{-1} (λ = 1.54 to 15.4 µm) under normal incidence in air.

The experimental mid-IR/LWIR setup used is very similar to the one described in chapter 4. The main difference relies on the laser source that for these experiments we use a pulsed QCL mid and long-wave infrared laser (MIRcat from Daylight Solutions) that its tunable wavelength ranges from 6.6 to 13.6 μm with a spectral resolution of <1 cm^{-1} and it's linearly polarized. We modulate the light via an optical chopper at 373 Hz and we measure the photocurrent using a lock-in amplifier (Stanford Research). We scan the device position with motorized xyz-stage. We focus the infrared light using a reflective objective with a NA of 0.5. To calibrate the incident power we use a thermopile detector from Thorlabs placed at the sample location.

5.4 Results and Discussion

5.4.1 FTIR transmission measurements

We perform transmission measurements using FTIR from a wavenumber range between 1200-1800 cm^{-1} ($\lambda = 8.3$ - 5.5 μm respectively). We typically normalize the transmission spectrum with a reference signal (e.g. bare substrate, in this case low doped Si/SiO_2) outside the device area (including the metallic rods with the 2D stack). However, when sweeping the Si backgate voltage during the measurements, we take the reference at the graphene area with the backgate at the CNP value (around 0 V). The spectrum resolution is about 4 cm^{-1} (correspondence of 16 nm in wavelength). We also estimate the extinction value of the measurements, which corresponds to the 1 minus the normalized transmission to the one at the graphene CNP. Following this procedure, we are able to probe the changes in the optical response of the device as a function of the charge carrier density.

Fig. 5.3d displays the extinction spectrum for several backgate voltage values, thus reaching Fermi level values of 0.3 eV. We observe several features in this spectrum. In particular, a prominent dip appears at 1435 cm^{-1} ($\lambda = 6.97$ μm) as the Fermi level increases and has negative values of extinction. Also we identify a sharp peak around 1447 cm^{-1} ($\lambda = 6.91$ μm), which increases its extinction value from 5% to 12% when increasing the Fermi level. Additionally, this peak blue shifts proportionally to the Fermi level that corresponds to a graphene plasmonic behavior. We investigate this peak by performing an optical simulation shown in Fig. 5.3b at 0.3 eV and the mentioned wavenumber (1447 cm^{-1}). We observe that the hBN hyperbolic phonon polaritons (HPPs) are launched at the edges of the metallic gratings and propagate as ray-like waves through the hBN slab. Simultaneously, in the graphene layer plane, a plasmonic wave is observed mainly below the metal width and gap region that also constructively interfere with the HPPs. This behavior corresponds to the hybridize plasmon-phonon polaritons as shown in near-field experiments via s-SNOM[28,37]. This is in agreement with the relatively small wavenumber shift (≈ 20 cm^{-1}) with the Fermi level ascribed to the phonon-like nature of this polariton.

On the other hand, we observe a peak with smaller extinction value below (5%) that appears at 0.22 eV and around 1540 cm^{-1}. This peak also blue shifts (≈ 35 cm^{-1}) for a narrower range of Fermi level (from 0.22 to 0.3 eV). We also investigate this extinction peak via optical simulation as shown in Fig. 5.3c, which depicts a graphene plasmon mode

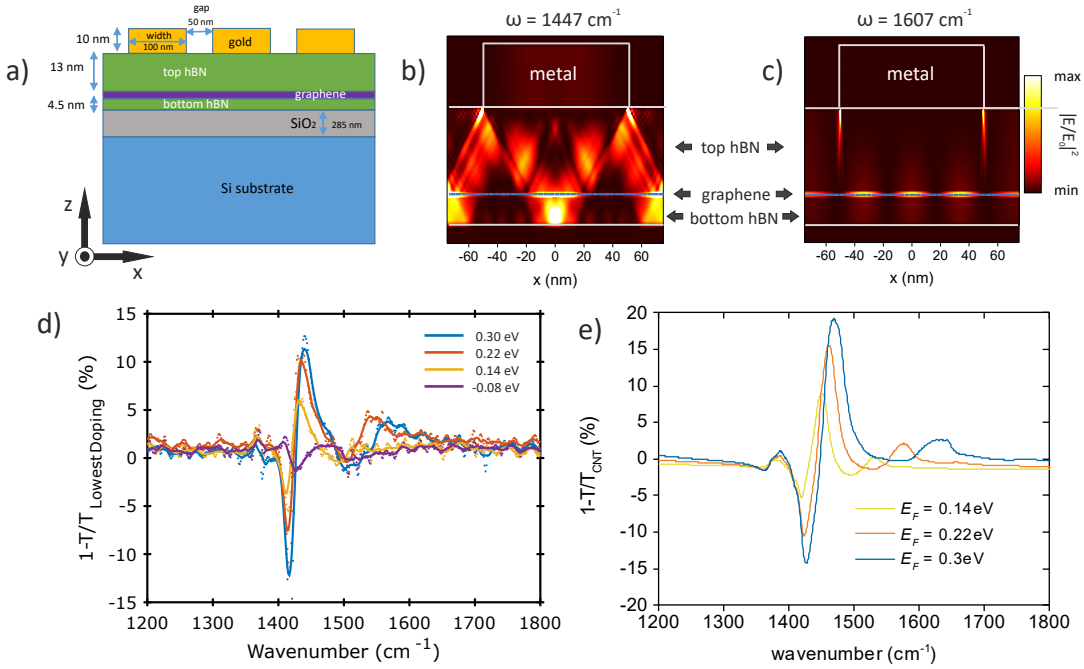

Fig. 5.3: Device 1 schematic, transmission measurements and simulations. **a)** Schematic representation (not to scale) of the device 1 cross section used for tranmission measurements. **b)** Cross section view of the simulated total electric field intensity ($|E|^2$) normalized to the incident one ($|E_0|^2$) at 1447 cm^{-1} ($\lambda = 6.91$ µm) for a graphene Fermi level of 0.3 eV. **c)** Same as **b** but at 1607 cm^{-1} ($\lambda = 6.22$ µm). **b** and **c** $y-$axis is not to scale for illustration. **d)** Extinction (1-T/T_{CNP}) spectrum of the device 1 measured by FTIR. The extinction corresponds to 1 minus the measured transmission normalized to the transmission at the graphene CNP. The traces correspond to several Fermi levels as indicated in the legend. **e)** Optical simulations based on device 1 geometry for several Fermi levels. We show excellent qualitatively and quantitatively agreement respect to the measurements shown in **d**.

at its plane. At this particular wavenumber value (1607 cm^{-1}) we don't observe a clear hybridization with the hBN HPPs since corresponds to the spectral edge of the upper RB. We point out that the former peak of the hybridized mode shows narrower linewidth and higher extinction value asscribed to the low-loss nature of this polariton [28,37] in comparison with the peak corresponding to the graphene plasmonic non-hybridized mode at 1600 cm^{-1}.

In collaboration with Elefterios Lidorikis group, we perform periodic optical simulations using finite-difference time-domain (FDTD in Lumerical software) of the structure depicted in Fig. 5.3a using a graphene mobility of 10,000 cm^2/Vs, which matches the extracted mobility of the device mentioned previously. We observe the theoretical extinction curves in Fig. 5.3e that show an excellent agreement in a qualitative and quantitative manner respect to the experimental results. The slight spectral blue shift of the peaks in the simulations respect to the experiment might be ascribed to the used hBN dielectric permittivity model (Cai et al. from ref. 28). Also, the slightly higher extinction value in the simulations are most likely due to the peak broadening as a result of inhomogeneous metal and gap width of the rods.

5.4.2 Photocurrent measurements and device responsivity

As previously explained, for the photocurrent measurements,the gratings are placed below the 2D stack and also are used as gates. These gates produce a non-uniform electrostatic profile as shown in Fig, 5.4e, where the field decays significantly outside the edges of the gates. In fact, the electrostatic potential and hence the Fermi level doesn't decay to zero for small values of the gap between the metallic rods. For instance, in the case of a period consisting of an equal size of the gap and metal width, we obtain a maximum decay of 3 times the value above the gated rod as shown in Fig. 5.4e. As we will explain later, this non-uniform gating has an important influence on the optical response of these devices.

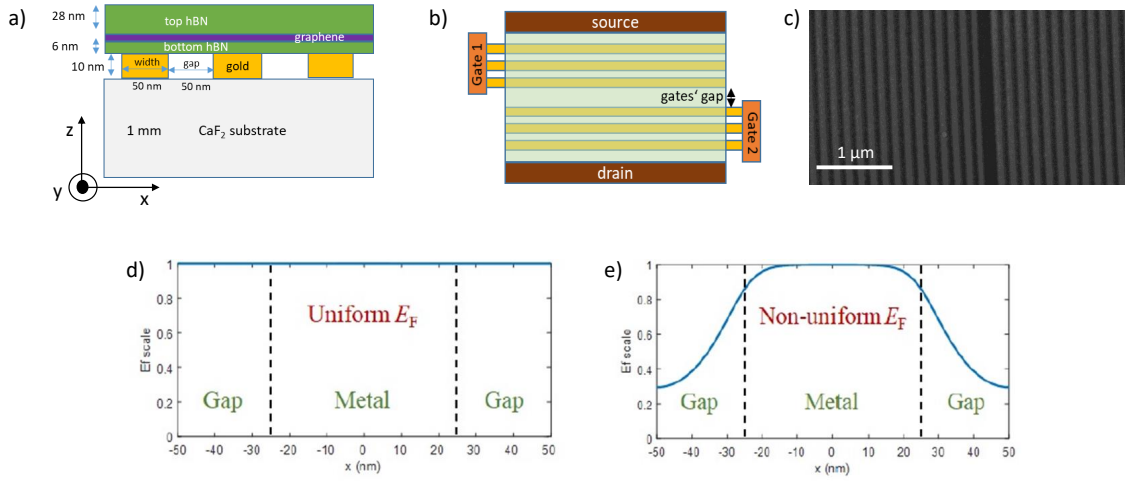

Fig. 5.4: Schematic of device 2 and electrostatic potential profile. **a)** Cross section view of device 2. This configuration is used for photocurrent measurements. **b)** Top view of device 2. The gap of the grating gates is 200 nm for this device. **c)** SEM image of the grating gates of device 4. **d)** Periodic electrostatic potential for a uniform gating device. **e)** Same as **d**, but for non-uniform electrostatic profile resembling the one of devices 2-4.

For the characterization of the photoresponse we first measure the device 2. The optical image of this device is displayed in Fig. 5.5a together with the electrical configuration using a zero-bias graphene channel. We perform a scanning photocurrent map across the device area and set the laser wavelength to 6.6 µm. We apply -0.2 V to both grating gate 1 (GG1) and grating gate 2 (GG2), which corresponds to p-type doping for both gated regions (CNP gate value is around 0 V). We observe in Fig. 5.5b that the main photocurrent contribution is from the metallic contact-graphene interface. This is attributed mainly to the Fermi level pinning of graphene in the vicinity of the contact[41,62]. It is worth mentioning that we are able to observe this contribution since the device size (24×21 µm^2) is larger than the beam spot size, which we typically achieve a beam fwhm close to the incident wavelength (e.g. 10 µm for a $\lambda = 6.6$ µm).

Then we apply to GG1 = 0.4 V (n-type doping) and to GG2 = -0.25 V (p-type doping), thus creating a graphene pn-junction. By taking the same scan map range as in Fig.

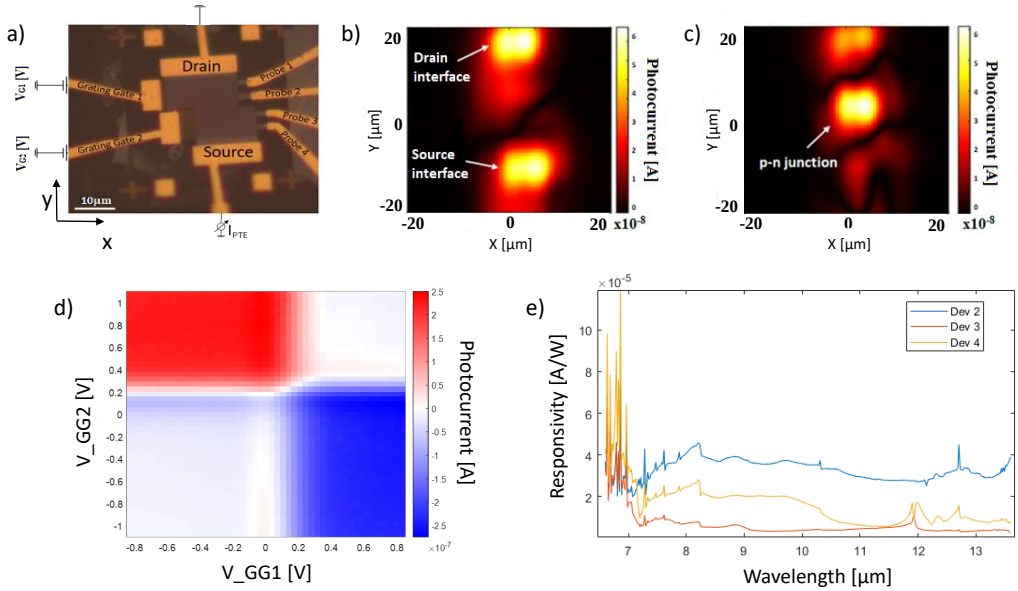

Fig. 5.5: Photocurrent measurements of device 2. **a)** Optical image of device 2. **b)** Scanning photocurrent map at 6.6 μm. The gates are set to -0.2 V that corresponds to p-type doping for both gated regions. **c)** Same as **b** but with GG1 set at 0.4 V and GG2 at -0.25 V, thus creating a pn-junction. **d)** Photocurrent map as a function of the two gate voltages at $\lambda = 8.6$ μm for device 4. **e)** Spectral responsivity of devices 2-4. The gates' voltages are set to low doped (≈ 0.1 eV) pn-junction configuration.

5.5b, we observe that in this case the photocurrent contribution is located at the graphene pn-junction interface. On the other hand, the contact contribution remains present but its magnitude is weaker than the pn-junction contribution (see Fig. 5.5c).

We locate at the pn-junction interface maximum signal with the motorized stages as explained in the previous chapters. Here, we acquire a photocurrent map as a function of the gate voltages (GG1 and GG2) that are tuned independently. This measurement allows us to identify the photocurrent mechanism and Fermi level of each junction for optimum operation. We observe that the maximum photocurrent occurs at the np or pn configuration as shown in Fig. 5.5d. Also, in this figure we notice multiple sign changes of the photocurrent, thus showing the characteristic 6-fold pattern corresponding to the photothermoelectric effect. This confirms that the PTE effect is the driven photocurrent mechanism as observed for similar devices in the previous chapters.

In Fig. 5.5e, we display the responsivity spectrum of devices 2, 3 and 4. We set the gate voltages to obtain a pn-junction configuration in the low doping regime between 0.15-0.16 eV. In general, we observe a higher photoresponse at the hBN upper ($\sim$ 6-7 μm) and lower ($\sim$ 12-13 μm) RB bands, since the HPPs concentrate the mid-IR light at the pn-junction interface as shown in chapter 4 for the upper RB case. The typical incident power ranges from $\sim$1-15 mW and an irradiance of 33.6 mW/μm^2. The three devices achieve a similar responsivity in the order of tens of μA/W. We point out that the low responsivity of these devices occurs since it doesn't exploit efficiently the photothermoelectric effect. First,

the device configuration doesn't fully concentrate the incoming beam to the graphene pn-junction as demonstrated with the approaches shown in previous chapters. Also, the device geometry is not optimum as the graphene shape corresponds to a rectangular sheet and not to an H-shaped graphene channel as shown in previous chapters as well. Despite of using this simplistic design, we accomplished a good SNR (see Fig. 5.5b-c).

5.4.3 Photocurrent spectra

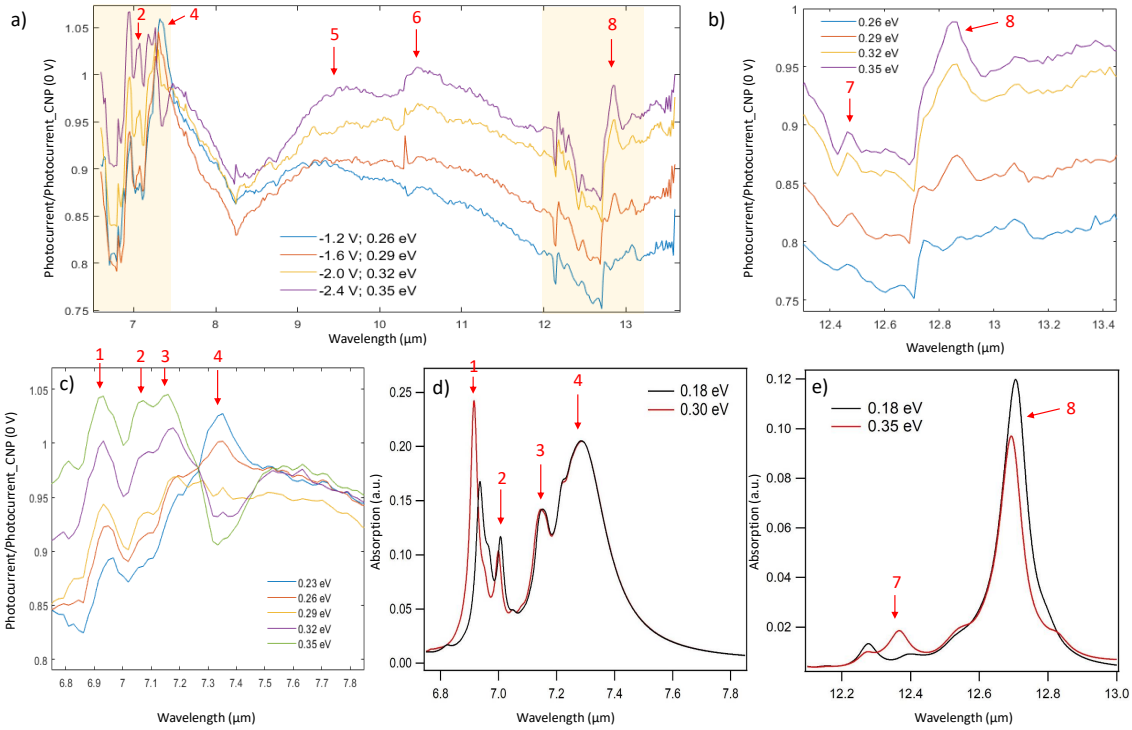

Fig. 5.6: Normalized photocurrent spectra of device 2. **a)** Normalized photocurrent spectrum at several gate voltages. The photocurrent spectra are normalized to the one at the gate at CNP. We highlight and label the polaritonic peaks with red arrows. **b)** Amplified region of **a** to highlight the lower RB spectral range. **c)** Same as **b** but for the upper RB range. **d)** Optical simulation of graphene absorption at the upper RB spectral region for different Fermi energies. We label the identified peaks in the same manner as the experimental ones. **e)** Same as **d** but for the lower RB range.

Now, we investigate the normalized photocurrent spectrum for device 2 at several gate voltages of GG2 as shown in Fig. 5.6a. Basically, the photocurrent spectra are normalized to the one taken with GG2 at the CNP in order to probe the carrier dependent optoelectronic properties. GG1 is set to a fixed gate voltage (0.4 V, n-type doping) and for this voltage, the maximum photocurrent when GG2 is swept towards negative voltages (p-type doping) as shown in Fig. 5.6a, thus forming a pn-junction configuration. We observe several peaks at different spectral regions as shown in the red arrows in Fig. 5.6a. We highlight in yellow two specific regions such as the upper (≈ 6-7 μm) and lower (≈ 12-13

μm) RBs, where we observe several peaks that evolves with Fermi level (up to 0.35 eV). This is ascribed to the hybridized plasmon-phonon polaritons. These peaks associated to polaritonic resonances are highlighted and labeled with red arrows.

Moreover, two additional broad peaks (labeled as 5 and 6) appear at higher Fermi levels outside the RBs, around 9.5 and 10.35 μm respectively. These peaks are potential graphene acoustic plasmons[31,32,128,129] since are separated with the metal rods by 5 nm of hBN. Regarding the evolution of these peaks as a function of the Fermi level, we observe that the normalized photocurrent in general increases in the spectral region between 9.2 to 12 μm proportionally to the Fermi level as shown in Fig. 5.6a. In particular, for the peak 5 we notice a broader peak at 0.32 eV that raises compared to the signal base level with its maximum located around 10 μm and shifts to 9.5 μm for a Fermi level of 0.35 eV. In the case of peak 6, we notice a peak emerging from the base line signal from 0.32 eV centered at 10.5 μm and shifts at 0.35 eV to 10.35 μm (considering the pronounced peak shoulder). We point out that the spike at 10.3 μm for 0.29-0.32 eV is due to a normalization artefact. It is worth to mention that the blue shift of these peaks are more pronounced to the ones at the RBs (hybridized modes).

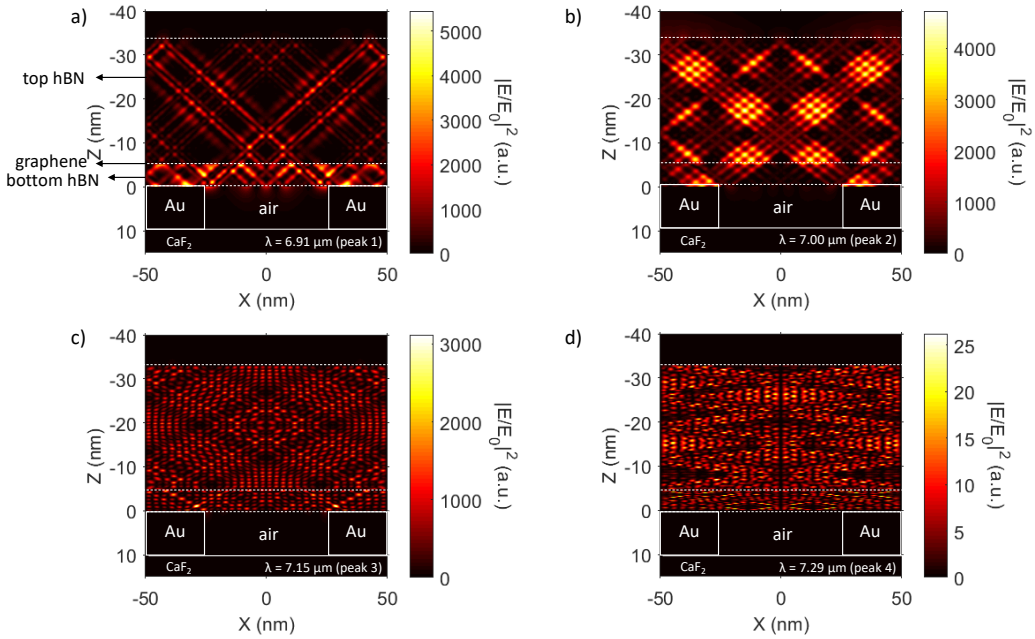

Fig. 5.7: Optical simulations at the upper RB range. Cross section view of the electric field intensity normalized to the incident one. The Z direction (y-axis in graphs) and X direction (x-axis in the graphs) are defined in Fig. 5.4a. The calculations correspond to a uniform graphene Fermi level at 0.3 eV for the following wavelengths: **a)** 6.91 μm (corresponding to peak 1 in Fig. 5.6), **b)** 7.0 μm (corresponding to peak 2 in Fig. 5.6), **c)** 7.15 μm (corresponding to peak 3) and **d)** 7.29 μm (corresponding to peak 4). The dashed lines in all panels indicate the correspondent 2D material (as shown in panel **a**) and the squares the metallic rods regions (labeled as Au). Due to the periodicity of the simulations, the metal width splits by half at the edges of the simulation unit cell.

We investigate in more details the peaks observed in the RBs. First, for the case of the lower RB range as shown in Fig. 5.6b, we observe two main peaks around 12.5 (peak labeled as 7) and 12.85 µm (peak labeled as 8). These peaks show an increase in the amplitude at higher Fermi levels, as well as a small blue shift for both peaks 7 and 8. For the case of the 8th peak from 12.88 µm (776 cm^{-1}) to 12.83 µm (779 cm^{-1}), whereas the 7th peak shifts from 12.48 µm (801.3 cm^{-1}) to 12.46 µm (802.6 cm^{-1}). For the case of the upper RB range shown in Fig. 5.6c, we identify several peaks (1-4) marked with the red arrows. In general, all the peaks increases the amplitude with the increase of the Fermi level. In particular, for peak 1 we observe a more pronounced blue shift with the Fermi level, which goes from 6.96 µm (1437 cm^{-1}) from to 6.91 µm (1447 cm^{-1}). The 4th peak corresponds to the TO phonon of hBN, which seems to have a pronounced contribution at low Fermi level values but reduces its effect at high doping.

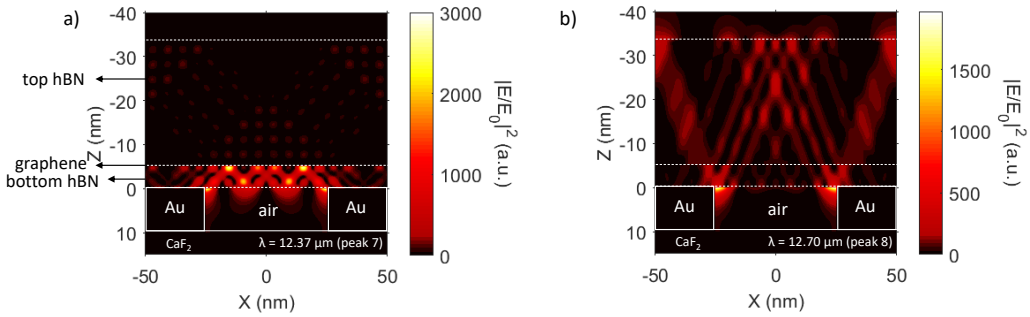

Fig. 5.8: Optical simulations at the lower RB range. Cross section view of the electric field intensity normalized to the incident one. The Z direction (y-axis in graphs) and X direction (x-axis in the graphs) are defined in Fig. 5.4a. The calculations correspond to a uniform graphene Fermi level at 0.3 eV for the following wavelengths: **a)** 12.37 µm (corresponding to peak 7 in Fig. 5.6) and **b)** 12.70 µm (corresponding to peak 8 in Fig. 5.6). The dashed lines in all panels indicate the correspondent 2D material as indicated with black arrows and the squares the metallic rods regions (labeled as Au). Due to the periodicity of the simulations, the metal width splits by half at the edges of the simulation unit cell.

Fig. 5.6d-e depicts optical simulations performed using semi-analytical coupled-wave analysis (RCWA) in collaboration with the group of Nuno Peres from University of Minho. In Fig. 5.6d we observe similar peaks as labelled in the experimental plot with the red arrows (5.6c) and also shows that peak 1 blue shifts more pronounced respect to the other ones, which demonstrates excellent agreement between the theory and measurements. In a similar fashion, Fig. 5.6e exhibits the two peaks present in the experimental results at similar spectral position.

We analyze these labeled peaks in more details by investigating theoretically the electric field intensity of these polaritonic resonances. The electric field intensity associated to peak 1 (labeled in Fig. 5.6c) is shown in Fig. 5.7a. We notice two horizontal nodes in the field located at the upper edge of the top hBN nearby x=0 and x=50 nm (or x=-50 nm), which confirms that this mode is produced by the first diffraction order. The angle of propagation of such modes inside the upper hBN layer is such that on one period of the structure, a ray can travel from the top hBN's upper edge towards the graphene layer, be partially reflected and then travel backwards the upper edge of top hBN layer. When inter-

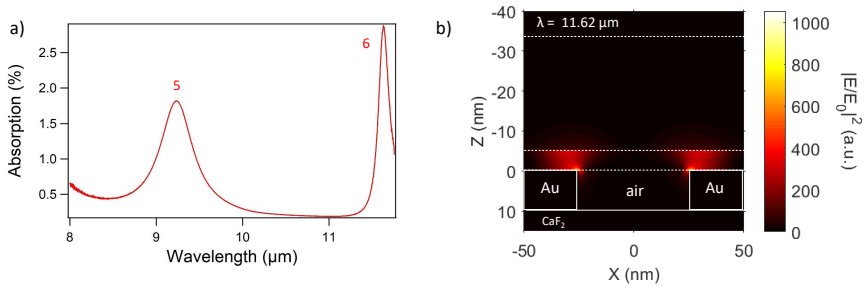

Fig. 5.9: Optical simulations of graphene plasmons. **a)** Absorption spectrum outside the RBs range. The graphene doping is 0.35 eV. **b)** Cross section view of the electric field intensity normalized to the incident one at $\lambda = 11.62$ μm. The Z direction (y-axis in graphs) and X direction (x-axis in the graphs) are defined in Fig. 5.4a. The calculations correspond to a uniform graphene Fermi level at 0.35 eV. The dashed lines in all panels indicate the correspondent 2D material (as shown in Fig. 5.7a) and the squares the metallic rods regions (labeled as Au). Due to the periodicity of the simulations, the metal width splits by half at the edges of the simulation unit cell.

acting with the graphene, part of the ray intensity penetrates into the bottom hBN layer, producing the wave with high field intensity, confined inside the lower hBN layer between the graphene and metallic grating. Fig. 5.7b shows the spatial distribution of the field, which corresponds to peak 2 in Fig. 5.6c. The spatial distribution of field is characterized by presence of 4 nodes on one period in the horizontal direction (which indicated that this mode corresponds to the second diffraction order). The angle of propagation of this mode is similar to the previous case: on one period of the structure the mode ray travels from the upper edge of the top hBN layer towards the graphene, partially reflects from it and returns towards the top hBN layer's upper edge. Fig. 5.7c shows the spatial distribution of the field intensity, corresponding to peak 3 in Fig. 5.6c. The presence of the two nodes (located at x=0 and x=50 nm) on one period of the structure demonstrates, that this mode correspond to the first diffraction order. The angle of propagation is different respect to the previous cases since on one period the ray travels from one side of the top hBN and returns to its initial position in another period. Finally, in Fig. 5.7d we observe that the spatial field intensity distribution corresponds to a bunching of modes. Thus, in the vicinity of hBN TO phonon resonance an infinite number of modes are excited, so that the field is the mixture of different modes.

In the case of the lower RB, we observe in Fig. 5.8a the electric field intensity corresponding to the peak 7 defined in Fig. 5.6b. We notice that the scenario is similar to that of peak 1 (see Fig. 5.7a): on one period ray-like mode travels from upper edge of top hBN layer, then partially reflects from graphene layer and return back to the upper edge of hBN. At the same time, the radiation, partially transmitted through the graphene, excites the mode in the bottom hBN, which field is concentrated mainly above the gap in the periodic structure. In Fig. 5.8b shows the spatial distribution of the field, corresponding to peak 8 in Fig. 5.6b. We observe that the propagation of the waves occurs in a different scenario: during the half-period of the structure, the wave travels from the upper edge of top hBN layer, reflects from the corner of metallic rod, and returns to the hBN upper edge (and the same on other half-period).

Now, we compare the peaks observed outside the RBs (see Fig 5.6a) with the results of the optical simulations as shown in Fig. 5.9a. We notice that the peak 5 located at 9.3 µm shows spectral position agreement with the experiment (located around 9.4 µm in Fig. 5.6a), however the peak at 11.6 µm (peak 6) is slightly red shifted respect to the one experimentally measured (located at 10.35 µm). It is worth to mention that the linewidth of the experimental peaks are significantly broader compared to the simulated ones. This might be ascribed to the non-uniform doping produced by the grating gates, which requires further studies. Fig. 5.9b shows the electric field intensity spatial distribution of graphene plasmon-polariton mode at 11.6 µm (peak 6). As it can be seen, the electromagnetic field is mainly concentrated between the graphene and metal, which is characteristic of an acoustic mode.[31,32,129] Peaks 6 and 5 correspond to the first and second diffraction orders, respectively. We also find the amplitude of the absorbance of the peak at 11.6 µm is larger compared to the other peak (peak 5) as the effectiveness of excitation of the second diffraction order is in general less, if compared to the effectiveness of first order excitation, which also is in agreement with both experiment and theory.

5.4.4 Dispersion relation of the 2D polaritons

We calculate the dispersion relation of the polaritonic modes present in the device using the transfer matrix method (TMM) in collaboration with the group of Nuno Peres from University of Minho. The dispersion of the plasmon phonon polariton modes in the upper and lower RB are shown in Fig. 5.10a-b, where the different colored lines represent the several order modes of these polaritons (ranging from the 1st to 5th modes). The order number is given by the number of nodes present in the polaritonic field. We point out the characteristic dispersion of the HPPs behaving as collective modes present at several wavelength values as shown in Fig. 5.10a-b.

Then, by considering the in-plane momentum conservation principle, the momentum provided by the light diffraction at the metallic rod array is given as following: $k_n = k_{in} + nK = \frac{2\pi}{\lambda} sin(\theta_{in}) + n\frac{2\pi}{L}$, where θ_{in} is the incident angle, λ is the incident wavelength, n is the diffraction order, L is the period of the metallic rods that consists on the sum of the metallic width (w) and the gap between these rods (g). Due to the fact that we work under normal incidence, the in-plane momentum will be given by the period of the metal grating ($K = n2\pi/L = n2\pi/(w+g)$). By taking into account the period of device 2 ($L =$ 100 nm, $w =$ 50 nm and $g =$ 50 nm), we determine the momentum given for the first ($K = 63$ μm^{-1}) and second ($K = 127$ μm^{-1}) diffraction order values respectively that are plotted as horizontal red dashed lines in Figs. 5.10a-b.

In Fig. 5.10a the modes corresponding to the peaks observed experimentally in Fig. 5.6c are plotted in red filled circles, where peak 1 and 3 correspond to the first diffraction order resonance produced by the metal rods, hence crossing the first horizontal red dashed line (this is confirmed by 2 nodes per period in Figs. 5.7a and 5.7c). Then for the case of the 2nd peak, we find that corresponds to a second diffraction order resonance (due to the four nodes per period observed in Fig. 5.7b) with a slight red shift compared to the estimated value (represented in open red circle), thus showing excellent agreement with the experimental results. In the same fashion, at the lower RB range in Fig. 5.10b we observe the excitation of the first diffraction order resonance, namely the peak located experimentally at 12.83 μm (peak 8) in Fig. 5.6b as well as a second order resonance the smaller peak at 12.46 μm (peak 7). We notice a slight red shift that is equal for both peaks of about 0.15 μm compared to the theoretical values represented in red open circles.

We also investigate the wavelengths of these polaritonic peaks as a function of graphene Fermi level as shown in Fig. 5.10c-d. We observe a very small blue shift in all the modes for the upper RB, except for the case of the peak 1 located around 6.9 μm in Fig. 5.10c. This fact is also confirmed by the experimental data (see Fig. 5.6c), where the shift of peak 1 is also more pronounced thus demonstrating its high degree of hybridization with graphene plasmons. For the case of the lower RB (Fig. 5.10d), the blue shift is considerably small as observed in the experiment for the 7th and 8th peaks. For instance, this latter peak located around 12.8 μm shows a blue shift of 50 nm in wavelength or 3 cm^{-1} in wavenumber as shown in Fig. 5.6b. The small shift for the hybridized modes is a result of the narrow RBs region that compressed spectrally these polaritons and the higher phononic contribution compared to the plasmonic one as seen in the electric field profile. Also as the hybridized polariton energy moves closer to the TO phonons of hBN, these polaritons become very

lossy due to the substrate absorption and these modes can't propogate anymore as shown in ref. 130,131.

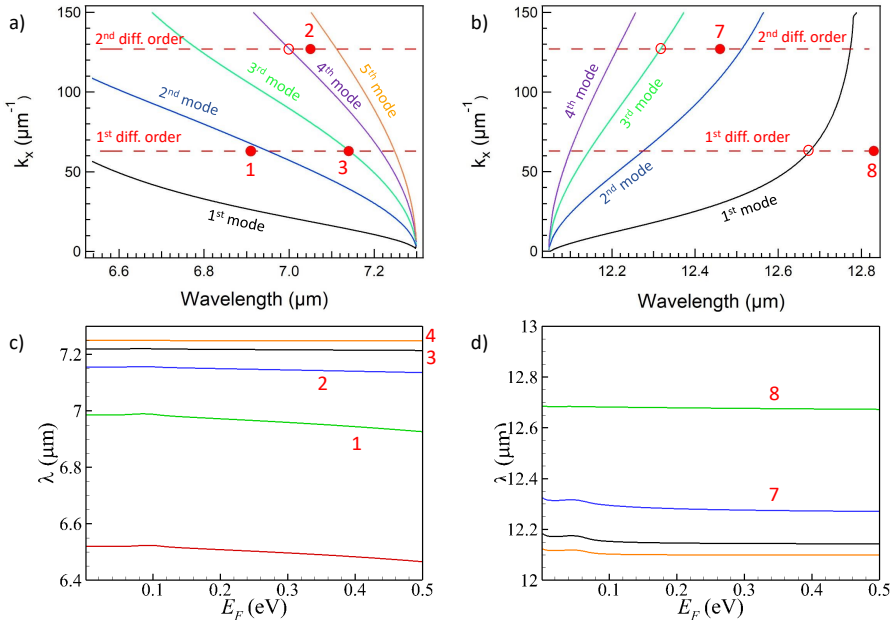

Fig. 5.10: Dispersion relation of the 2D polaritons at RBs. **a)** Dispersion relation of the hybridized plasmon phonon polariton modes at the upper RB. The two horizontal dashed lines correspond to the first and second diffraction order resonances launched by the metal rod array. The marked red dots represent the experimental values, which the numeric labels are defined in Fig. 5.6. The graphene Fermi level is 0.35 eV. **b)** Same as **a** but at the lower RB spectral range. **c)** Eigenfrequency (wavelength) of each polaritonic mode at the upper RB as a function of the graphene Fermi level. **d)** Same as **c** but at the range of the lower RB.

5.4.5 Tunability of the 2D polaritonic nanoresonators

Furthermore, we investigate theoretically the tunability of the excited 2D polaritons by varying the bottom (Fig. 5.11a) or top (Fig. 5.11b) hBN slab thickness or metal grating period (Fig. 5.11c-d). The bottom and top hBN layers form a whole slab, where the hybridized polaritons propagate and bounce at the boundaries of the layers. As a result, in Fig. 5.11a we notice that when increasing the top hBN thickness, the peaks of the polaritonic modes mostly blue shift (contrary to a Fabry-Pérot like resonator) and conserve their absorption amplitude. In particular a prominent shift is observed for the peaks 1 and 2 as labeled also in Fig. 5.6c. In addition, we observe an additional peak (labeled as 5' in Fig. 5.11a) for the thicker case of the top hBN. The peaks 1 and 2 vary in amplitude and spectral position when the bottom hBN layer thickness is changed and even appears an additional peak for the thicker bottom hBN (8 nm). The peak 3 remains at the same spectral position for the different cases.

When varying the period of the metallic rods as shown in Fig. 5.11c, we observe a sim-

ilar trend as when changing the top hBN thickness (see Fig. 5.11a). Mainly, we observe a red shift of the peaks 1-3 and a weak variation of the peak amplitude. However, we don't observe any appearance of additional peaks as in the former cases. In contrast, for the lower RB range (Fig 5.11d) we notice that when increasing the periodicity of the metallic rods, the polaritonic peaks blue shift and the absorption amplitude is increased.

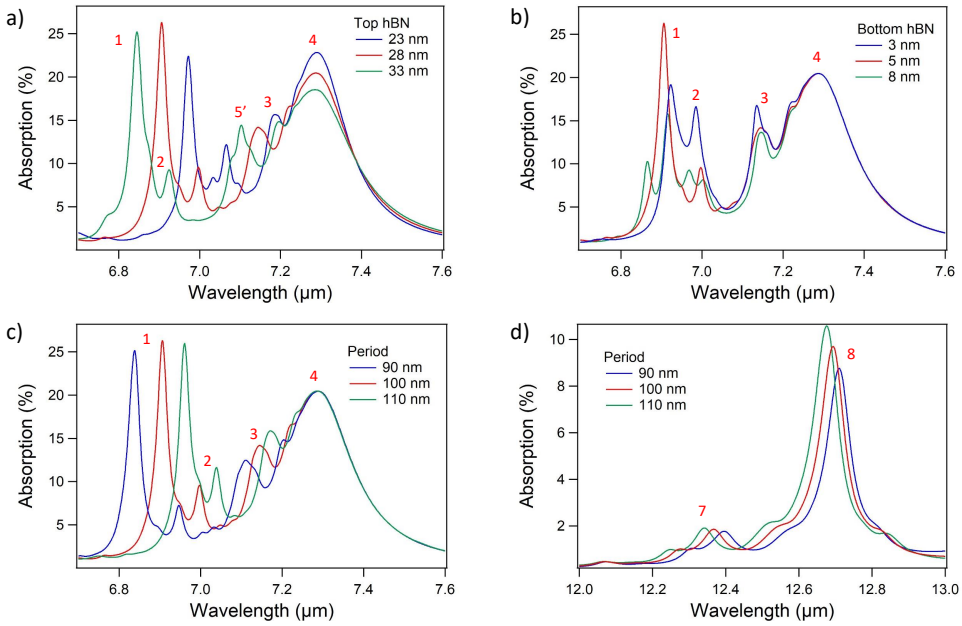

Fig. 5.11: Tunability of the polaritonic cavity. **a)** Absorption spectrum of the upper RB spectral range for several top hBN thicknesses. The graphene Fermi level is 0.35 eV. **b)** Same as **a** but changing the bottom hBN thickness and keeping constant the total thickness of the hBN slab (bottom and top layers). **c)** Same as **a** but keeping at a fixed value of the bottom hBN to 5 nm and top hBN to 28 nm. It shows several traces for different values of the period of the metallic rods. **d)** Same as **c** but at the range of the lower RB.

5.4.6 Power dependence of the photoresponse

We measure the photocurrent as a function of the incident power of the mid-IR light. We are able to attenuate the laser power for several orders of magnitude, hence reaching the microwatts regime. We focus on the wavelengths that we find the polaritonic peaks shown above. In addition to this, we perform this measurement for several gate values in order to observe any influence on the graphene doping related to the polaritonic behavior. Basically, we fix the GG1 to 0.5 V (n-type doping) and sweep the GG2 towards negative voltage values (p-type doping), thus creating a pn-junction as done for the other measurements. We fit the data according to a power law $I_{PTE} \propto P^{\gamma}$ as shown in filled lines in Fig. 5.12a-d, where I_{PTE} is the photocurrent and P the incident laser power. We obtain a value of γ ranging from 0.85-0.95, thus showing a rather linear behavior of the photoresponse that for all the wavelengths for several orders of magnitude of incident power (up to 4 orders at $\lambda = 9.35$ μm). Regarding the effect of the doping variation, we didn't observe a

significant difference between the γ values at the CNP and 0.35 eV. These results indicate that the device is operating in the weak heating regime, where the change in temperature of the electronic system (ΔT) is significantly smaller than the ambient temperature ($T_{ambient}$)[23,45,100]. This is in agreement with the optical simulations that show relatively low absorption percentage of graphene (around 10% of the incident light), which experimentally is even smaller by considering that mainly the absorption taking place at the pn-junction interface contributes to the photocurrent generation.

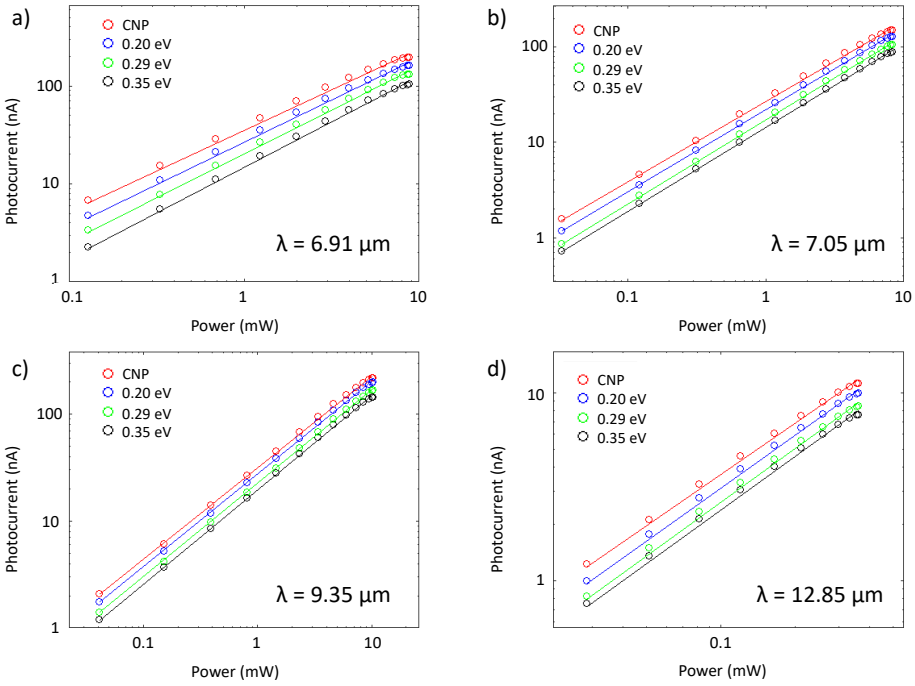

Fig. 5.12: Power dependence of the photoresponse. Photocurrent as a function of the incident power for several wavelengths: **a)** at 6.91 μm, **b)** at 7.05 μm, **c)** at 9.35 μm and **d)** at 12.85 μm. For all the cases we plot for different gate voltages of GG2 that 0 V corresponds to the CNP and -2.4 V to a graphene Fermi level of 0.35 eV. GG1 remains fixed at 0.5 V. The opened circles represent to the experimental points and the lines to the fit.

5.5 Conclusions

To summarize, we have shown mid and long-wave infrared photocurrent spectroscopy via electrical detection of graphene plasmons, hyperbolic phonon-polaritons and their hybridized modes. We also probed these high quality polaritons via optical transmission measurements. We have demonstrated the wide tunability of these nanoresonators by changing several parameters, such as hBN thickness, grating period, substrate and graphene Fermi energy. Thus, this approach enables a suitable platform for spectrally selective detection in this range and has the potential to constitute high accuracy thermal imaging, compact spectrometers, gas sensors, etc.

6 Electrical detection of molecular vibrations coupled to hyperbolic phonon polaritons

6.1 Introduction

The identification of molecular vibrations is at the heart of many infrared applications such as molecular spectroscopy,[5,6,127] infrared thermography,[2] moisture detection for fire safety,[2,8,11] space exploration,[2] etc. These vibrational modes' resonances correspond to e.g. stretching vibrations of chemical bonds, which represent their spectral fingerprints and occur at this particular infrared range of the spectrum extending even up to the THz range.[132,133] At these frequencies the absorption cross section of molecules and thin layers is considerably small, which makes the identification of them even more challenging.[4]

In previous studies, hBN hyperbolic phonon polaritons were coupled to vibrational modes of molecules, even reaching the vibrational strong coupling regime.[4,134] These polaritons, besides showing huge field confinement and long lifetimes, are spectrally located at the mid and long-wave IR range coinciding with these molecular vibrational resonances. A first experiment was conducted using hBN nanoribbons that constituted high Q-factor nanoresonators, where on top of these VdW crystals was deposited thin layers of 4,4'-bis(*N*-carbazolyl)-1,1'-biphenyl (CBP) molecules.[4] FTIR (fourier transform infrared) transmission measurements were measured to obtain the spectra (see Fig.6.1) of the nanoribbons array without and with several CBP layer thicknesses. When the CBP thickness increases, a more pronounced red shift occurs of the HPP resonance. We notice that the vibrational feature affects the lineshape of the HPP resonance starting from 3 nm thick CBP layer, which becomes more prominent at 10 nm layer thick. These effects are supported with the optical simulations as shown in Fig. 6.1b.

In the near-field experiment they performed real-space nanoimaging of these hybrid modes (HPPs with molecular vibrations).[134] They observed a clear anticrossing of the phonon polaritons' dispersion (Fig. 6.2c) by showing a distortion (significant decrease in signal amplitude) in the experimentally dispersion curves of the hBN HPPs at the frequencies of the CBP vibrational resonances (Fig. 6.2b). Also, we notice an evident loss in the propagation length (i.e. from 2 to 0.5 μm at 1510 cm^{-1} as shown in Fig. 6.2d-e) of the polaritons at the vibrational modes' frequencies of the CBP molecules (see Fig. 6.2b). On the contrary, in Fig. 6.2f-h we notice an unperturbed dispersion and propagation length of the HPPs. In this work, unstructured layers of hBN were used to avoid any additional losses from sample deterioration, such as inhomogeneities and scattering caused by nanopatterning process, in contrast to the previously mentioned far-field experiment.[4]

Even though these two main experiments described above were performed to investigate spectroscopically this vibrational strong coupling with far-field and near-field interferometry at the mid-infrared range, the electrical detection of this light-matter interaction has remained unexplored. It is worth mentioning that these experiments required an external detector (MCT) for the identification of this coupling. Moreover, the near-field experiment required a sophisticated equipment vibration free and even the molecules needed to be below the hBN flakes since the scanning tip removed these molecular layers. The far-field experiment on the other hand, required large area array (20×20 μm^2) to obtain a decent signal in the optical detector, which avoids miniaturizing the sensitive area. These above mentioned reasons prevent the development of an on-chip platform for non-destructive and label free ultrasensitive molecular spectroscopy.

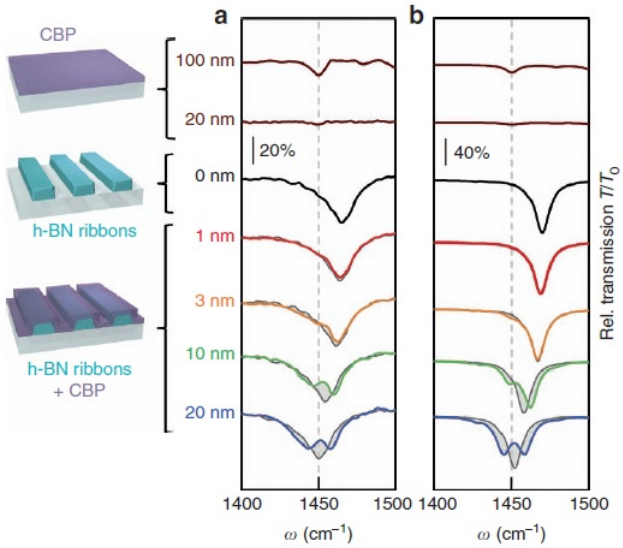

Fig. 6.1: Infrared transmission spectra of hBN nanoribbons as a function of the CBP layer thickness. **a)** Experimental transmission spectra of the hBN nanoribbons. The black curve represents the spectrum of bare hBN nanoribbons. For illustration, this curve is also shown in gray curves shifted in frequency (ω) as a background in the spectra of the nanoribbons coated with CBP. From the red to blue curves depict the spectra of the hBN nanoribbons coated with different CBP thickness. The brown curves in the upper area of the figure show the spectra of two CBP thicknesses (100 and 20 nm) on the bare substrate. The nanoribbon array area is 20×20 μm^2 with a period of 400 nm and ribbon with of 158 nm. **b)** Theoretical transmission spectra with the same color notation as in **a**. The nanoribbon period is 400 nm and ribbon width of 167 nm. Figure adapted from ref. 4

The photodetection mechanism of our novel sensing platform is based on the PTE effect as described in previous chapters 3-5, where the pn-junction is created by the split gate that simultaneously launches the hBN HPPs that are guided and constructively interfered at this junction (see Fig. 6.3a and 6.4c). Graphene will absorb these ray-like polaritons and produce hot carriers that will drive a temperature gradient across the graphene channel and hence a photovoltage. Since the hBN HPPs field penetrate the CBP molecules and the vibrational modes of them oscillate in the upper RB, there will be a strong light matter interaction between these resonances that takes place in the vicinity of graphene. Thus, graphene will act as a sensor of this strong interactions and will affect its absorption and thereby its photocurrent signal. As a result, we will electrically detect these molecular vibrational modes interactions with hBN HPPs.

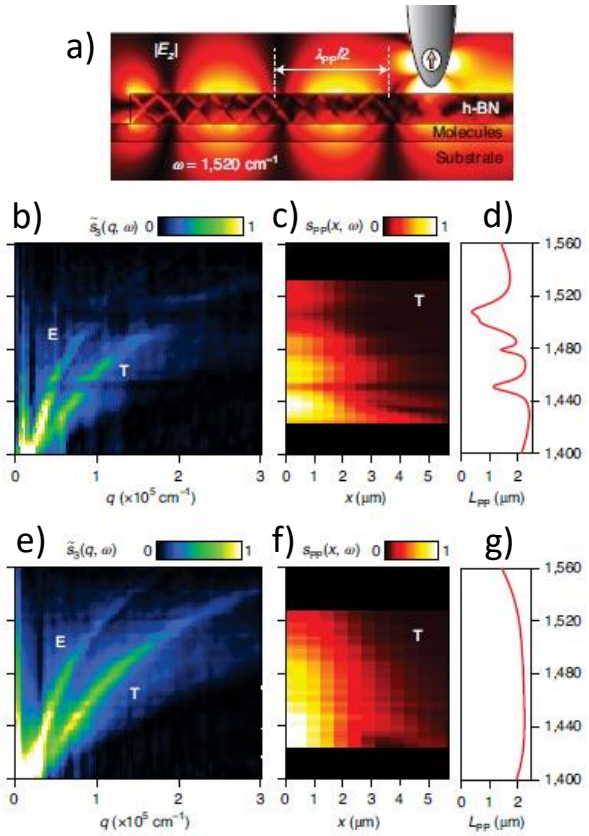

Fig. 6.2: Near-field (nano-FTIR) experiment of hBN HPPs coupled to molecular vibrations. **a)** Simulated cross section of the electric field (z-component). The field outside the hBN layer corresponds to the fundamental mode. The zigzag pattern inside the hBN layer on other hand, corresponds to higher order modes. **b)** Dielectric function (imaginary part) of the CBP molecules. **c)** and **f)** Fourier transform of the nano-FTIR amplitude signal along the scanning direction of the tip. The fundamental mode excited by the flake edge (labeled as E) or tip (labeled as T). **d)** and **g)** Isolated tip scattered field of the fundamental mode. **e)** and **h)** Theoretical propagation length of the mentioned mode. In Figs. **a-e** the hBN and CBP thicknesses are 50 and 40 nm respectively on top of a 150 nm SiO_2 on Si. Figs. **f-h** the hBN thickness is 50 nm on top of a 150 nm SiO_2 on Si. Figure adapted from ref. 134

6.2 Device fabrication and working principle

We have fabricated two devices with very similar characteristics that are resumed in Table 6.1. The first step is to pattern and evaporate the local gates that are shown in Fig. 6.3a. These sharp edges around the gap of the gates will launch efficiently the hBN HPPs as shown in Fig. 6.4c and as previously discussed in Chapter 4. Later, we perform a 2D heterostructure assembly with thin hBN layers encapsulating graphene. This 2D stack we drop on top of the local gates following the procedure described in Chapter 2. Subsequently, we shape graphene by using EBL for patterning a PMMA etching mask. We use SF_6 gas to selectively etch the top hBN, avoiding thus to reach the local gate level that can cause an electrical leak. This is followed by an etching step for graphene using O_2 gas. Finally, we pattern the 1D contact between metal and graphene using EBL and perform the same etching procedure mentioned above. We evaporate thermally the Cr/Au contacts and lift off in acetone as described in previous Chapters and in ref. 34. The overview of the fabricated devices is depicted in Fig. 6.3b,c.

At the end of the fabrication, we perform a so called brooming step, which consists on removing the lithographic residues (e.g. PMMA residues) using an AFM tip in contact mode. By applying the force on the tip sufficiently enough to remove the residues and push them to the end of the scan region (in this case towards the contacts as shown in Fig. 6.3c marked in red arrows), we clear the active area of the detector that is located at the pn-junction interface (around the gap of the gates). This procedure guarantee that the evaporated molecules will be as close as possible to the top hBN and graphene to ensure the light-matter interaction.

Regarding the evaporation of the molecular layers of 4,4'-bis(*N*-carbazolyl)-1,1'-biphenyl (CBP) with sublimated quality (99.9% from Sigma-Aldrich), it is done via thermal evaporation in an ultra-high-vacuum evaporator chamber (base pressure of $<10^{-9}$ mbar) at a rate of 0.1 nm/s using a Knudsen cell. We select the CBP molecules due to their vibrational modes spectrally located within the hBN reststrahlen band.

The 2 devices are listed in Table 6.1 with their respective characteristics such as hBN thicknesses and SD distance. In this chapter, we report mainly the results of device 1 that we evaporate the CBP molecules on top of it. For device 2 we report mainly the photocurrent characterization as shown in Fig. 6.6a-b.

Sample	Top hBN thickness (nm)	Bottom hBN thickness (nm)	Source-drain distance (µm)	Substrate
Device 1	3	4.5	3.4	SiO_2
Device 2	3.8	10.5	3.4	SiO_2

Table 6.1: Characteristics of the fabricated devices.

We perform optical simulations of the device in COMSOL in collaboration with Luis Martín-Moreno group from University of Zaragoza. In Fig. 6.4a we show the simulated graphene absorption normalized to its maximum value, which is around 1405 cm^{-1} in the upper RB for the case of 10 nm thick CBP layer on top of the device and the one with-

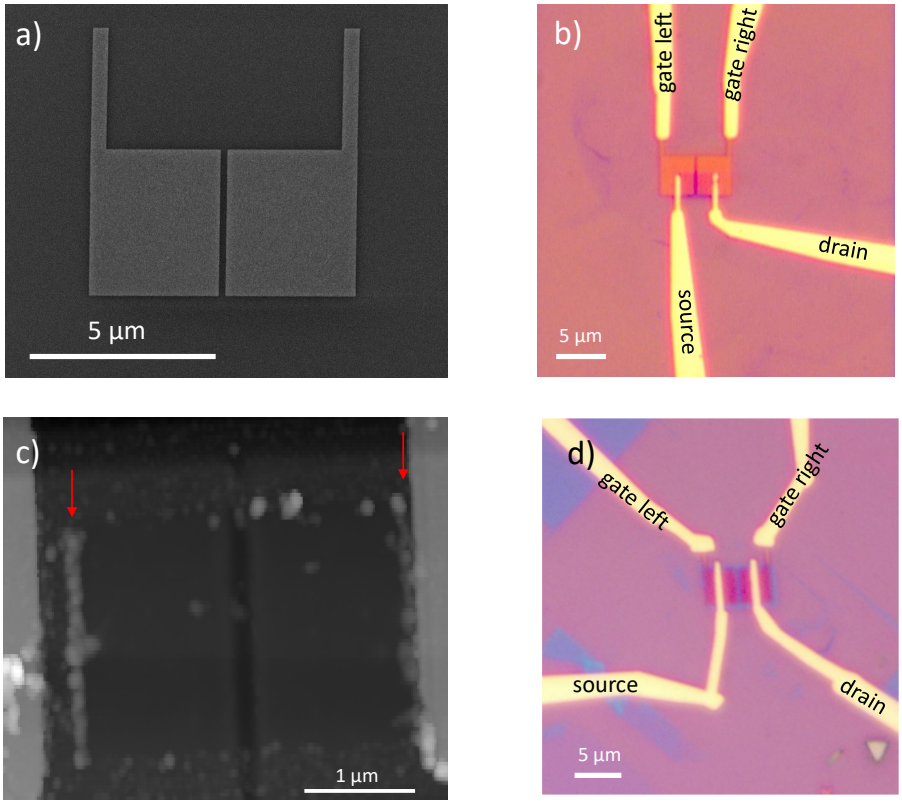

Fig. 6.3: Devices outlook. a) SEM picture of the fabricated local gates. **b)** and **d)** depict the optical figures of device 1 and 2. **c)** AFM scan of device 1 after brooming its surface. The red arrows indicate the broomed lithographic residues that agglomerates near the metallic electrodes by this AFM tip assisted process.

out CBP. The absorption is calculated at the graphene plane and we consider the whole photodetector structure (gates, contacts, hBN layers, etc.). We observe a decrease in the graphene absorption due to the presence of the CBP 10 nm layer at its vibrational modes frequencies (see Fig. 6.4b, which has the same frequency scale as Fig. 6.4a) that will be explained in section 6.3.2. The vertical dashed lines correspond to the frequencies that the electric field cross sections are shown.

For the first case at 1405 cm^{-1}, we observe the hBN HPPs being launched at the edges of the gates that propagate across the hBN slab and also the field penetrates the CBP layer as depicted in Fig. 6.4c. In contrast, for the electric field cross section at 1448 cm^{-1} shown in Fig. 6.4d corresponding to one of the vibrational modes of the CBP, we notice that the propagating behavior of the HPP is not longer observed but rather a strong field concentration in both CBP and hBN slab near the gap of the gates. Moreover, there are two additional peaks outside the upper RB of hBN observed in the absorption spectrum at 1300 and 1712 cm^{-1}. The former one corresponds to the absorption enhancement produced by the SiO_2 phonon polariton as described in chapter 4. The electric field cross section of the latter one at 1712 cm^{-1} is depicted in 6.4e, which is ascribed to the metallic

gates that show the antenna resonance at this wavenumber.

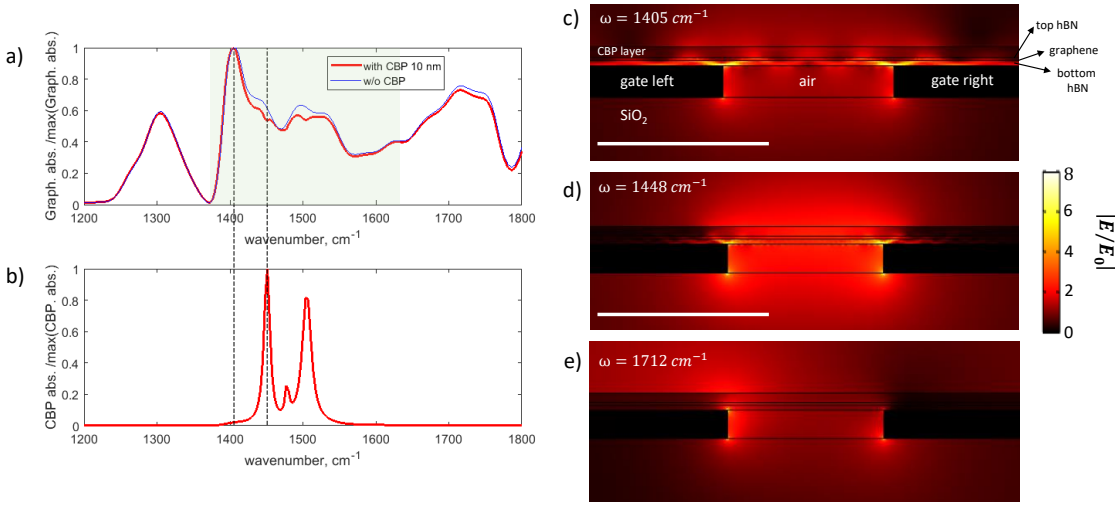

Fig. 6.4: Optical simulations of the device structure. **a)** Graphene absorption spectrum normalized to its maximum value for the cases with 10 nm thick CBP molecules (red curve) and without them (blue curve). The absorption is calculated at the graphene plane and including the whole photodetector structure (gates, contacts, hBN, etc.). The hBN upper RB is highlighted in light green. **b)** CBP absorption spectrum normalized to its maximum value. The dashed vertical lines correspond to the selected frequencies (ω) for the electric field (normalized to the incident field) profiles depicted in **c)** at 1405 cm^{-}1 (7.1 µm), **d)** at 1448 cm^{-1} (6.9 µm) and **e)** at 1712 cm^{-1} (5.8 µm). The white scale bar corresponds to 200 nm. Both graphs share the colorbar.

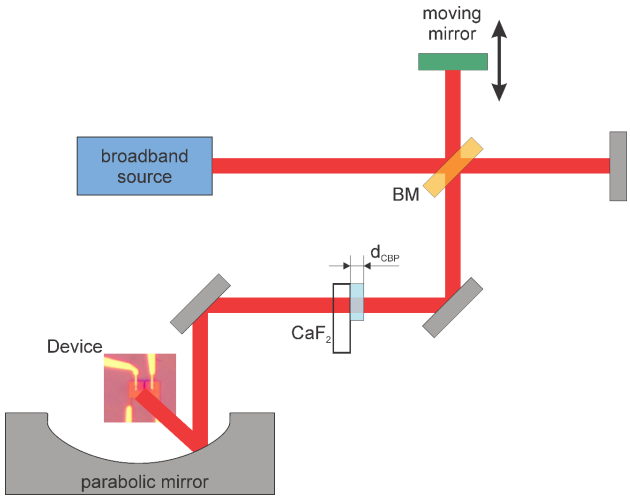

Fig. 6.5: Schematic of the FTIR setup. In this case, we show the configuration of the transmission measurements performed using the CBP molecules deposited on the CaF_2 window and as the detector we use device 1 instead of a commercial MCT. The mid-IR light is focused using a parabolic mirror.

6.3 mid-IR/LWIR and FTIR setup

For device 1 we use the nano-FTIR module of the s-SNOM setup but without the tip to focus the light as shown in Fig. 6.5. We use it initially for sample location purposes. The source is based on a *p*-polarized broadband mid-infrared light produced by a supercontinuum laser (Femtofiber pro IR and SCIR from Toptica) with average power of 0.5 mW and frequency range spanning from 1200 to 1700 cm^{-1} (from 5.8 to 8.3 µm). The spectral resolution was set to 6.25 cm^{-1}, which is the setup limit resolution. For the characterization of the photoresponse of device 2, we use the setup described in Chapter 6.

6.3.1 Photocurrent measurements and device responsivity

For the investigating the photoresponse of these devices, we first measure the device 2 using the mid-IR/LWIR setup described above. We perform a scanning photocurrent map across the device area under zero-bias graphene channel condition and set the laser wavelength to 7.9 µm as shown in Fig. 6.6a. We apply 3.5 V (0.1 eV) to the left gate (G_L) and 0.7 V (-0.22 eV) to the right gate (G_R), which corresponds to n-type and p-type doping respectively for each gated region (CNP gate value is around 3 V). As a result, a graphene pn-junction is formed that produces the photoresponse driven by the PTE effect as shown in previous chapters 3-5. We typically obtain a beam fwhm close to the incident wavelength (e.g. 10 µm for a $\lambda = 7.9$ µm).

We locate at maximum signal that corresponds to the pn-junction interface with the motorized stages as explained in the previous chapters. Here, we acquire the responsivity as a function of the incident wavelength as depicted in Fig. 6.6b. We observe relatively high responsivity values (above 10 µA/W) at the upper ($\sim$ 6-7 µm or 1660-1370 cm^{-1})

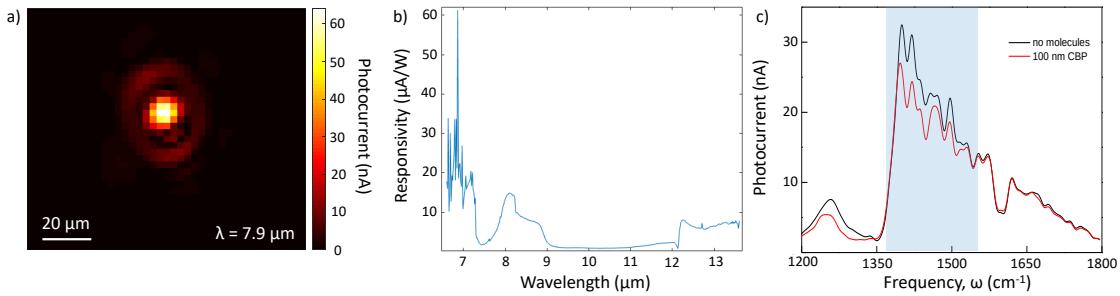

Fig. 6.6: Photoresponse of devices 1 and 2. **a)** Scanning photocurrent map of device 2 under incident light wavelength of $\lambda = 7.9$ µm. **b)** Responsivity spectrum of device 2. **c)** Photocurrent spectrum of device 1 measured in the FTIR setup for the cases of with and without the CBP molecules on top of the hBN.

and lower ($\sim$ 12-13 µm or 830-770 cm^{-1}) reststrahlen bands (RBs), which is ascribed to the enhanced photoresponse due to HPPs contribution in graphene absorption as described in Chapter 4. We also notice at 8-9 µm an increased photoresponse due to the SiO_2 phonon polaritons as also described in Chapter 4. The rest of the spectrum show low responsivity values, in particular at the TO phonons spectral regions.

Later, we measure device 1 using the nano-FTIR setup for the cases of the device covered with 100 nm thick layer of CBP molecules and without them as shown in Fig. 6.6c. We observe a higher photocurrent values at the upper RB range that is highlighted in light blue, which is in agreement with the responsivity spectrum mentioned above. We notice a pronounced decrease of the photocurrent at this upper RB wavenumber range when the 100 nm thick CBP molecules are deposited. This effect will be discussed further in the following sections.

6.3.2 CBP molecules effect on the photocurrent

We initially perform photocurrent measurements using the FTIR setup previously described and we use as a detector the device 1 instead of a commercial MCT as shown in the schematic in Fig. 6.5. We add in the optical path a CaF_2 window with different thicknesses of the CBP molecules as shown in the shared legend in Fig. 6.7. Thus, this experiment focuses on the far-field light-matter interactions occurring at distances $> 2\lambda$. In Fig. 6.7a it is exhibited the photocurrent for several thickness of the CBP molecules normalized to the photocurrent with the bare CaF_2 window. We observe that the normalized photocurrent spectrum remains with a negligible SNR until a thickness of 20 nm, where we notice 3 main dips highlighted in dashed lines corresponding to the vibrational modes of the CBP molecules as explained in section 6.1. At higher thicknesses these dips become more prominent except the middle one (at 1480 cm^{-1}) that is barely visible. We point out that in this case, the dips in photocurrent are ascribed to a lower tranmission at these particular frequencies due to the absorption of the vibrational modes of the CBP layers. It is worth mentioning that we artificially shift the amplitude of the normalized photocurrent for clarity.

In contrast, for the case when the CBP molecules are directly evaporated on top of the device, we notice a different behavior as shown in Fig. 6.7b. We label this experiment as near-field since the light-matter interactions occur at distances $<$ than the incident λ. The normalized spectrum shows the 3 dips corresponding to these vibrational modes of the CBP molecules even at the thinnest thickness evaporated (10 nm) of the CBP molecules. For larger thicknesses the dips become significantly more prominent with a high SNR. In general, we notice that the SNR or extinction of the features in the spectra are more prominent in the near-field case compared to the previous one. The fact that we observe these dips in photocurrent, means that the lineshape of the HPPs resonances are being modified due to its strong interaction with the CBP vibrational modes. Moreover, the dispersion of the hBN HPPs changes with the modification of the dielectric environment [134]. We point out that besides these 3 dips there's an additional dip appearing around 1410 cm^{-1}, which is not present in the previous far-field experiment. This dip is ascribed to the dielectric loading produced by the CBP refractive index on the hBN and metal dielectric environment, which will be discussed further in the following paragraphs.

The theoretical simulations of the absorption in graphene for the cases with a certain thickness of CBP molecules and without them are depicted in Fig. 6.7c. We observe a quite similar trend as the experimental results with the corresponding 3 dips in the normalized absorption and also the additional dip at 1410 cm^{-1} due to the dielectric loading. As mentioned in other chapters 4-5 the photocurrent is proportional to the graphene absorption.

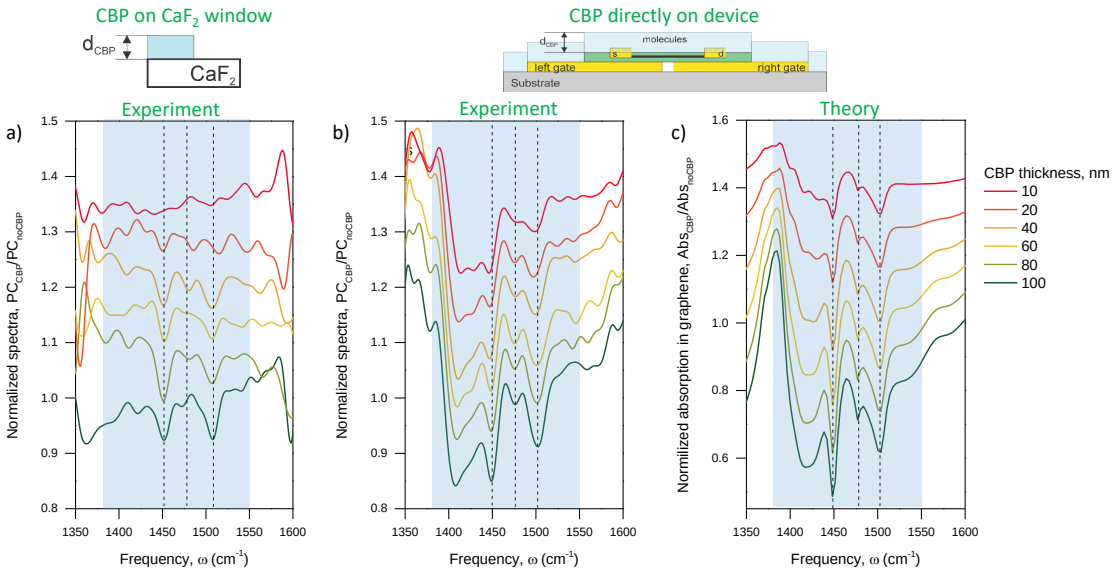

Fig. 6.7: Normalized photocurrent spectra of device 1 for several CBP layer thickness. **a)** Photocurrent spectra with a CaF_2 window in the optical path as shown in Fig. 6.5 for several CBP layer thickness (see top inset), normalized to the photocurrent without any CBP layer (just the bare CaF_2 window). The legend of CBP layer thickness is shared among all the figures. **b)** Photocurrent spectra for several CBP thickness on top of the device normalized to the photocurrent without CBP molecules. The schematic inset shows the device geometry cross section with the CBP molecules. **c)** Optical simulations of the absorption spectra of graphene on the device with several CBP thicknesses normalized to the absorption without CBP molecules.

6.3.3 Dielectric loading effect

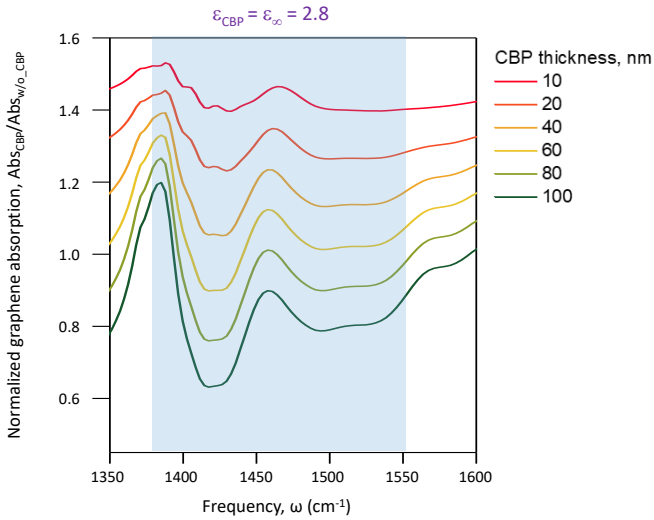

Fig. 6.8: Simulations of the graphene absorption for several CBP thicknesses normalized to the one without CBP. The dielectric permittivity of the CBP is considered as wavelength independent with a fixed value of 2.8.

We run an optical simulation to calculate the graphene absorption on the device for several thickness of CBP layers and without them as shown in Fig. 6.8. We consider a wavelength independent dielectric permittivity of the CBP layers ($\varepsilon = 2.8$), neglecting the vibrational modes of the CBP. We observe on the normalized graphene absorption that the main feature correspond to a dip around at 1410 cm^{-1} that becomes more prominent at thicker CBP thicknesses. This is ascribed to the fact that at thicker CBP layers, more electric field produced by hBN HPPs and metal can penetrate this dielectric material.[134] These simulations are in excellent agreement with the experimental behavior that we observe and gives support to the dielectric loading effect as a near-field contribution of the CBP molecules to the photocurrent and graphene absorption.

6.4 Conclusions

In conclusion, we have demonstrated a platform for electrical detection of molecular vibrations that are coupled to hyperbolic phonon polaritons in hBN. This interaction is detected by a graphene pn-junction located at the vicinity of the hBN-CBP molecules stack. We use our photodetector to acquire the interaction with CBP molecules in far and near-field measurements, obtaining clear differences between them. Moreover, our simulations strongly support the experimental results with excellent agreement. This study gives insights for the development of a highly compact detector, where the optical and electrical readout is integrated in one single device that would have strong impact in the field of ultrasensitive molecular spectroscopy.

7 Conclusions and outlook

In this thesis we have shown a remarked advance of optoelectronic graphene devices for the non-well explored range of mid, long-wave and far-infrared (terahertz). Especially, we have shown photodetectors at this wavelength regime that outperform the state-of-the-art graphene photodetectors and commercially available technology. These results serve as a guidance for building the new generation of infrared cameras, ultracompact spectrometers, gas sensors and more optoelectronic devices.

In chapter 2, we have described the state-of-the-art techniques for assembly of 2D layers, the fabrication of one-dimensional contact between a metallic electrode and graphene and also the fabrication of metallic nanostructures that are involved in these optoelectronic devices. We explained the different techniques that we used to measure the electronic properties and the photoresponse of these devices. Additionally, we illustrated some of the photodetectors figures of merit for proper comparison with commercial technology.

We have successfully integrated an antenna with a graphene pn-junction for highly sensitive and fast THz detection in this regime as described in chapter 3. This novel terahertz detector exploits efficiently the PTE effect, based on a design that employs a dual-gated, dipolar antenna with a nanogap (around 100 nm). The narrow-gap antenna simultaneously creates a pn-junction in the graphene channel, which is located just above the antenna and strongly concentrates the incident THz light at this pn-junction, where the photoresponse is created. We have demonstrated that this novel detector leads to an excellent sensitivity, with a noise-equivalent power of 80 $pW/\sqrt{Hz}$ at room temperature, a response time below 30 ns (setup-limited), a wide dynamic range (linear power dependence over more than 3 orders of magnitude) and broadband operation range (measured at 1.8–4.2 THz, antenna-limited), which fulfills a combination of figure-of-merits that is currently missing in the state-of-the-art detectors, even after 2 years of publishing the work[135]. Importantly, on the basis of the agreement we obtained between experiment, analytical model, and numerical simulations, we have reached a solid understanding of how the PTE effect gives rise to a THz-induced photoresponse, which enables a further detector optimization. The outlook of this work consists on optimizing the antenna, in order to obtain a higher absorption in graphene and hence achieving a lower NEP. Moreover, by considering an even broader band operation antenna (e.g. log-periodic), the detector will be sensitive for a broader range of THz frequencies. The sensitivity can be further improved by having a lower thermal conductivity. This could be achieved by using alternative encapsulation materials, rather than hBN (e.g. a transition metal dichalcogenide (TMD) material) and by operating at a lower temperature.

In chapter 4 we overcame the main challenge of infrared photodetectors, which is to funnel the light into a small nanoscale active area and efficiently convert it into an electrical signal. We achieve this by efficient coupling of a plasmonic antenna to hyperbolic phonon-polaritons in hBN to highly concentrate mid-infrared light into a graphene pn-junction. We use a metallic bowtie antenna and H-shape resonant gates that besides concentrating the light into its nanogap, their plasmonic resonances spectrally overlap within the upper reststrahlen band of hBN (6-7 μm), thus launching efficiently these HPPs and guiding them with constructive interferences towards the photodetector active area. The two different antennas allow us to have sensitive detection in two incident polarizations. Furthermore, we tuned the device geometry to balance the interplay of the absorption, electrical and

thermal conductivity of graphene. This approach yields outstanding device performance by featuring room temperature high sensitivity (NEP of 82 pW/$\sqrt{Hz}$) and fast rise time of 17 ns (setup-limited), among others, thus obtaining a combination currently not present in the state-of-the-art graphene and commercially available mid-infrared detectors. We supported these experimental results by a novel multiphysics model, which includes optical, thermal and electrostatic simulations that show excellent quantitatively agreement. Consequently, the simulations revealed the different contributions to our photoresponse, thus paving the way for further improvement of these types of photodetectors even beyond mid-infrared range. We point out that this concept can be further extended to other wavelengths by tuning the antennas and combining with HPPs in other spectral regions of the mid and long-wave infrared range that are present in other 2D materials such as V_2O_5 [136], MoO_3 [120,122], which this latter one presents HPPs also in the THz range [137]. Additional tuning and wavelength sensitivity can be accomplished by controlling the hyperbolic material's thickness or shape, thus allowing this type of detector more specific functionalities such as hyperspectral imaging and spectroscopy.

In chapter 5 we have shown mid and long-wave infrared photocurrent spectroscopy via electrical detection of graphene plasmons, hyperbolic phonon-polaritons and their hybridized modes. We combined in one single platform the efficiently excited polaritonic material that also acts as a detector itself. We fabricated 4 devices based on high quality graphene encapsulated by hexagonal boron nitride (hBN) placed on top of metallic rod arrays that serve to launch the hBN phonon polaritons and/or graphene plasmons. We also doped graphene via an electrostatic potential applied between these rods and graphene separated by a thin hBN layer. By following this approach, we reached high Fermi level values of the order of 0.4 eV. We performed transmission measurements using FTIR. We observed graphene plasmons and the hybridized plasmon phonon polaritons that showed a blue shift when increasing the gate voltage (Fermi level). This confirms the plasmonic behaviour of these resonances. Moreover, we observed narrow linewidths of these resonances that show an extinction value above 10%. Additionally, these metallic gratings form two independent gates to create a graphene pn-junction. We characterized the photoresponse that we determined the PTE effect as the dominant mechanism. We performed photocurrent spectra in the mid and long-wave infrared range (from $\lambda = 6.6$ to 13.6 µm) at different gate voltages for tuning the graphene Fermi level. We identified peaks in the photocurrent spectra that evolves and blue shift by increasing the gate voltage. In particular, we observed hybridized plasmon phonon polaritons at the upper and lower reststrahlen bands of hBN. Also we observed graphene plasmons that are confined between the metal and separated by 5 nm of hBN. We have demonstrated the wide tunability of these nanoresonators by changing several parameters to shift the spectral position of the resonances, such as hBN thickness, grating period, substrate (SiO_2 or CaF_2) and graphene Fermi energy. Our results showed excellent agreement with the simulated absorption spectra and dispersion relation of these 2D polaritonic modes. Thus, this approach enables an *in-situ* tunable platform for spectrally selective detection in this range and has the potential to constitute high accuracy thermal imaging, compact spectrometers, gas sensors, etc. The future work of this chapter includes to develop a multiphysics model as explained in chapter 4, so that we can estimate in a quantitative manner the photoresponse of these devices. Also we will use this novel platform for gas sensing purposes at this spectral regime.

Finally, in chapter 6 we investigated the electrical detection of molecular vibrations of CBP coupled to hyperbolic phonon polartions in hBN. We detected this strong light-matter interaction via a graphene pn-junction placed at the vicinity of the CBP-hBN stack. The edges of the gap of the local gates launch efficiently the hBN HPPs that interact with the CBP molecular resonances that are spectrally located at the upper RB. We studied this coupling as a function of the CBP thickness and observed a stronger effect for thicker CBP layers due to the stronger field penetration produced by the HPPs. Additionally, we compared two type of measurements configurations: 1) a far field configuration where a CaF_2 window is added to the optical path far from the graphene detector and 2) for the near field case where the CBP molecules are deposited directly on top of the graphene detector. We observed a significant difference between both experiments, which the near field showed the highest sensitivity by identifying already the vibrational modes for thin CBP layers of 10 nm. The theoretical simulations are in excellent agreement with the experimental results as a function of the CBP thickness. This investigation demonstrates the development of a highly compact sensor that includes the optical and electrical components in one single device. This work paves the way for miniaturizing these sensors since the active area is quite small allowing ultrasensitive molecular spectroscopy. The future work will be to show vibrational strong coupling via electrical detection. For this purpose, several devices will be required, which represent a significant effort to demonstrate it experimentally. Moreover, by enhancing the responsivity of the detector as shown in the previous chapters, we could probably detect with a high SNR sub-nm layers of CBP. Another direction would be to detect other type of molecule with the vibrational modes at different spectral region. Another interesting experiment would be to detect resonances of vibrational modes of gases, hence we could have a dynamical platform for detection at this spectral range that could be extended even at THz frequencies[137].

Publications

The chapters of the thesis are written based on the following publications:

Chap. 3 K.J. Tielrooij, S. Castilla, B. Terres, M. Autore, L. Viti, J. Li, A. Nikitin, M. S. Vitiello, R. Hillenbrand, F.H.L. Koppens, Highly sensitive, ultrafast photo-thermoelectric graphene thz detector, 2018 43rd International Conference on Infrared, Millimeter, and Terahertz Waves (IRMMW-THz) (2018)

Chap. 3 S. Castilla, B. Terres, M. Autore, L. Viti, J. Li, A. Nikitin, I. Vangelidis, K. Watanabe, T. Taniguchi, E. Lidorikis, M. S. Vitiello, R. Hillenbrand, K. J. Tielrooij, F.H.L. Koppens, Fast and sensitive terahertz detection using an antenna-integrated graphene pn junction, Nano letters 19 (5), 2765-2773 (2019)

Chap. 4 S. Castilla,* I. Vangelidis,* V.-V. Pusapati, J. Goldstein, M. Autore, T. Slipchenko, K. Rajendran, S. Kim, K. Watanabe, T. Taniguchi, L. Martín-Moreno, D. Englund, K.J. Tielrooij, R. Hillenbrand, E. Lidorikis, F.H.L. Koppens, Plasmonic antenna coupling to hyperbolic phonon-polaritons for sensitive and fast mid-infrared photodetection with graphene, Nature Communications 11, 4872 (2020)

Chap. 5 S. Castilla, H. Agarwal, D. Alcaraz-Iranzo, Y. Bludov, I. Vangelidis, A. Grabulosa, M. Ceccanti, I. Torre, K. Watanabe, T. Taniguchi, H. Herzig-Sheinfux, E. Lidorikis, N. Peres, F.H.L. Koppens, Mid and long-wave infrared photocurrent spectroscopy via electrical detection of 2D polaritonic nanoresonators, in preparation

Chap. 6 A. Bylinkin,* S. Castilla,* T. Slipchenko,* M. Autore, V.-V. Pusapati, D. Barcons, K. Watanabe, T. Taniguchi, L. Martín-Moreno, A. Nikitin, R. Hillenbrand, E. Lidorikis, F.H.L. Koppens, Electrical detection of molecular vibrations coupled to hyperbolic phonon polaritons, in preparation

Other publications by the author (not included as thesis chapters):

H. Herzig-Sheinfux, L. Orsini, M. Jung, I. Torre, M. Ceccanti, R.A. Maniyara, D. Barcons-Ruiz, S. Castilla, N.C.H. Hesp, E. Janzen, V. Pruneri, J.H. Edgar, G. Shvets, F.H.L. Koppens, Bound in the continuum modes in indirectly-patterned hyperbolic media, 2021 Conference on Lasers and Electro-Optics Europe and European Quantum Electronics Conference (CLEO/Europe-EQEC) (2021)

H. Herzig-Sheinfux, L. Orsini, M. Jung, I. Torre, M. Ceccanti, R.A. Maniyara, D. Barcons-Ruiz, S. Castilla, N.C.H. Hesp, E. Janzen, V. Pruneri, J.H. Edgar, G. Shvets, F.H.L. Koppens, Bound in the continuum modes in indirectly-patterned hyperbolic media, submitted (2021)

I. Vangelidis, D. V. Bellas, S. Suckow, G. Dabos, S. Castilla, F.H.L. Koppens, A. C. Ferrari, N. Pleros, and E. Lidorikis, Unbiased plasmonic-assisted integrated graphene photodetectors, submitted (2021)

S. Castilla,* V.-V. Pusapati,* D. De Fazio. R. Bertini, M. Ceccanti, I. Torre, H. Herzig-Sheinfux, F.H.L. Koppens, Electrical detection of gate tunable low-loss hyperbolic nanoresonators at low temperatures, in preparation

*: These authors contributed equally.

Bibliography

[1] Rogalski, A., Martyniuk, P. & Kopytko, M. Challenges of small-pixel infrared detectors: a review. *Rep. Prog. Phys.* **79**, 046501 (2016).

[2] Rogalski, A. Graphene-based materials in the infrared and terahertz detector families: a tutorial. *Advances in Optics and Photonics* **11**, 314 (2019).

[3] Goossens, S. et al. Broadband image sensor array based on graphene-CMOS integration. *Nature Photonics* **11**, 366–371 (2017).

[4] Autore, M. et al. Boron nitride nanoresonators for Phonon-Enhanced molecular vibrational spectroscopy at the strong coupling limit. *Light: Science and Applications* **7**, 17172–17178 (2018).

[5] Rodrigo, D. et al. Mid-infrared plasmonic biosensing with graphene. *Science* **349**, 165–168 (2015).

[6] Lee, I. H., Yoo, D., Avouris, P., Low, T. & Oh, S. H. Graphene acoustic plasmon resonator for ultrasensitive infrared spectroscopy. *Nature Nanotechnology* **14**, 313–319 (2019).

[7] Ferguson, B. & Zhang, X. C. Materials for terahertz science and technology. *Nature Materials* **1**, 26–33 (2002).

[8] Mittleman, D. Sensing with Terahertz Radiation. *Springer-Verlag: Berlin* **342**, 614–617 (2003).

[9] Kleine-Ostmann, T. & Nagatsuma, T. A review on terahertz communications research. *Journal of Infrared, Millimeter, and Terahertz Waves* **32**, 143–171 (2011).

[10] Scontel. *Superconducting nanotechnology* **available at http://www.scontel.ru/terahertz/** (2018).

[11] Appleby, R. & Wallace, H. B. Standoff detection of weapons and contraband in the 100 GHz to 1 THz region. *IEEE Trans. Antennas Propag.* **55**, 2944–2956 (2007).

[12] Gentec-EO. *Pyroelectric terahertz detectors* **available at http://www.gentec-eo.com/products/thz-detectors/** (2018).

[13] Guo, Q. et al. Efficient electrical detection of mid-infrared graphene plasmons at room temperature. *Nature Materials* **17**, 986–992 (2018).

[14] Basov, D. N., Fogler, M. M. & García De Abajo, F. J. Polaritons in van der Waals materials. *Science* **354** (2016).

[15] Low, T. et al. Polaritons in layered two-dimensional materials. *Nature Mater.* **16**, 182–194 (2016).

[16] Caldwell, J. D. et al. Low-loss, infrared and terahertz nanophotonics using surface phonon polaritons. *Nanophotonics* **4**, 44–68 (2015).

[17] *Virginia diodes. schottky diodes terahertz detectors* **available at http://www.vadiodes.com/en/products/detectors** (2018).

[18] Geim, A. K. & Novoselov, K. S. The rise of graphene. *Nature Mater.* **6**, 183–191 (2007).

[19] Koppens, F. H. L. et al. Photodetectors based on graphene, other two-dimensional materials and hybrid systems. *Nat Nano* **9**, 780–793 (2014).

[20] Li, Z. Q. et al. Dirac charge dynamics in graphene by infrared spectroscopy. *Nature Physics* **4**, 532–535 (2008).

[21] Low, T. & Avouris, P. Graphene plasmonics for terahertz to mid-infrared applications. *ACS Nano* **8**, 1086–1101 (2014).

[22] Banszerus, L. et al. Ultrahigh-mobility graphene devices from chemical vapor deposition on reusable copper. *Science Advances* **1**, 1–7 (2015).

[23] Tielrooij, K. J. et al. Generation of photovoltage in graphene on a femtosecond timescale through efficient carrier heating. *Nature Nanotechnology* **10**, 437–443 (2015).

[24] Low, T. & Avouris, P. Graphene plasmonics for terahertz to mid-infrared applications. *ACS Nano* **8**, 1086–1101 (2014).

[25] Gonçalves, P. A. & Peres, N. M. *An Introduction to Graphene Plasmonics* (2016). 1609.04450.

[26] Hwang, E. H., Rossi, E. & Das Sarma, S. Theory of thermopower in two-dimensional graphene. *Physical Review B - Condensed Matter and Materials Physics* **80**, 1–5 (2009).

[27] Mics, Z. et al. Thermodynamic picture of ultrafast charge transport in graphene. *Nature Communications* **6**, 7655 (2015).

[28] Woessner, A. et al. Highly confined low-loss plasmons in graphene–boron nitride heterostructures. *Nature Mater.* **14**, 421–425 (2015).

[29] Koppens, F. H. L., Chang, D. E. & García de Abajo, F. J. Graphene Plasmonics: A Platform for Strong Light-Matter Interactions. *Nano Lett.* **11**, 3370–3377 (2011).

[30] Smith, C. L., Stenger, N., Kristensen, A., Mortensen, N. A. & Bozhevolnyi, S. I. Gap and channeled plasmons in tapered grooves: A review. *Nanoscale* **7**, 9355–9386 (2015).

[31] Iranzo, D. A. et al. Probing the ultimate plasmon confinement limits with a van der Waals heterostructure. *Science* **360**, 291–295 (2018).

[32] Epstein, I. et al. Far-field excitation of single graphene plasmon cavities with ultra-compressed mode volumes. *Science* **368**, 1219–1223 (2020).

[33] Foteinopoulou, S., Devarapu, G. C. R., Subramania, G. S., Krishna, S. & Wasserman, D. *Phonon-polaritonics: Enabling powerful capabilities for infrared photonics* (2019).

[34] Wang, L. One-Dimensional Electrical Contact to. *Science (New York, N.Y.)432* **342**, 614–617 (2013).

[35] Caldwell, J. D. et al. Sub-diffractional volume-confined polaritons in the natural hyperbolic material hexagonal boron nitride. *Nature Commun.* **5**, 5221 (2014).

[36] Giles, A. J. et al. Ultralow-loss polaritons in isotopically pure boron nitride. *Nature Materials* **17**, 134–139 (2018).

[37] Dai, S. et al. Graphene on hexagonal boron nitride as a tunable hyperbolic metamaterial. *Nature Nanotech.* **10**, 682–686 (2015).

[38] Efetov, D. K. et al. Fast thermal relaxation in cavity-coupled graphene bolometers with a Johnson noise read-out. *Nature Nanotechnology* **13**, 797–801 (2018).

[39] Skoblin, G., Sun, J. & Yurgens, A. Graphene bolometer with thermoelectric readout and capacitive coupling to an antenna. *Applied Physics Letters* **112**, 063501 (2018).

[40] Freitag, M., Low, T., Xia, F. & Avouris, P. Photoconductivity of biased graphene. *Nature Photonics* **7**, 53–59 (2013).

[41] Shiue, R. J. et al. High-Responsivity Graphene-Boron Nitride Photodetector and Autocorrelator in a Silicon Photonic Integrated Circuit. *Nano Letters* **15**, 7288–7293 (2015).

[42] Cai, X. et al. Sensitive room-temperature terahertz detection via the photothermoelectric effect in graphene. *Nature Nanotechnology* **9**, 814–819 (2014).

[43] Song, J. C. W., Rudner, M. S., Marcus, C. M. & Levitov, L. S. Hot carrier transport and photocurrent response in graphene. *Nano letters* **11**, 4688–4692 (2011).

[44] Gabor, N. M. et al. Hot Carrier-Assisted Intrinsic Photoresponse in Graphene. *Science* **334**, 648–652 (2011).

[45] Tielrooij, K. J. et al. Out-of-plane heat transfer in van der Waals stacks through electron-hyperbolic phonon coupling. *Nature Nanotechnology* **13**, 41–46 (2018).

[46] Kittel, C. *Introduction to Solid State Physics* (Wiley, 2004), 8 edn.

[47] Li, X. et al. Large-area synthesis of high-quality and uniform graphene films on copper foils. *Science* **324**, 1312–1314 (2009).

[48] Bae, S. et al. Roll-to-roll production of 30-inch graphene films for transparent electrodes. *Nature Nanotechnology* **5**, 574–578 (2010).

[49] Xu, X. et al. Ultrafast epitaxial growth of metre-sized single-crystal graphene on industrial Cu foil. *Science Bulletin* **62**, 1074–1080 (2017).

[50] Caneva, S. et al. Nucleation control for large, single crystalline domains of monolayer hexagonal boron nitride via Si-doped Fe catalysts. *Nano Letters* **15**, 1867–1875 (2015).

[51] Blake, P. et al. Making graphene visible. *Applied Physics Letters* **91** (2007).

[52] Martin, J. et al. Observation of electron-hole puddles in graphene using a scanning single-electron transistor. *Nature Physics* **4**, 144–148 (2008).

[53] Chen, J. H., Jang, C., Xiao, S., Ishigami, M. & Fuhrer, M. S. Intrinsic and extrinsic performance limits of graphene devices on SiO 2. *Nature Nanotechnology* **3**, 206–209 (2008).

[54] Dean, C. R. et al. Boron nitride substrates for high-quality graphene electronics. *Nature Nanotechnology* **5**, 722–726 (2010).

[55] Giles, A. J. et al. Ultralow-loss polaritons in isotopically pure boron nitride. *Nature Materials* **17**, 134–139 (2018).

[56] Pizzocchero, F. et al. The hot pick-up technique for batch assembly of van der Waals heterostructures. *Nature Communications* **7** (2016).

[57] Purdie, D. G. et al. Cleaning interfaces in layered materials heterostructures. *Nature Communications* **9**, 1–12 (2018).

[58] Singh, K., Ohlan, A. & Dhawan, S. Polymer-graphene nanocomposites: Preparation, characterization, properties, and applications. In Ebrahimi, F. (ed.) *Nanocomposites*, chap. 3 (IntechOpen, Rijeka, 2012).

[59] Ferrari, A. C. & Basko, D. M. Raman spectroscopy as a versatile tool for studying the properties of graphene. *Nature Nanotech.* **8**, 235–246 (2013).

[60] Castellanos-Gomez, A. et al. Deterministic transfer of two-dimensional materials by all-dry viscoelastic stamping. *2D Materials* **1**, 011002 (2014).

[61] Jessen, B. S. et al. Lithographic band structure engineering of graphene. *Nature Nanotechnology* **14**, 340–346 (2019).

[62] Mueller, T., Xia, F., Freitag, M., Tsang, J. & Avouris, P. Role of contacts in graphene transistors: A scanning photocurrent study. *Phys. Rev. B* **79**, 245430 (2009).

[63] Badioli, M. et al. Phonon-Mediated Mid-Infrared Photoresponse of Graphene. *Nano Lett.* **14**, 6374–6381 (2014).

[64] Woessner, A. et al. *Electrical detection of hyperbolic phonon-polaritons in heterostructures of graphene and boron nitride* 1–6 (2017).

[65] Klots, A. R. et al. Probing excitonic states in suspended two-dimensional semiconductors by photocurrent spectroscopy. *Scientific Reports* **4**, 1–7 (2014).

[66] Vicarelli, L. et al. Graphene field-effect transistors as room-temperature terahertz detectors. *Nature Materials* **11**, 865–871 (2012).

[67] Spirito, D. et al. High performance bilayer-graphene Terahertz detectors. *Applied Physics Letters* **104**, 061111 (2014).

[68] Viti, L., Purdie, D. G., Lombardo, A., Ferrari, A. C. & Vitiello, M. S. HBN-Encapsulated, Graphene-based, Room-temperature Terahertz Receivers, with High Speed and Low Noise. *Nano Letters* **20**, 3169–3177 (2020).

[69] Tonouchi, M. Cutting-edge terahertz technology. *Nature Photonics* **1**, 97–105 (2007).

[70] Lee, M. & Wanke, M. C. Searching for a solid-state terahertz technology. *Science* **316**, 64–65 (2007).

[71] Federici, J. F. et al. THz imaging and sensing for security applications - Explosives, weapons and drugs. *Semiconductor Science and Technology* **20** (2005).

[72] Siegel, P. H. Terahertz technology in biology and medicine. *IEEE Transactions on Microwave Theory and Techniques* **52**, 2438–2447 (2004).

[73] Ma, J., Karl, N. J., Bretin, S., Ducournau, G. & Mittleman, D. M. Frequency-division multiplexer and demultiplexer for terahertz wireless links. *Nature Communications* **8**, 1–7 (2017).

[74] Mittendorff, M., Li, S. & Murphy, T. E. Graphene-Based Waveguide-Integrated Terahertz Modulator. *ACS Photonics* **4**, 316–321 (2017).

[75] Tydex. *Golay cells terahertz detectors* **available at http://www.tydexoptics.com/products** (2018).

[76] Sizov, F. & Rogalski, A. THz detectors. *Progress in Quantum Electronics* **34**, 278–347 (2010).

[77] Bonaccorso, F., Sun, Z., Hasan, T. & Ferrari, A. C. Graphene photonics and optoelectronics. *Nature Photonics* **4**, 611–622 (2010).

[78] Mittendorff, M. et al. Ultrafast graphene-based broadband THz detector. *Applied Physics Letters* **103** (2013).

[79] Zak, A. et al. Antenna-integrated 0.6 THz FET direct detectors based on CVD graphene. *Nano Letters* **14**, 5834–5838 (2014).

[80] Generalov, A. A., Andersson, M. A., Yang, X., Vorobiev, A. & Stake, J. A 400-GHz

Graphene FET Detector. *IEEE Transactions on Terahertz Science and Technology* **7**, 614–616 (2017).

[81] Bandurin, D. A. et al. Dual origin of room temperature sub-terahertz photoresponse in graphene field effect transistors. *Applied Physics Letters* **112** (2018).

[82] Auton, G. et al. Terahertz Detection and Imaging Using Graphene Ballistic Rectifiers. *Nano Letters* **17**, 7015–7020 (2017).

[83] Lemme, M. C. et al. Gate-activated photoresponse in a graphene p-n junction. *Nano Letters* **11**, 4134–4137 (2011).

[84] Guo, W. et al. Graphene-based broadband terahertz detector integrated with a square-spiral antenna. *Optics Letters* **43**, 1647 (2018).

[85] Tan, Y. W. & Kim, P. Measurement of Scattering Rate and Minimum Conductivity in Graphene. *Phys. Rev. Lett.* **99**, 246803 (2007).

[86] Lee, J. E., Ahn, G., Shim, J., Lee, Y. S. & Ryu, S. Optical separation of mechanical strain from charge doping in graphene. *Nature Communications* **3**, 1024–1028 (2012).

[87] Zuev, Y., Chang, W. & Kim, P. Thermoelectric and Magnetothermoelectric Transport Measurements of Graphene. *Phys. Rev. Lett.* **102**, 96807 (2009).

[88] Bistritzer, R. & MacDonald, A. H. Electronic cooling in graphene. *Physical review letters* **102**, 206410 (2009).

[89] Lundeberg, M. B. & Koppens, F. H. L. Thermodynamic reciprocity in scanning photocurrent maps. *Arxiv* 1–5 (2020).

[90] Landau, L. D. et al. Electrodynamics of continuous media. *Elsevier* **8** (1984).

[91] Cai, W. et al. Thermal transport in suspended and supported monolayer graphene grown by chemical vapor deposition. *Nano Letters* **10**, 1645–1651 (2010).

[92] Koh, Y. K., Bae, M. H., Cahill, D. G. & Pop, E. Heat conduction across monolayer and few-layer graphenes. *Nano Letters* **10**, 4363–4368 (2010).

[93] Mak, K. F., Ju, L., Wang, F. & Heinz, T. F. Optical spectroscopy of graphene: From the far infrared to the ultraviolet. *Solid State Communications* **152**, 1341–1349 (2012).

[94] Dawlaty, J. M. et al. Measurement of the optical absorption spectra of epitaxial graphene from terahertz to visible. *Applied Physics Letters* **93** (2008).

[95] Viti, L. et al. Thermoelectric graphene photodetectors with sub-nanosecond response times at terahertz frequencies. *Nanophotonics* **10**, 89–98 (2020).

[96] Hu, G., Shen, J., Qiu, C. W., Alù, A. & Dai, S. Phonon Polaritons and Hyperbolic Response in van der Waals Materials. *Advanced Optical Materials* **1901393**, 1–19 (2019).

[97] Dai, S. et al. Graphene on hexagonal boron nitride as a tunable hyperbolic metamaterial. *Nature Nanotechnology* **10**, 682–686 (2015).

[98] Nikitin, A. Y. et al. Nanofocusing of Hyperbolic Phonon Polaritons in a Tapered Boron Nitride Slab. *ACS Photonics* **3**, 924–929 (2016).

[99] Tamagnone, M. et al. Ultra-confined mid-infrared resonant phonon polaritons in van der Waals nanostructures. *Science Advances* **4**, 4–10 (2018).

[100] Castilla, S. et al. Fast and Sensitive Terahertz Detection Using an Antenna-Integrated Graphene pn Junction. *Nano Letters* **19**, 2765–2773 (2019).

[101] Peng, C. et al. Compact mid-infrared graphene thermopile enabled by a nanopatterning technique of electrolyte gates. *New Journal of Physics* **20**, 083050 (2018).

[102] Schuler, S. et al. Graphene Photodetector Integrated on a Photonic Crystal Defect Waveguide. *ACS Photonics* **5**, 4758–4763 (2018).

[103] Muench, J. E. et al. Waveguide-Integrated, Plasmonic Enhanced Graphene Photodetectors. *Nano Letters* **19**, 7632–7644 (2019).

[104] Pons-Valencia, P. et al. Launching of hyperbolic phonon-polaritons in h-BN slabs by resonant metal plasmonic antennas. *Nature Communications* **10**, 1–8 (2019).

[105] Herring, P. K. et al. Photoresponse of an electrically tunable ambipolar graphene infrared thermocouple. *Nano Lett.* **14**, 901–907 (2014).

[106] Hsu, A. L. et al. Graphene-Based Thermopile for Thermal Imaging Applications. *Nano Lett.* **15**, 7211–7216 (2015).

[107] Dai, S. et al. Subdiffractional focusing and guiding of polaritonic rays in a natural hyperbolic material. *Nature Communications* **6**, 1–7 (2015).

[108] Cakmakyapan, S., Lu, P. K., Navabi, A. & Jarrahi, M. Gold-patched graphene nano-stripes for high-responsivity and ultrafast photodetection from the visible to infrared regime. *Light: Science and Applications* **7** (2018).

[109] Sassi, U. et al. Graphene-based mid-infrared room-temperature pyroelectric bolometers with ultrahigh temperature coefficient of resistance. *Nature Communications* **8** (2017).

[110] Yu, X. et al. Narrow bandgap oxide nanoparticles coupled with graphene for high performance mid-infrared photodetection. *Nature Communications* **9**, 1–8 (2018).

[111] Kischkat, J. et al. Mid-infrared optical properties of thin films of aluminum oxide, titanium dioxide, silicon dioxide, aluminum nitride, and silicon nitride. *Applied Optics* **51**, 6789–6798 (2012).

[112] Hanson, G. W. Quasi-transverse electromagnetic modes supported by a graphene parallel-plate waveguide. *Journal of Applied Physics* **104** (2008).

[113] Johnson, P. & Christy, R. Optical constants of the noble metals. *Phys. Rev. B* **6**, 4370–4379 (1972).

[114] Cutler, M. & Mott, N. F. Observation of anderson localization in an electron gas. *Physical Review* **181**, 1336–1340 (1969).

[115] Soavi, G. et al. Broadband, electrically tunable third-harmonic generation in graphene. *Nature Nanotechnology* **13**, 583–588 (2018).

[116] McPherson, J. W., Kim, J., Shanware, A., Mogul, H. & Rodriguez, J. Trends in the ultimate breakdown strength of high dielectric-constant materials. *IEEE Transactions on Electron Devices* **50**, 1771–1778 (2003).

[117] Kim, K. K. et al. Synthesis and characterization of hexagonal boron nitride film as a dielectric layer for graphene devices. *ACS Nano* **6**, 8583–8590 (2012).

[118] Xia, F., Perebeinos, V., Lin, Y. M., Wu, Y. & Avouris, P. The origins and limits of metal-graphene junction resistance. *Nature Nanotechnology* **6**, 179–184 (2011).

[119] Mišković, Z. L. & Upadhyaya, N. Modeling electrolytically top-gated graphene. *Nanoscale Research Letters* **5**, 505–511 (2010).

[120] Ma, W. et al. In-plane anisotropic and ultra-low-loss polaritons in a natural van der Waals crystal (2018).

[121] Zheng, Z. et al. Highly Confined and Tunable Hyperbolic Phonon Polaritons in Van Der Waals Semiconducting Transition Metal Oxides. *Advanced Materials* **30**, 1–9 (2018).

[122] Zheng, Z. et al. A mid-infrared biaxial hyperbolic van der Waals crystal. *Science Advances* **5**, 1–9 (2019).

[123] Dai, S. et al. Tunable Phonon Polaritons in Atomically Thin van der Waals Crystals of Boron Nitride. *Science* **343, 6175**, 1125–1129 (2014).

[124] Kalfagiannis, N., Stoner, J. L., Hillier, J., Vangelidis, I. & Lidorikis, E. Mid- to far-infrared sensing: SrTiO 3 , a novel optical material . *Journal of Materials Chemistry C* (2019).

[125] Alfaro-Mozaz, F. J. et al. Deeply subwavelength phonon-polaritonic crystal made of a van der Waals material. *Nature Communications* **10**, 1–7 (2019).

[126] Li, P. et al. Hyperbolic phonon-polaritons in boron nitride for near-field optical imaging and focusing. *Nature Communications* **6**, 1–9 (2015).

[127] Bareza, N. J., Gopalan, K. K., Alani, R., Paulillo, B. & Pruneri, V. Mid-infrared Gas Sensing Using Graphene Plasmons Tuned by Reversible Chemical Doping. *ACS Photonics* **7**, 879–884 (2020).

[128] Lundeberg, M. B. et al. Thermoelectric detection and imaging of propagating graphene plasmons. *Nature Materials* **16**, 204–207 (2017).

[129] Alonso-González, P. et al. Acoustic terahertz graphene plasmons revealed by photocurrent nanoscopy. *Nat Nano* **12**, 31–35 (2017).

[130] Brar, V. W., Jang, M. S., Sherrott, M., Lopez, J. J. & Atwater, H. A. Highly confined tunable mid-infrared plasmonics in graphene nanoresonators. *Nano Letters* **13**, 2541–2547 (2013).

[131] Fei, Z. et al. Infrared nanoscopy of dirac plasmons at the graphene-SiO2 interface. *Nano Letters* **11**, 4701–4705 (2011).

[132] Wei, L. et al. Application of terahertz spectroscopy in biomolecule detection. *Frontiers in Laboratory Medicine* **2**, 127–133 (2018).

[133] Qin, J. et al. Ultrasensitive detection of saccharides using terahertz sensor based on metallic nano-slits. *Scientific Reports* **10**, 1–6 (2020).

[134] Bylinkin, A. et al. Real-space observation of vibrational strong coupling between propagating phonon polaritons and organic molecules. *Nature Photonics* **15**, 197–202 (2021).

[135] Liu, J. et al. *Recent Progress in the Development of Graphene Detector for Terahertz Detection* 1–24 (2021).

[136] Taboada-Gutiérrez, J. et al. Broad spectral tuning of ultra-low-loss polaritons in a van der Waals crystal by intercalation. *Nature Materials* **19**, 964–968 (2020).

[137] de Oliveira, T. V. et al. Nanoscale-Confined Terahertz Polaritons in a van der Waals Crystal. *Advanced Materials* **33** (2021).